

HANDHELD XRF AS A PROXY FOR ONSITE EVALUATION OF UNCONVENTIONAL
TARGETS: AN INVESTIGATION OF THE WOODFORD SHALE, ANADARKO BASIN,
OKLAHOMA.

by

TYLER JAYNE WILLEY

B.S., Union College, 2011

A THESIS

Submitted in partial fulfillment of the requirements for the degree

MASTER OF SCIENCE

Department of Geology
College of Arts and Sciences

KANSAS STATE UNIVERSITY
Manhattan, Kansas

2015

Approved by:

Major Professor
Matthew Totten

Copyright

TYLER JAYNE WILLEY

2015

Abstract

The Woodford shale is recognized as an abundant source rock across Oklahoma and much of the midcontinent (Lambert, 1990), and up to 8% of the world's hydrocarbon reserves are estimated to have been sourced by the Woodford and its equivalents (Fritz et al, 1991). The Woodford shale is far more complex than other Devonian black shales found in North America due to the presence of alternating bands of chert-like amorphous silica and silica-rich shale. Analysis of chert and its possible role in gas generation and storage in shales has been largely overlooked. The goal of this study is to determine if chert size, amounts, or polycrystallinity can be indicators of thermal maturity within the Woodford shale. Handheld XRF analysis was conducted on the whole rock samples, and a mudrock specific sodium bisulfate fusion was used to separate the non-clay fraction. SEM was performed on the resulting separates to study and observe changes in chert fabric, grain-size, and amount.

No correlations were observed to indicate that chert is an indicator of thermal maturity within the Woodford shale. Increase in chert growth and amount was also not detected within the size fractions as thermal maturity increases. Handheld XRF proved to be a good proxy for quick, onsite analysis of silica concentrations, as well as the amount of organic matter within drill core. This could be beneficial as hydraulic fracking produces best results in areas of higher silica content, and the wells with the highest organic matter have the highest potential for petroleum accumulations.

Table of Contents

List of Figures	vi
List of Tables	viii
Acknowledgements.....	ix
Dedication	x
Chapter 1 - Introduction.....	1
1.1 – Significance	3
1.2 – Geologic Setting	5
1.3 – Previous Work	10
Chapter 2 - Methodology	12
2.1 – Sample Selection.....	12
2.2 – Whole Rock XRF Analysis.....	14
2.3 – Sodium Bisulfate Fusion.....	16
2.4 – FESEM.....	17
Chapter 3 - Results.....	18
3.1 Whole Rock XRF Analysis.....	18
3.2 Sodium Bisulfate Fusion.....	21
3.3 SEM with EDS Spectra.....	23
3.4 Size Distribution	27
Chapter 4 - Discussion	30
4.1 – XRF Accuracy	30
4.2 – XRF: Estimate of Shale Mineralogy.....	31
4.2.1 – Clay Mineralogy and Chert.....	34
4.2.2 – Heavy Minerals	36
4.2.3 – Rare Earth Elements	39
4.3 – XRF: A Proxy for Organic Matter.....	40
4.4 – Grain Size Correlations.....	42

4.5 – Grain Size Parameters.....	44
4.6 – Chert as Indicator of Thermal Maturation	46
4.7 – Petrography.....	48
Chapter 5 - Conclusions.....	50
Chapter 6 - Further Research	51
References.....	52
Appendix A -.....	54

List of Figures

Figure 1. Map of U.S. Shale gas plays (EIA, 2011).	2
Figure 2. Graph depicting the positive relationship between amount of quartz and thermal maturity (Totten and Blatt, 1996).	4
Figure 3. South-north cross section through the Anadarko Basin (Sorenson, 2005).....	5
Figure 4. Map of geologic provinces of Oklahoma (Northcutt and Campbell, 1995).....	6
Figure 5. Stratigraphic column of the deposition of the Woodford shale modified from Johnson and Cardott (1992).	7
Figure 6. Distribution of Devonian black shales in the U.S. modified from Comer (2008).....	8
Figure 7. Woodford shale organic maturity map of Oklahoma based on vitrinite reflectance data. Modified from Comer (1992).	9
Figure 8. Regional isopach map of the Woodford shale (Comer, 2008).	10
Figure 9. Graph showing the relationship between weight percent heavy minerals and vitrinite reflectance (Coddington, 2013).....	11
Figure 10. Sampling location (blue arrow) of WF#5 Dwyer Mt (Ramirez-Caro, 2013).....	12
Figure 11. Regional map showing the study area and sample locations (black dots) (Ramirez-Caro, 2013).	14
Figure 12. Krumbein’s phi scale conversion equation and associated statistical equations (Folk, 1980).	18
Figure 13. Graph depicting the major element weight percent distribution among the ten Woodford samples.	20
Figure 14. Log scale graph depicting the trace element relative parts per million (ppm) distribution among the ten Woodford samples.	21
Figure 15. Photomicrograph of WF#3 Lela Rahm and location of EDS spectra. Red highlights the presence of the element silica, and green highlights the presence of the element aluminum.	24
Figure 16. EDS spectra for WF#3 Lela Rahm.....	24

Figure 17. Photomicrograph for WF#7 Chenoweth and associated spectra. The color red highlights the presence of silica (chert); green highlights the presence of aluminum (clay minerals).	25
Figure 18. EDS spectra for WF#7 Chenoweth.	25
Figure 19. Photomicrograph of WF#9 Ne Alden and associated spectra point. The color red highlights the presence of silica; the color green highlights the presence of aluminum.	26
Figure 20. EDS spectra for WF#9 Ne Alden.	26
Figure 21. Cumulative curve plot for WF#1 McCalla Ranch and associated ϕ locations and values.	29
Figure 22. Graph depicting the strong correlation observed between Si/Al and Si/K ratios.....	35
Figure 23. Graph depicting the correlation between the chert percent and the observed XRF Si/Al ratio.	36
Figure 24. Graph depicting the inverse correlation between titanium and chert weight percent.	37
Figure 25. Graph depicting the inverse correlation between iron and chert weight percent.	37
Figure 26. Graph depicting the inverse correlation between rubidium and chert weight percent.	38
Figure 27. Graph depicting the inverse correlation between zirconium and chert weight percent.	38
Figure 28. Graph depicting strong relationship of barium to rare earth element concentrations in the organic matter fraction of the samples.....	39
Figure 29. Graph depicting strong relationship of zinc to rare earth element concentrations in the organic matter fraction of the samples.....	40
Figure 30. Graph depicting strong relationship of sulfur to rare earth element concentrations in the organic matter fraction of the samples.....	40
Figure 31. Graph depicting the inverse correlation between organic matter weight percent and handheld XRF Si/Al ratio.	42
Figure 32. Graph depicting strong correlation between median and phi 50 (mean).....	44
Figure 33. Graph showing the location of ϕ 75 and its correlating phi value of approximately 9.4	46
Figure 34. SEM image comparison of samples containing the highest and lowest vitrinite values.	49
Figure 35. SEM image comparison of samples containing the highest and lowest TOC values.	49

List of Tables

Table 1. Location of samples and their stratigraphic units (Ramirez-Caro, 2013).....	13
Table 2. XRF major element raw data averages for the ten Woodford samples in relative weight %	19
Table 3. XRF trace element relative parts per million (ppm) raw data for the ten Woodford samples.....	19
Table 4. Residue proportions in the Woodford samples after initial fusion procedure.	22
Table 5. Estimated percent of chert in the Woodford samples after fusion and sieving.	23
Table 6. Table depicting grains sizes (phi) and cumulative percents for the ten Woodford samples.....	28
Table 7. Table depicting the data calculated from the cumulative curves for each sample.....	30
Table 8. Table displaying the elemental precision of the handheld XRF.	31
Table 9. Correlation matrix of major and trace element data analyzed.	33
Table 10. Major element analytical results of the organic portion of the Woodford samples from Ramirez (2013).	41
Table 11. Correlation matrix of the size data analyzed.	43

Acknowledgements

I would like to thank Dr. Matt Totten for taking me on as a graduate student, always being available to talk about my thesis, and putting up with my obnoxious amounts of ‘that’s what she said’ jokes. I would also like to thank Dr. Sambhudas Chaudhuri for all of his input and knowledge on clay mineralogy. I would like to thank Pamela Kempton for entrusting me to use her brand new handheld XRF.

Dedication

I would like to dedicate this work to my mudlogging friends at Canrig... thanks for helping me find my passion in the field of petroleum geology. Also, thanks for all the great memories and for supporting and encouraging me to embark on this journey...even though it was in Kansas (Andrea).

I dedicate this work to my fellow K-State Geology Masters class of 2015, I can't imagine going through this process with any other group...WE MADE IT!!

Chapter 1 - Introduction

Until recently, shales were regarded almost exclusively as organic-rich source and seal mudstones that were unworthy of research to the degree that other sedimentary rocks received (Potter, 1980). The use of horizontal drilling in conjunction with hydraulic fracturing has greatly expanded the ability of producers to profitably recover natural gas and oil from low-permeability geologic plays—particularly; shale plays. The proliferation of activity into new shale plays has increased dry shale gas production in the United States from 1.0 trillion cubic feet in 2006 to 4.8 trillion cubic feet, or 23 percent of total U.S. dry natural gas production, in 2010 (EIA, 2011).

The Woodford shale is recognized as an abundant source rock across Oklahoma and much of the midcontinent (Lambert, 1990), and up to 8% of the world's hydrocarbon reserves are estimated to have been sourced by the Woodford and its equivalents (Fritz et al, 1991). The Woodford shale has been recognized as one of the 'Magnificent Seven' gas shale plays in North America (Figure 1), accompanied by the Barnett, Fayetteville, Haynesville, Marcellus, Horn River, and Montney (Kuuskraa, 2011).

A shale can be defined as “any laminated, indurated (consolidated) rock with > 67% clay-sized materials” (Jackson, 1997). Shales are commonly formed from the compaction of silt and clay sized mud particles, primarily clay minerals such as illite, kaolinite, and smectite. Other mineral particles found in shales are quartz, feldspar, and chert, which average 1/3 of the rock (Blatt, 1981). With a composition predominantly of clay and mud particles, shales are often placed into the mudstone category; however shales are commonly fissile and laminated which helps distinguish them from other mudstones (King, 2005).

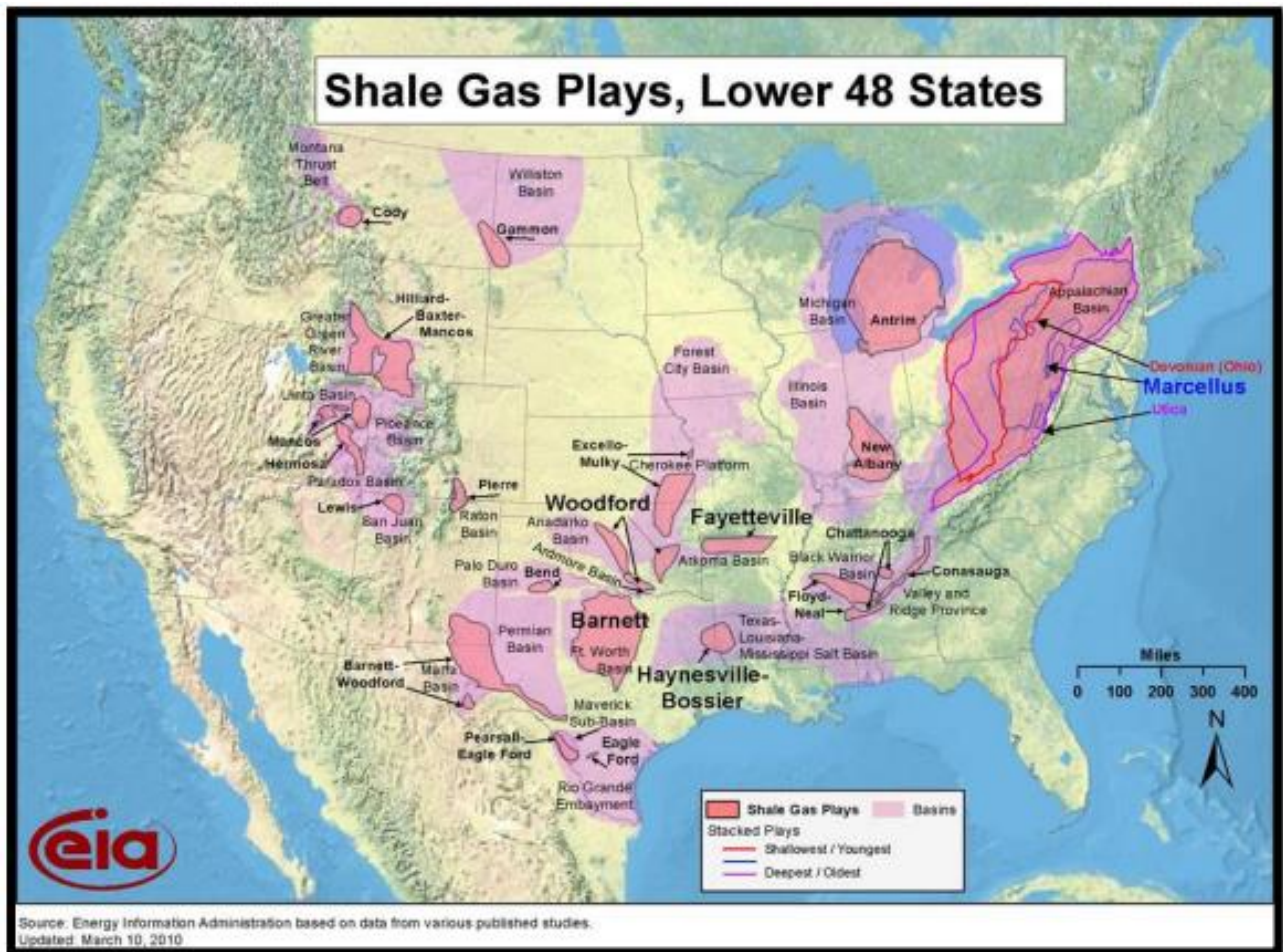


Figure 1. Map of U.S. Shale gas plays (EIA, 2011).

Mudrocks are less well understood than their coarser-grained (sandstone) counterparts even though they comprise over 60% of the sedimentary column (Totten and Hanan, 1998). Most petrologic mudrock studies have had a focus on clay mineralogy, with the non-clay minerals receiving minimal research (Coddington, 2013). The goal of this study is to analyze chert particles located within shale rocks of the Woodford shale in the Anadarko basin of Oklahoma. In this study shale samples have been disaggregated, and cherts separated out of the shale samples using a sodium bisulfate fusion technique adapted from Totten (1995). The cherts have

been analyzed by SEM. Whole-rock core analysis has been done using handheld XRF. No correlations were found to show that cherts are indicators of thermal maturity within the Woodford shale. Data collected with the handheld XRF displayed that it could be a useful tool for onsite analysis of unconventional targets.

1.1 – Significance

Chert is a microcrystalline or cryptocrystalline sedimentary rock material composed of silicon dioxide (SiO_2), and is known for its conchoidal fracture and extreme hardness placing it about a 7 on Mohs scale (King, 2005). Due to its hardness and fracture patterns, chert has the ability to affect drilling and completion design, production practices and ultimately well productivity (Halliburton, 2011). Chert is known to play a large impact on drilling speed and efficiency, as it is commonly known to damage and destroy drill bits and cause slow drilling rates of penetration.

The significance of this study comes from the fact that Woodford shale is typically more complex than other Devonian black shales found in North America due to the presence of alternating bands of chert-like amorphous silica and silica-rich shale (Halliburton, 2011). Analysis of chert and its possible role in gas generation and storage in shales has been largely overlooked. Fishman et al. (2010), conducted a study on Woodford shale chert beds from outcrops in the Arbuckle Mountains of Oklahoma and concluded that the quartz found in cherts of the Woodford formed diagenetically from the recrystallization of radiolarian skeletal parts. They also hypothesized that, due to their rigid fabric, the petrophysical characteristics of cherts in the Anadarko basin (compared to the Arbuckle) likely only underwent minor changes, whereas the mudstones underwent major changes due to compaction and compression, causing a

collapse of the ductile constituents. This lead to the final hypothesis that ‘the potential for Woodford cherts to better retain porosity, coupled with their contained TOC, may provide important overlooked intervals of gas generation and overall gas storage in the formation, which may be contributing significant portions of the gas being produced from the formation’.

Previous studies have been conducted to analyze the role of silica and quartz in relation to diagenesis of shales. Totten and Blatt (1996) conducted a study of silica and polycrystalline quartz within the Stanley formation (Mississippian) in the Ouachita Mountains of southeastern Oklahoma and southwestern Arkansas. Results of this study showed that the quartz fraction increased in size, amount, and polycrystallinity with increasing thermal maturity (Figure 2). Through analysis of chert fractions within the Woodford shale we may be able to obtain a better understanding of the role cherts play in relation to thermal maturity.

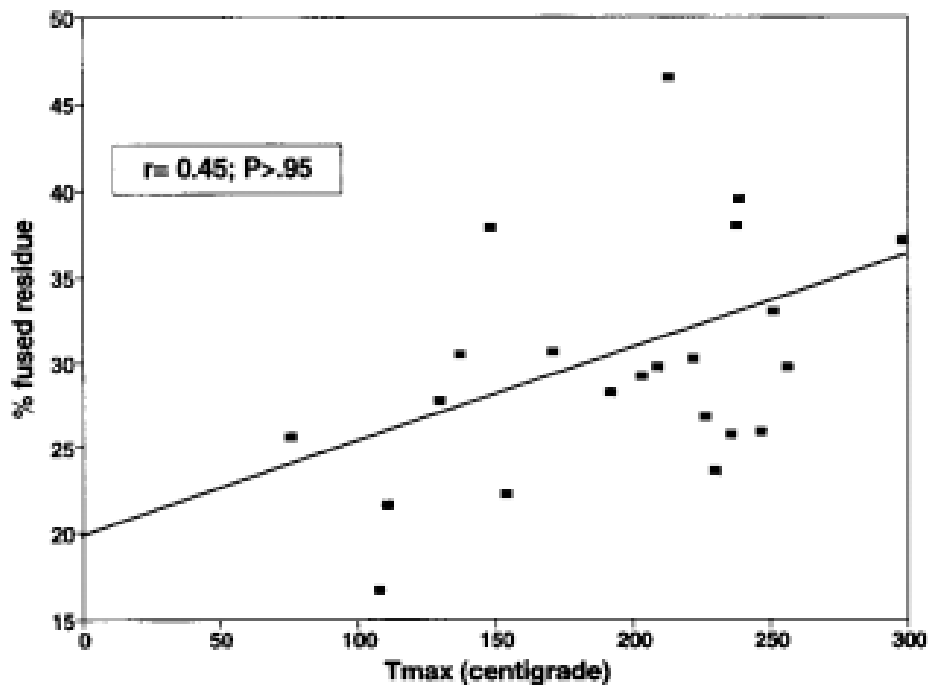


Figure 2. Graph depicting the positive relationship between amount of quartz and thermal maturity (Totten and Blatt, 1996).

1.2 – Geologic Setting

The greater Anadarko basin province covers almost the entire western part of Oklahoma, the southwestern part of Kansas, the northeastern part of the Texas Panhandle, and the southeastern corner of Colorado (Davis and Northcutt 1989). The basin is axially asymmetric and of Paleozoic age (Figure 3) (Cardott and Lambert, 1985).

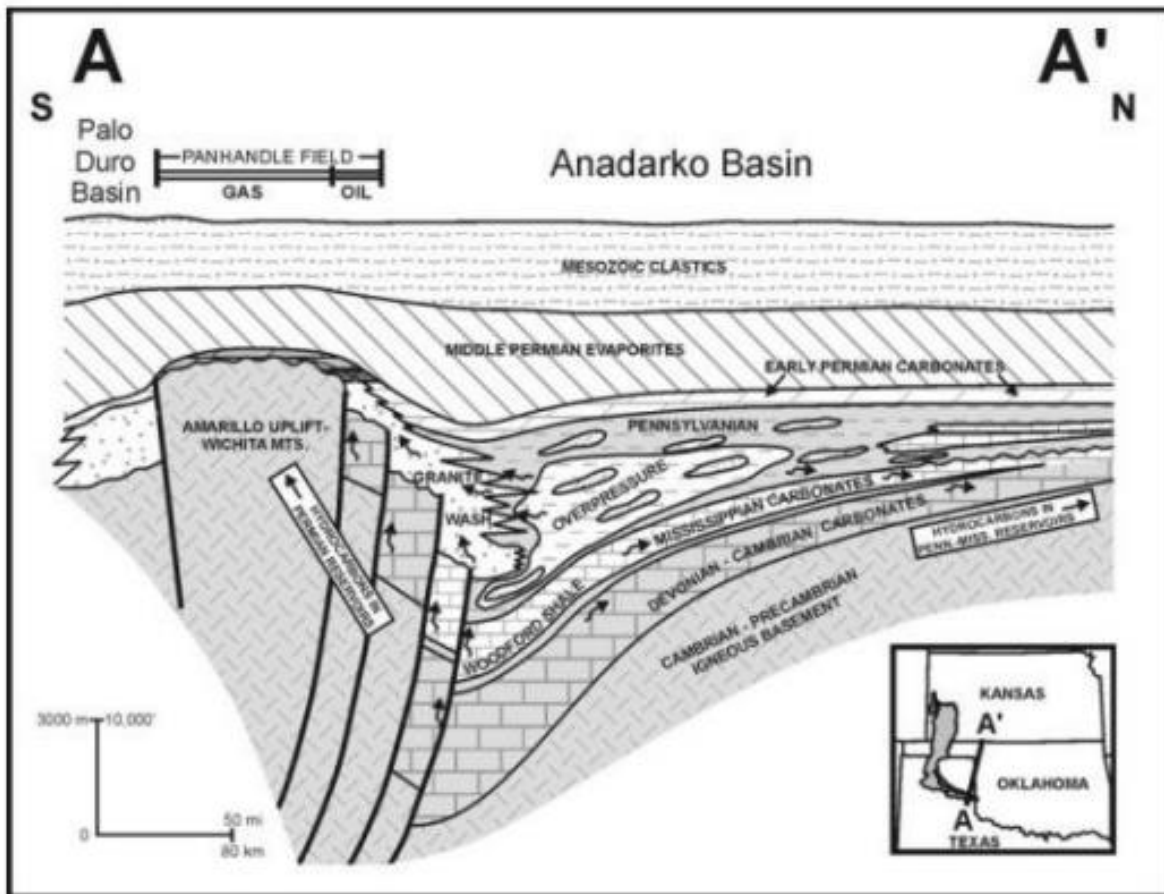


Figure 3. South-north cross section through the Anadarko Basin (Sorenson, 2005).

The province is bounded by major uplifts--the Wichita-Amarillo Uplift to the south, the Cimarron and Las Animas Arches to the west, the Central Kansas Uplift to the north, the Pratt Anticline to the northeast, the Nemaha Uplift to the east, and the Southern Oklahoma fold belt to the southeast (Figure 4). Most strata range in age from Cambrian to Permian with some minor

occurrences of Mesozoic and Cenozoic strata in the northwestern part of the province. Mississippian and older rocks are predominately carbonates, whereas Pennsylvanian and younger rocks are mostly shales with some sandstones. The Anadarko basin has 25 identified oil and gas plays, with 24 being conventional plays and the only unconventional play being the Woodford/Chattanooga/Arkansas Novaculite of the Midcontinent.

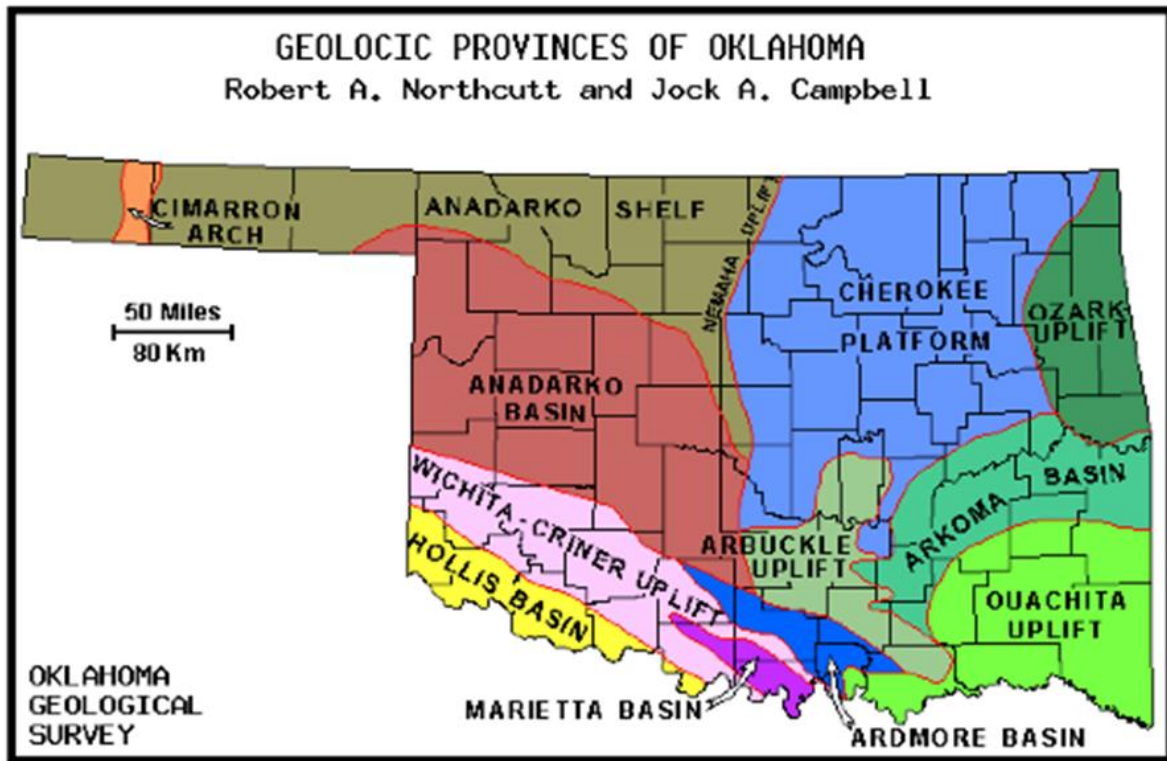


Figure 4. Map of geologic provinces of Oklahoma (Northcutt and Campbell, 1996).

The Woodford shale is considered to be one of the most important hydrocarbon source rocks in the province. The Woodford shale is of a deep marine depositional environment, and was deposited during the late Devonian into the early Mississippian (Figure 5). The late Devonian saw the transgression of a euxinic ocean from the south-southwest, which resulted in the deposition of organic rich dark gray to black silt and clay sediments, which make up the Woodford shale (Kirkland, 1992).

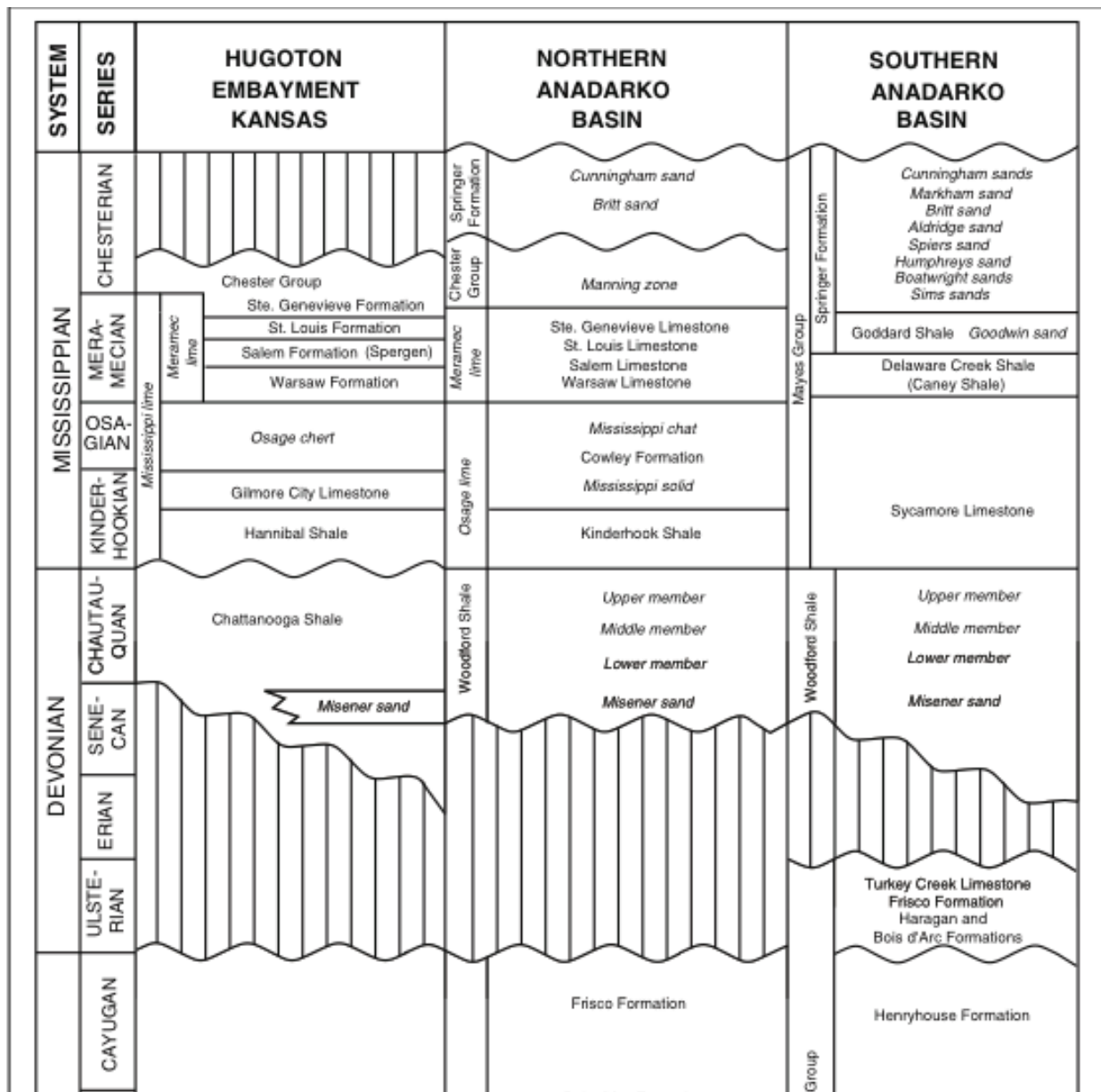


Figure 5. Stratigraphic column of the deposition of the Woodford shale modified from Johnson and Cardott (1992).

The Woodford shale is stratigraphically equivalent to various other Devonian black shales seen in North America (Figure 6). While the Woodford may be stratigraphically equivalent, the geological settings present in Oklahoma at the time of deposition were different than those of the other Devonian black shales. This difference is observed within the range of thermal maturities observed within the Woodford; with the highest thermal maturities found in

the deepest parts of the basin, and the lowest maturities found at the structural highs (Henry and Hester 1995) (Figure 7).

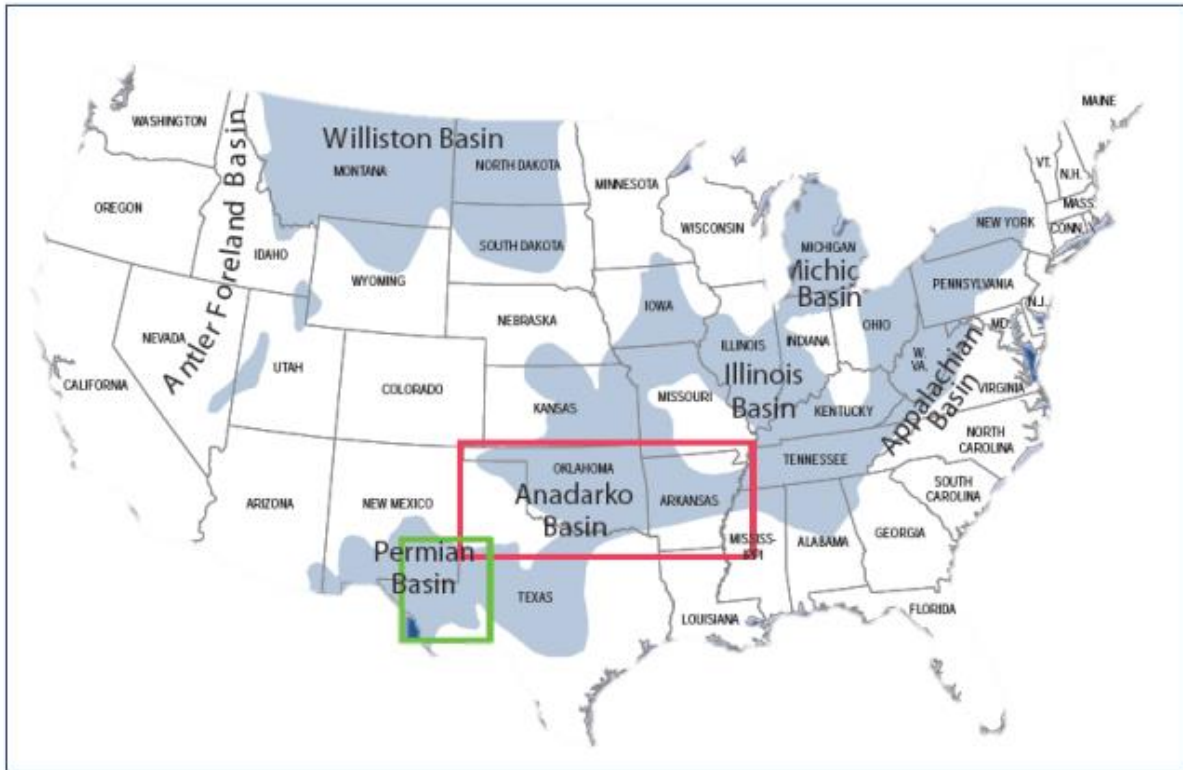


Figure 6. Distribution of Devonian black shales in the U.S. modified from Comer (2008).

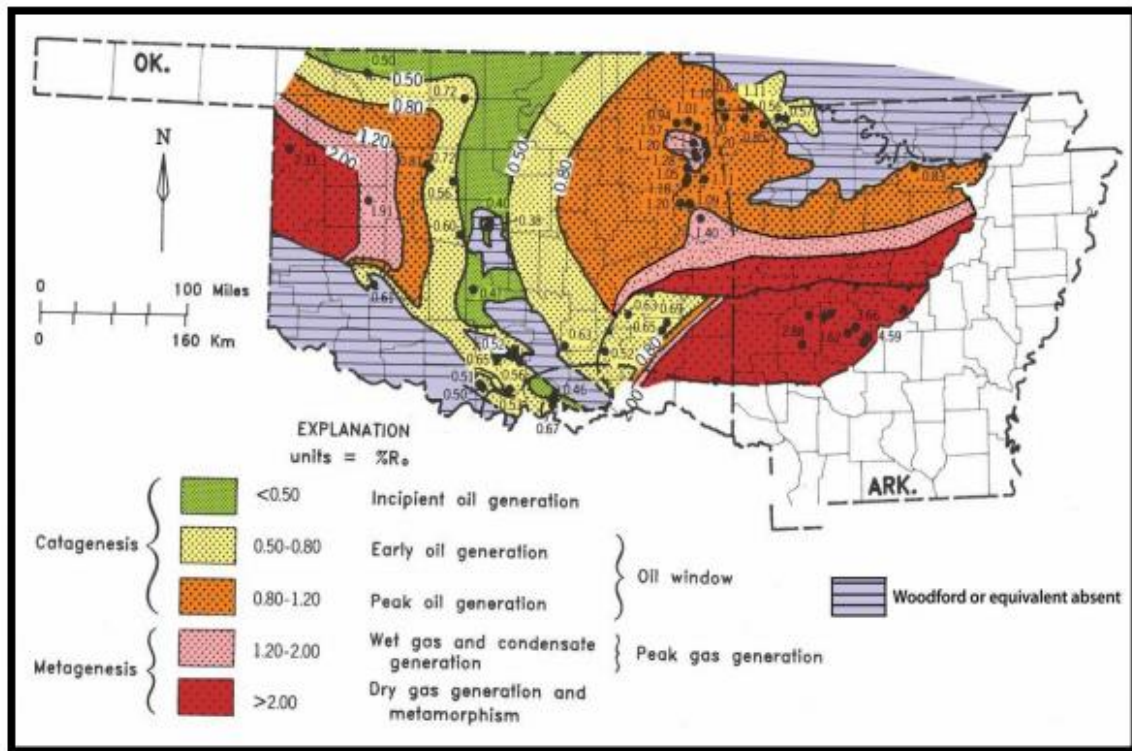


Figure 7. Woodford shale organic maturity map of Oklahoma based on vitrinite reflectance data. Modified from Comer (1992).

The Woodford ranges in thickness from nearly zero to upwards of 900 feet throughout the basin (Figure 8). The organic-matter is believed to be a mixture of type II and type III kerogens (Henry and Hester, 1995). The Woodford shale dips into the Anadarko basin with subsurface depths ranging from 4,000-25,000 feet, which allows for the broad range of thermal maturities seen within (Hester et al., 1990).

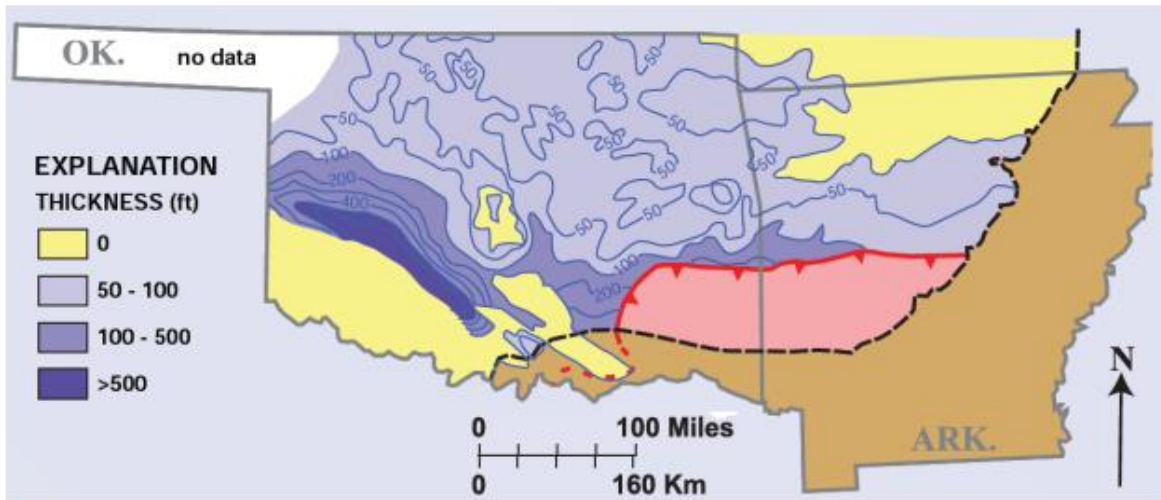


Figure 8. Regional isopach map of the Woodford shale (Comer, 2008).

1.3 – Previous Work

Daniel Ramirez-Caro (2013) conducted a study of REE patterns and total organic matter concentrations of 10 Woodford shale samples, through separation of organic matter from the shale. His total REE sum results in the organic matter of the samples contained a range from 300-800 ppm which are values greater than the average found in modern day shales and plants. These values were interpreted to represent exchanges of REE from associated sediments with the buried Woodford organic matter in post-depositional environment conditions. Using this observed data it was suggested that distribution patterns of the REE were influenced by both source and burial effects of the deposited organic material in association with the inorganic constituents.

Kacee Coddington (2013), using the same 10 Woodford samples as Ramirez-Caro, conducted a study analyzing the heavy minerals within the Woodford in hopes of obtaining a better understanding of the diagenetic changes that occurred after deposition, and how they might be related to the generation of hydrocarbons. Results of this study concluded that the

largest heavy mineral constituent was pyrite, and that it contributed to approximately 66% of the heavy mineral fraction observed. Fe-mica is the second largest constituent observed. The morphology of the pyrite was related to thermal maturity, with the most mature rocks showing euhedral pyrite crystals.

Coddington (2013) compared her findings with the TOC, vitrinite reflectance, depth and location within the basin, and REE variation data from Ramirez-Caro's 2013 study of the same samples. It was noted that samples with higher percentages of heavy minerals were more thermally mature (Figure 9). It was hypothesized that as a rock becomes overly mature, the percent of heavy minerals present will continue to increase. No correlation was observed relating the percentage of heavy minerals to depth or TOC. It was hypothesized that thermal maturity is a controlling factor in the release of iron and sulfur, resulting in pyrite growth, which is observed to significantly contribute to the heavy mineral percentages found within the Woodford samples.

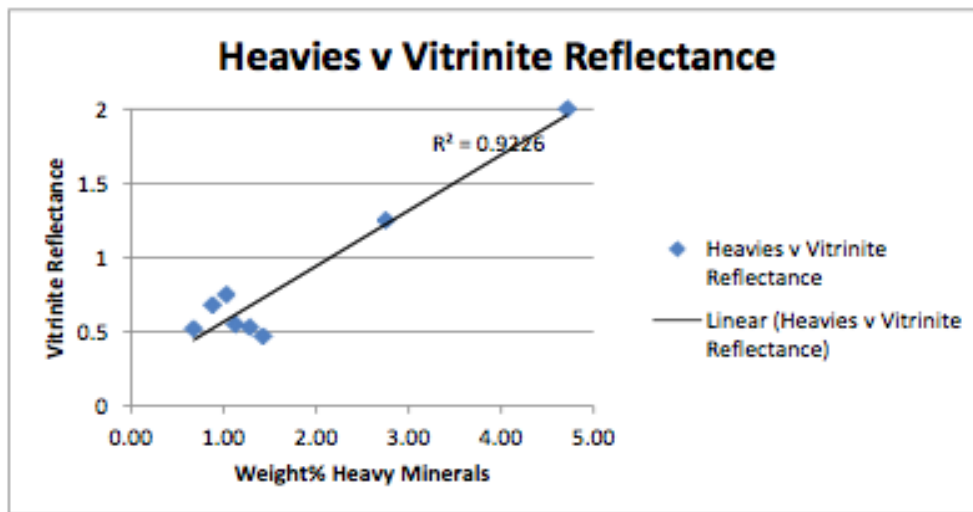


Figure 9. Graph showing the relationship between weight percent heavy minerals and vitrinite reflectance (Coddington, 2013).

Chapter 2 - Methodology

2.1 – Sample Selection

The samples for this study were chosen due to their availability and previous research. The samples were collected by Daniel Ramirez-Caro (2013) in the fall of 2011 from the core library at the OPIC (Oklahoma Petroleum Information Center) in the Oklahoma Geological Survey. The goal was to obtain samples with a wide spatial distribution throughout north central Oklahoma. Samples were chosen based on availability and visible characteristics; with the main objective being to collect clean, black shale samples estimated to contain the highest content of organic matter. Ramirez-Caro selected samples from 10 wells, and collected approximately 90 grams of sample from each core (Figure 10).



Figure 10. Sampling location (blue arrow) of WF#5 Dwyer Mt (Ramirez-Caro, 2013).

The 10 wells are located throughout eight counties in north central Oklahoma, and come from various depths ranging from approximately 4,100 feet to 17,000 feet (Table 1). The 10

core sample locations for this project can be seen depicted in Figure 11 by black markers. The green markers depict oil samples collected and used by Ramirez-Caro (2013).

Sample Name	Latitude	Longitude	Section	TWP	RNG	County	Sample Depth(ft)	Formation
WF # 1 Shell McCalla Ranch	35.0912	-97.78539	12	07N	06W	GRADY	12309	Woodford
WF # 2 Mobil Sara Kirk	36.72669	-97.93513	15	26N	07W	GRANT	5567	Woodford
WF # 3 Mobil Rahm Lela	36.5809	-97.82898	03	24N	06W	GARFIELD	6729	Woodford
WF # 4 Shell Guthrie	36.25138	-97.45871	31	21N	02W	NOBLE	4165	Woodford
WF # 6 Mobil Cement Ord	34.90223	-98.07862	18	05N	08W	GRADY	17581	Woodford
WF # 5 Mobil Dwyer Mt	36.23352	-98.22134	01	20N	10W	MAJOR	8716.5	Woodford
WF # 7 Amerada Chenoweth	36.40693	-97.73539	04	22N	05W	GARFIELD	6513	Woodford
WF # 8 Apexco Curtis	35.39349	-97.72205	27	11N	05W	CANADIAN	8520	Woodford
WF # 9 Jones and Pellow	35.03079	-98.53458	35	07N	13W	CADDO	6793	Woodford
WF # 10 Lonestar Hannah	36.15513	-99.79674	06	19N	24W	ELLIS	14323	Woodford

Table 1. Location of samples and their stratigraphic units (Ramirez-Caro, 2013).

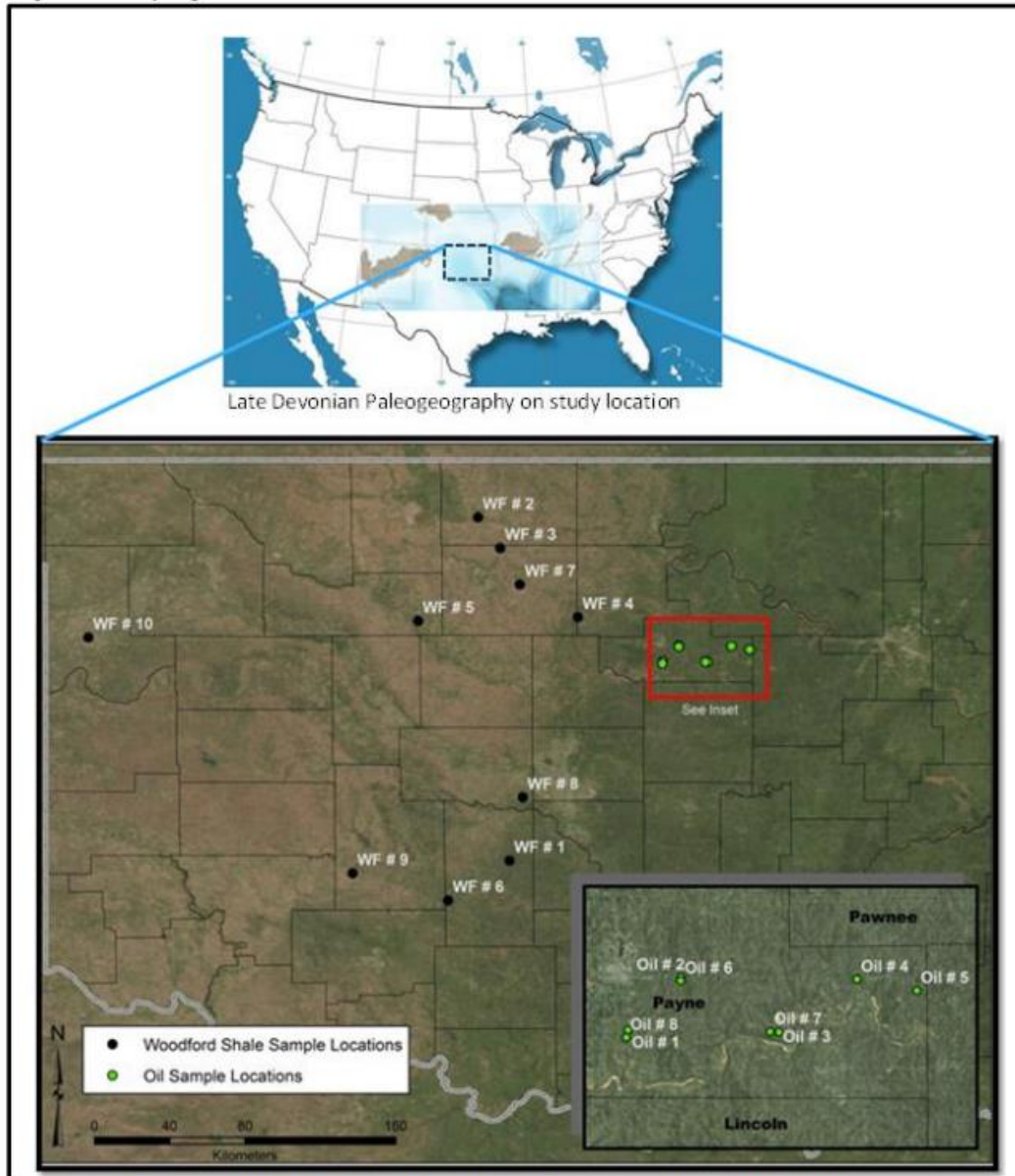


Figure 11. Regional map showing the study area and sample locations (black dots) (Ramirez-Caro, 2013).

2.2 – Whole Rock XRF Analysis

X-ray Fluorescence (XRF) was performed on the 10 whole rock samples to obtain bulk elemental composition using a Bruker Tracer III handheld XRF. No sample preparation was needed, as the analysis is nondestructive to the object being analyzed. In recent years the

handheld XRF has emerged as a beneficial analytical tool for quick, on-site analysis; however, it is important to note that due to their low penetrating power and low energy, light element readings (i.e. elements with an atomic weight less than Mg) will be almost immeasurable when analyzed in air. This issue can be solved by using helium as a controlled atmosphere in the chamber to eliminate the dispersing effect of the air, which would then allow for small readings of the lighter elements. At the time of analysis, the handheld XRF was newly acquired, and so no helium purge was available for use.

Trace element analysis was first conducted on the samples, and the Bruker mudrock calibration was used. The settings used were yellow filter (12 mil Al + 1 mil Ti), 40kV, 12.4 μ A, and 60 second intervals. Five randomly selected surfaces were analyzed on each sample to obtain an average bulk chemical analysis. Trace element peaks were generated and identified in the S1PXRF program provided by Bruker, and relative weight percentages for each element were calculated from the data. The weight percent values produced from elemental analyses were then averaged and converted to parts per million (ppm) to calculate the bulk trace element composition for each sample.

For major element analysis with the handheld XRF the yellow filter was removed and the instrument was connected to a vacuum to remove the air between the XRF window and the x-ray detector. The settings were readjusted so that sampling intervals were 180 seconds at 15kV and 25 μ A. Once again, each whole rock sample was analyzed on five randomly selected surfaces and run through the S1PXRF program to identify element peaks and calculate weight percent values. The weight percent values were then averaged to show the bulk major element composition for each sample.

Once all major and trace element data was collected, plots were generated in Microsoft Excel to show bulk element composition of each whole rock sample. Additional plots were also generated to better articulate any significant elemental changes that were observed between samples.

2.3 – Sodium Bisulfate Fusion

A sodium bisulfate fusion technique adapted from Blatt et al., (1982) and Totten et al., (1995) was performed to separate the chert from the mudrock whole samples.

In preparation for fusion, samples were crushed using a mortar and pestle until fragments could pass through a 300 μ m sieve screen. 0.4g of sample was weighed and placed in a nickel crucible. 4.0g of anhydrous sodium bisulfate (NaHSO₄) was added to the sample, followed by a few drops of distilled water to wet the mixture. The crucible was placed above a Meker burner and heated slowly to avoid overflow of sample during frothing. Gentle heating of the bottom and sides of the crucible continued until all frothing stopped. Upon completion of the frothing, the crucible was lowered closer to the Meker burner, and the sample was fused for 15 minutes using the maximum heat of the burner. After fusing, the crucible was removed from heat and allowed to cool before being transferred to a 1000mL beaker containing 300mL of 1.0N HCl. The beaker was heated using a hotplate until the fused cake sufficiently dissolved from the crucible. The crucible was removed and washed using 1.0N HCl, and heating continued until all of fusion cake was entirely dissolved. The beaker was removed from heat and allowed to cool, and the HCl was filtered using a suction filter apparatus and chemically resistant 0.42 μ m millipore filter. Using alternate washings of distilled water and 1.0N HCl, the filtrate was washed 3 times. The filtrate was next transferred into 300mL 0.5N NaOH and boiled for 20 minutes on a hotplate.

Upon cooling, the filtrate residue was filtered using a new 0.42 μm millipore filter. The residue was washed once with 0.5N NaOH, followed by 3 alternate washings of 1.0N HCl and distilled water. The residue was air dried, and a final weight measured. Calculations were performed to depict the chert/silica weight percentage of the whole rock fractions.

2.4 – FESEM

Field emission scanning electron microscopy (FESEM) was conducted on the ten fused samples to help identify mineralogy, size, and shape of the cherts and possible organics. Dr. Dan Boyle of the Kansas State University Department of Biology operated the FESEM. Carbon conductive double coated spectro tabs were placed on specimen stubs, and the adhesive was dipped into the fused sample. No coating was applied to the samples, and the techniques performed for mineral identification were backscatter electron imaging and energy dispersive spectra (EDS). Mixed images were generated in INCA software to help illustrate silica and carbon concentrations. EDS spectra charts were also created in INCA to illustrate individual spectra and sum spectra.

Point counting was conducted directly on the photomicrographs to determine sizes (μm) of chert grains present. Krumbein's phi scale was then applied to the size data and for each well and cumulative size distribution curves were generated. These charts were then used to calculate graphic mean, median, mode, inclusive standard deviation, inclusive graphic skewness, and kurtosis. The equations used for calculations can be seen in Figure 12.

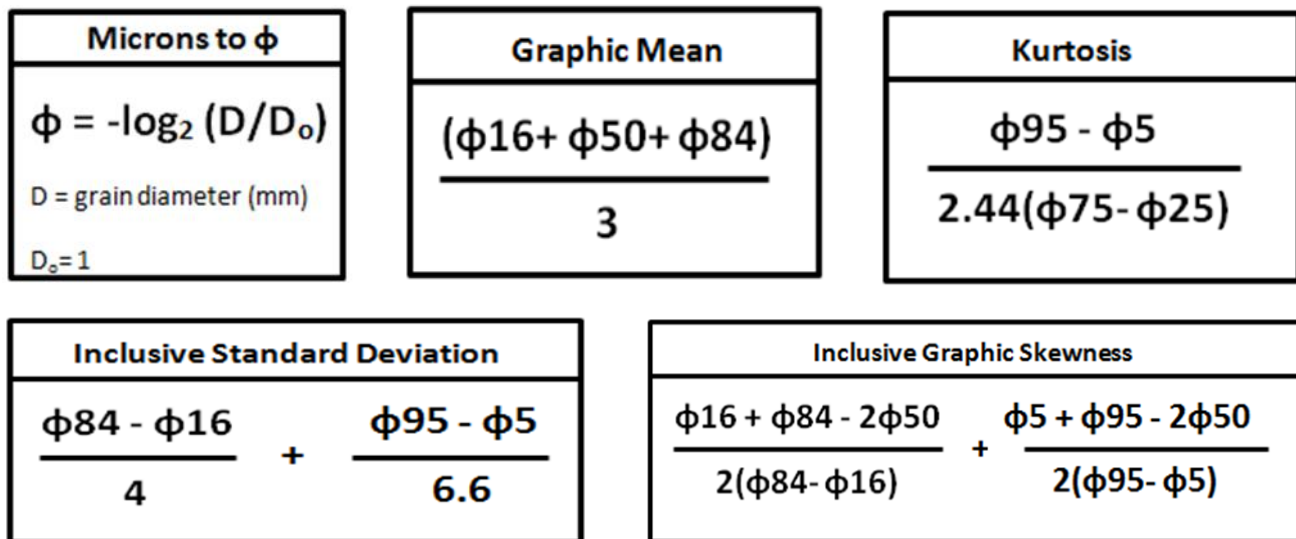


Figure 12. Krumbein’s phi scale conversion equation and associated statistical equations (Folk, 1980).

Chapter 3 - Results

3.1 Whole Rock XRF Analysis

At the time of analysis the calibration that came with the handheld XRF had yet to be tested. Therefore, while we can comment on the internal precision of our analysis at this time, we cannot testify as to their accuracy. However, all the data obtained in this study will be internally consistent, so comparisons within this sample set are still significant.

The results of the handheld XRF for both major and trace elements are presented in Tables 2 and 3. The data were then converted to charts to better depict elemental variations amongst the samples (Figures 13, 14). Standard deviation values were plotted for each element upon averaging the five runs performed on each sample.

Sample	Time	NaKa1	MgKa1	AlKa1	SiKa1	P Ka1	S Ka1	K Ka1	CaKa1	BaLa1	TiKa1	V Ka1	CrKa1	MnKa1	FeKa1	CoKa1	NiKa1	CuKa1	ZnKa1
WF#1 McCalla Ranch Avg	180	0.55	0.77	5.26	19.35	0.01	0.55	2.33	2.07	0.03	0.34	0.01	0.01	0.02	1.86	0.00	0.01	0.01	0.01
WF#2 Sara Kirk Avg	180	0.54	1.43	4.37	15.20	0.06	0.65	2.34	6.74	-0.02	0.22	0.00	0.00	0.06	2.29	0.00	0.00	0.00	0.01
WF#3 Lela Rahm Avg	181	0.46	1.37	6.94	22.52	0.04	1.82	3.46	2.05	0.00	0.36	0.01	0.01	0.03	3.94	0.00	0.01	0.01	0.01
WF#4 Guthrie Avg	180	0.57	0.51	2.51	14.51	6.69	1.80	1.50	3.67	-0.05	0.23	0.03	0.02	0.02	3.77	0.00	0.01	0.02	0.06
WF#5 Dwyer Mt Avg	180	0.47	0.94	5.88	29.47	0.05	1.33	3.01	0.81	-0.03	0.31	0.04	0.01	0.03	2.38	0.00	0.01	0.01	0.02
WF#6 Cement Ord Avg	180	0.39	0.75	3.46	30.10	0.11	4.68	1.23	0.17	0.88	0.12	0.24	0.00	0.03	1.75	0.00	0.01	0.05	0.19
WF#7 Chenoweth Avg	180	0.48	0.91	4.89	29.42	0.05	1.98	2.75	0.53	-0.05	0.28	0.05	0.01	0.02	2.52	0.00	0.01	0.00	0.01
WF#8 Curtis Avg	180	0.48	1.10	6.32	22.28	0.06	2.69	2.73	1.33	0.01	0.35	0.03	0.01	0.03	2.70	0.00	0.01	0.01	0.01
WF#9 Ne Alden Avg	181	0.41	0.54	1.72	28.52	0.03	1.54	0.60	0.15	-0.07	0.09	0.05	0.01	0.03	0.41	0.00	0.01	0.01	0.03
WF#10 Hannah Avg	181	0.56	1.04	6.22	18.68	0.02	0.67	3.44	4.52	0.07	0.36	0.00	0.01	0.02	3.63	0.00	0.00	0.00	0.01

Table 2. XRF major element raw data averages for the ten Woodford samples in relative weight %

Sample	Time (s)	Ba	Cr	Mn	Ni	Cu	Zn	Rb	Sr	Zr
WF#1 McCalla Ranch	60	292.52595	23.702178	211.45713	88.099782	86.911751	131.1556	163.11939	71.727898	141.03701
WF#2 Sara Kirk	60	483.22875	35.149555	1227.4572	28.457955	6.7754499	37.634916	116.52234	158.60542	100.38306
WF#3 Lela Rahm	60	714.50946	99.643407	358.67768	88.606658	50.651169	129.8977	162.98596	60.832433	137.52092
WF#4 Guthrie	60	138.17625	217.02009	193.53521	85.891649	8.0865069	174.19985	112.0692	46.286229	39.545106
WF#5 Dwyer Mt	60	338.94477	86.136771	248.94138	175.09451	63.064001	145.55039	139.26142	69.02429	107.24744
WF#6 Cement Ord	60	14274.084	205.89471	162.54005	157.52673	168.26108	1438.9287	51.562606	42.240168	42.945728
WF#7 Chenoweth	60	36.903255	107.3292	181.79675	177.47043	21.05893	142.46151	149.8625	55.664945	131.13941
WF#8 Curtis	60	978.5384	80.021437	235.06605	138.89475	178.66506	271.64085	168.00742	218.69555	162.11561
WF#9 Ne Alden	60	155.76734	80.927618	137.20792	108.97108	76.459764	254.83202	39.845014	30.073584	34.660979
WF#10 Hannah	60	1042.3133	71.394987	382.52961	40.312799	4.2616583	46.492207	179.49014	68.241759	167.71679

Table 3. XRF trace element relative parts per million (ppm) raw data for the ten Woodford samples.

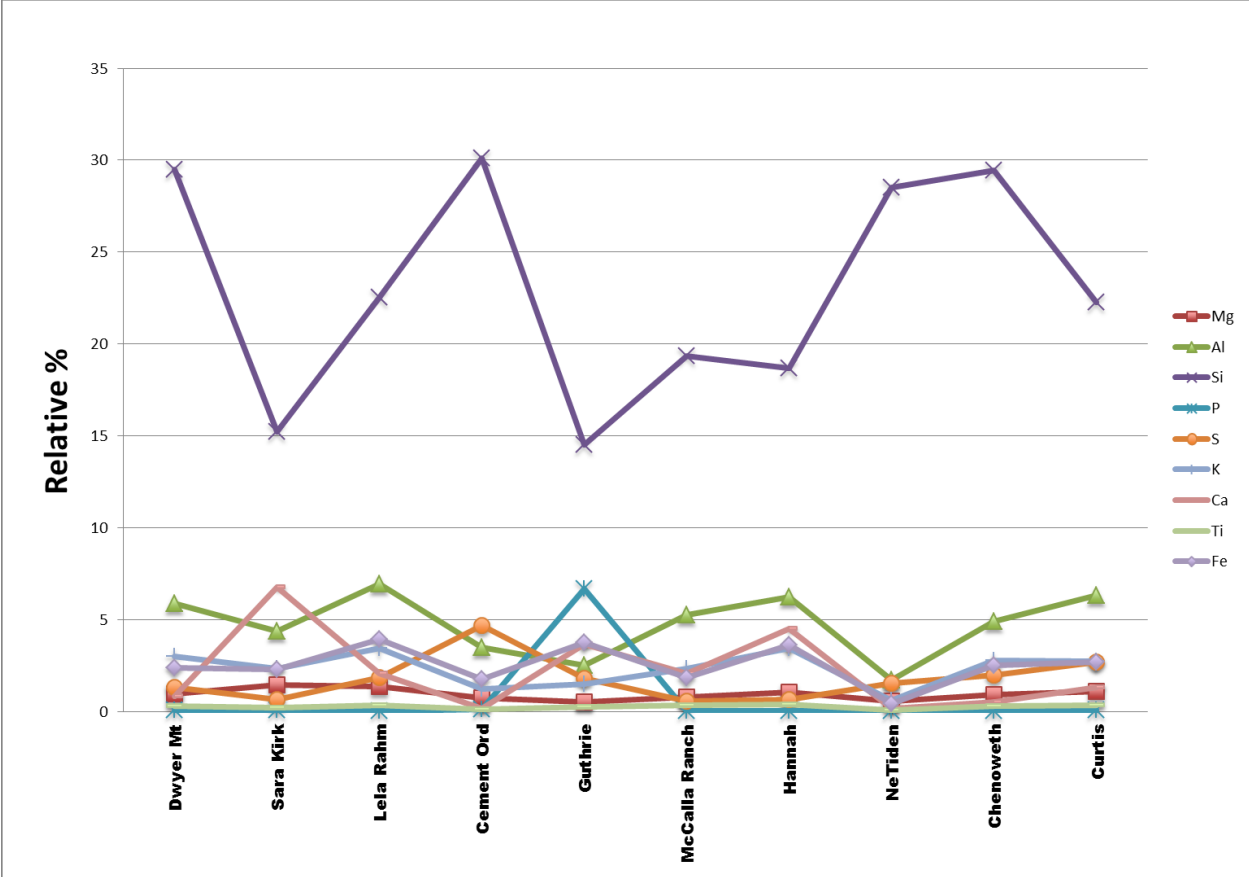


Figure 13. Graph depicting the major element weight percent distribution among the ten Woodford samples.

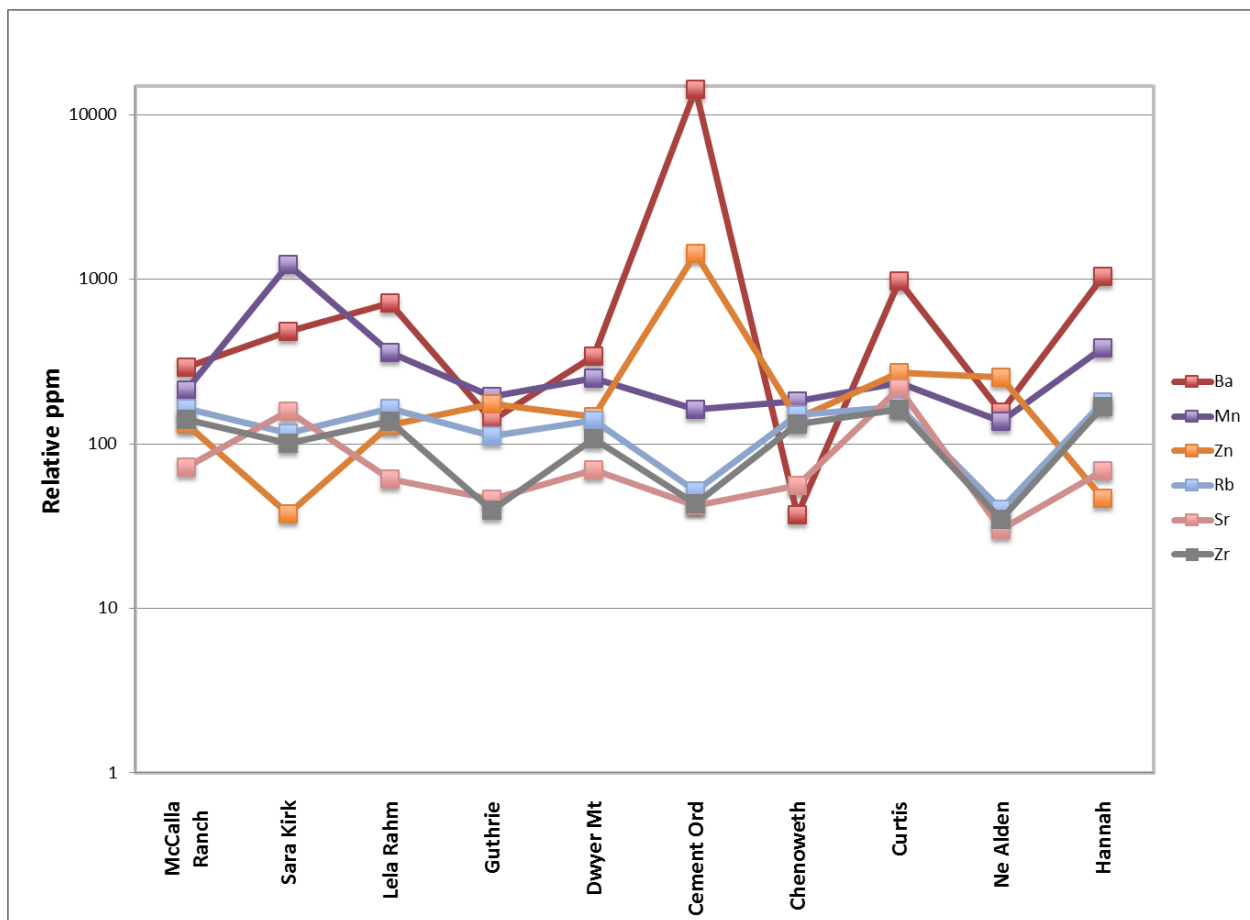


Figure 14. Log scale graph depicting the trace element relative parts per million (ppm) distribution among the ten Woodford samples.

3.2 Sodium Bisulfate Fusion

The initial results of the sodium bisulfate fusion procedure are presented in Table 4. The final weights of the samples appeared to be heavier than expected, and some large, dark grains were observed. It was hypothesized that these dark remaining grains observed were organic material. Observation under petrographic microscope, suggested that organic matter was still present. Observation under SEM, however, showed that many of these large fragments were shale particles and an incomplete fusion was confirmed. Totten et al., (1995) never conducted

this sodium bisulfate fusion procedure on organic-rich mudrocks, so it is possible that the organic matter interfered with the fusion.

The small sample size available precluded a repeat of the fusion experiment, and instead required attempts to isolate the chert using other methods. Had there been enough sample, treating the rock with hydrogen peroxide to remove the organic matter before fusion would have been a good alternative. Chert is expected to be very fine-grained in the black shales deposited under low-energy conditions; hence, it was inferred that the chert could be isolated from the unfused fragments from the fused residue via size separations. Wet sieving was conducted to separate the samples into three size fractions; $>63\mu\text{m}$, $20\ \mu\text{m} - 63\ \mu\text{m}$, and $<20\ \mu\text{m}$. The less than 20 micron was inferred to contain the chert fraction, hence the percentage of this fraction times the percentage of the fused residue was considered to be the corrected weight percentage of chert in each sample. These are presented in Table 5. The $<20\ \mu\text{m}$ fraction was examined by SEM analysis to confirm the isolation of chert from the rock samples.

SAMPLE	Sample wt (g)	Filter wt (g)	Sodium Bisulfate (g)	Final weight w/ filter (g)	Final weight w/o filter (g)	% of start wt
WF#1 McCalla Ranch	0.4	0.07	4.00	0.30	0.23	48.94%
WF#2 Sara Kirk	0.4	0.07	4.00	0.21	0.14	29.79%
WF#3 Lela Rahm	0.4	0.07	4.00	0.22	0.15	31.91%
WF#4 Guthrie	0.4	0.07	4.00	0.29	0.22	46.81%
WF#5 Dwyer Mt.	0.4	0.07	4.00	0.33	0.26	55.32%
WF#6 Cement Ord	0.4	0.07	4.00	0.31	0.24	51.06%
WF#7 Chenoweth	0.4	0.07	4.00	0.28	0.21	44.68%
WF#8 Curtis	0.4	0.07	4.00	0.25	0.18	38.30%
WF#9 Ne Alden Un	0.4	0.07	4.00	0.38	0.31	65.96%
WF#10 Hannah	0.4	0.07	4.00	0.19*	0.12	25.53%

Table 4. Residue proportions in the Woodford samples after initial fusion procedure.

	Seive start weight w/o filter	>63 μm w/o filter (g)	>63 % start sieve wt	20-63 μm w/o filter (g)	20-63 % start sieve wt	<20 μm w/o filter (g)	<20 % start sieve wt	Adjusted % Silica
WF#1 McCalla Ranch	0.19	0.11	57.89	0.03	15.79	0.05	26.32	33.29
WF#2 Sara Kirk	0.10	0.07	70.00	0.01	10.00	0.02	20.00	20.27
WF#3 Lela Rahm	0.12	0.06	50.00	0.03	25.00	0.03	25.00	21.71
WF#4 Guthrie	0.20	0.13	65.00	0.04	20.00	0.03	15.00	31.85
WF#5 Dwyer Mt	0.17	0.10	58.82	0.05	29.41	0.02	11.76	37.64
WF#6 Cement Ord	0.19	0.13	68.42	0.04	21.05	0.02	10.53	34.74
WF#7 Chenoweth	0.13	0.06	46.15	0.04	30.77	0.03	23.08	30.40
WF#8 Curtis	0.14	0.10	71.43	0.02	14.29	0.02	14.29	26.06
WF#9 Ne Alden	0.23	0.16	69.57	0.04	17.39	0.03	13.04	44.87
WF#10 Hannah	0.07	0.03	42.86	0.03	42.86	0.01	14.29	17.37

Table 5. Estimated percent of chert in the Woodford samples after fusion and sieving.

Although the estimated chert percentages calculated after the wet sieving produced results that fall within the range expected for the Woodford, this two-step approach introduces additional uncertainty in the estimates. The possibility for loss of sample, which could greatly impact calculated percentages since the sample weight was small to start with, could occur both in the transferring process and sieving procedure. Loss of sample impacting the final adjusted chert percentages can be observed in WF #10 Hannah, where an unknown sample amount was spilt in the fusion transfer. Therefore, the low estimated percentage for this sample is probably in error.

3.3 SEM with EDS Spectra

The SEM photomicrographs and associated EDS confirming chert grains for grain mounts of samples WF#3, WF#7 and WF#9 are presented below (Figures 15-20). The remaining images and spectra can be found in Appendix A. It should be noted that many of the chert grains have a coating of an aluminum-bearing phase, likely clay. This is not surprising given the wet sieving of chert and shale fragments. Some amount of clay was probably washed from the fragments during this process, and ended up as a coating on the chert grains. This is readily observed in the X-ray maps of Si and Al in Figures 15 and 17.

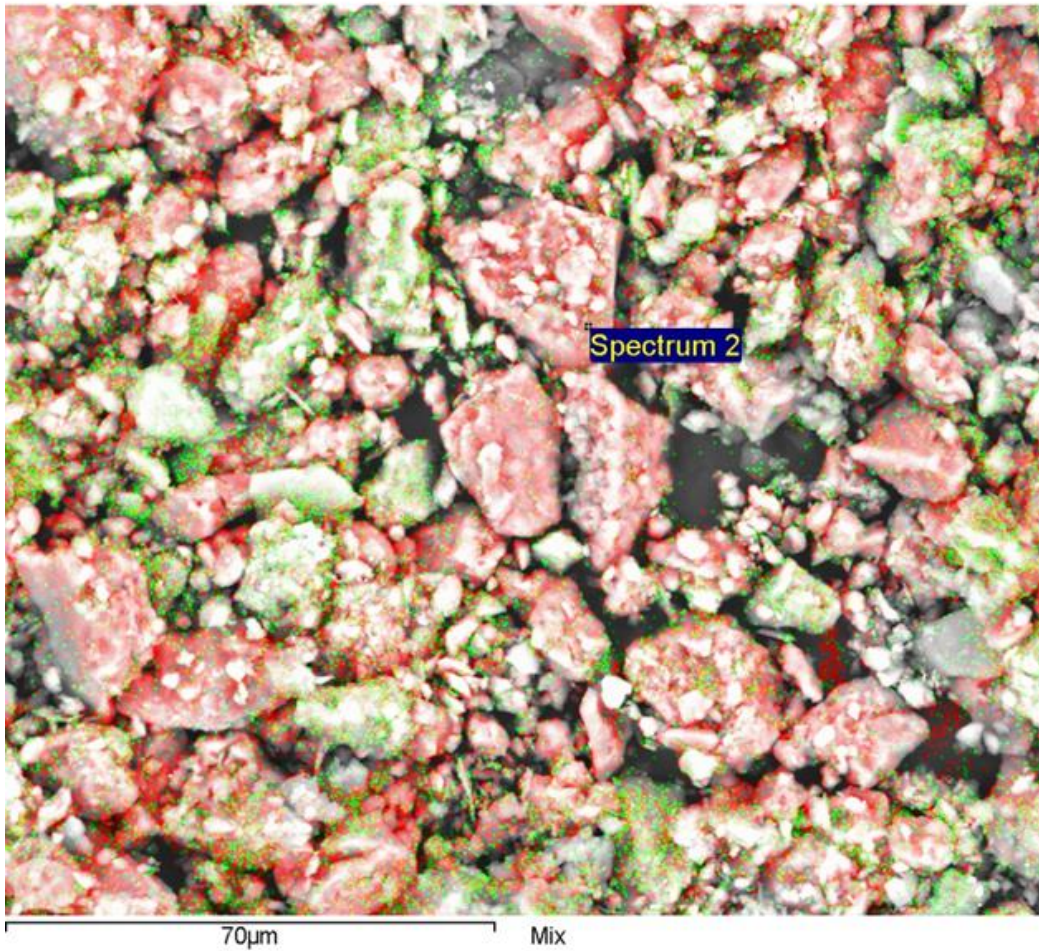


Figure 15. Photomicrograph of WF#3 Lela Rahm and location of EDS spectra. Red highlights the presence of the element silica, and green highlights the presence of the element aluminum.

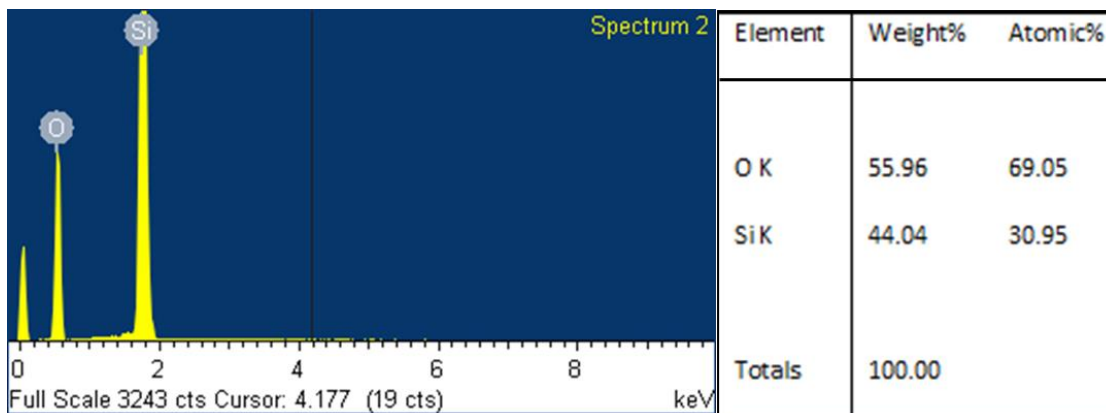


Figure 16. EDS spectra for WF#3 Lela Rahm

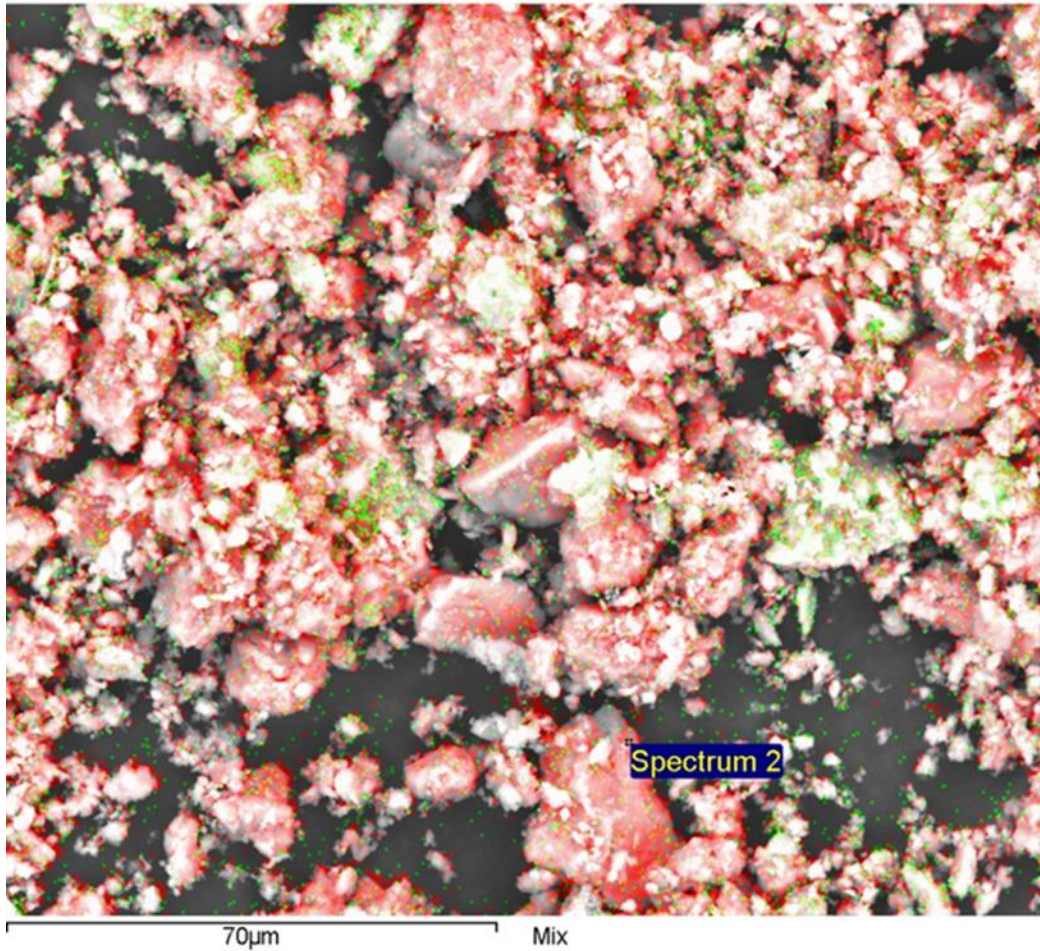


Figure 17. Photomicrograph for WF#7 Chenoweth and associated spectra. The color red highlights the presence of silica (chert); green highlights the presence of aluminum (clay minerals).

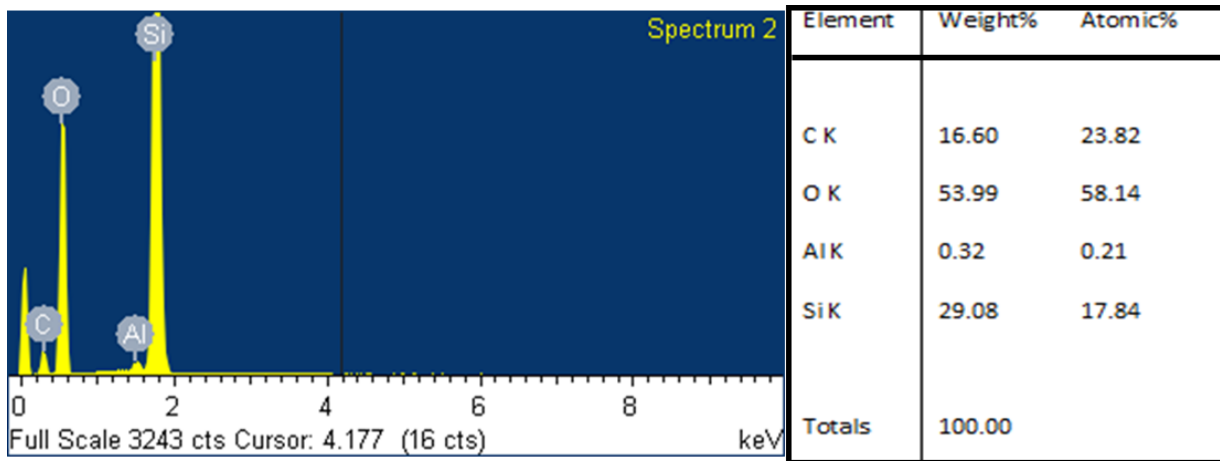


Figure 18. EDS spectra for WF#7 Chenoweth.

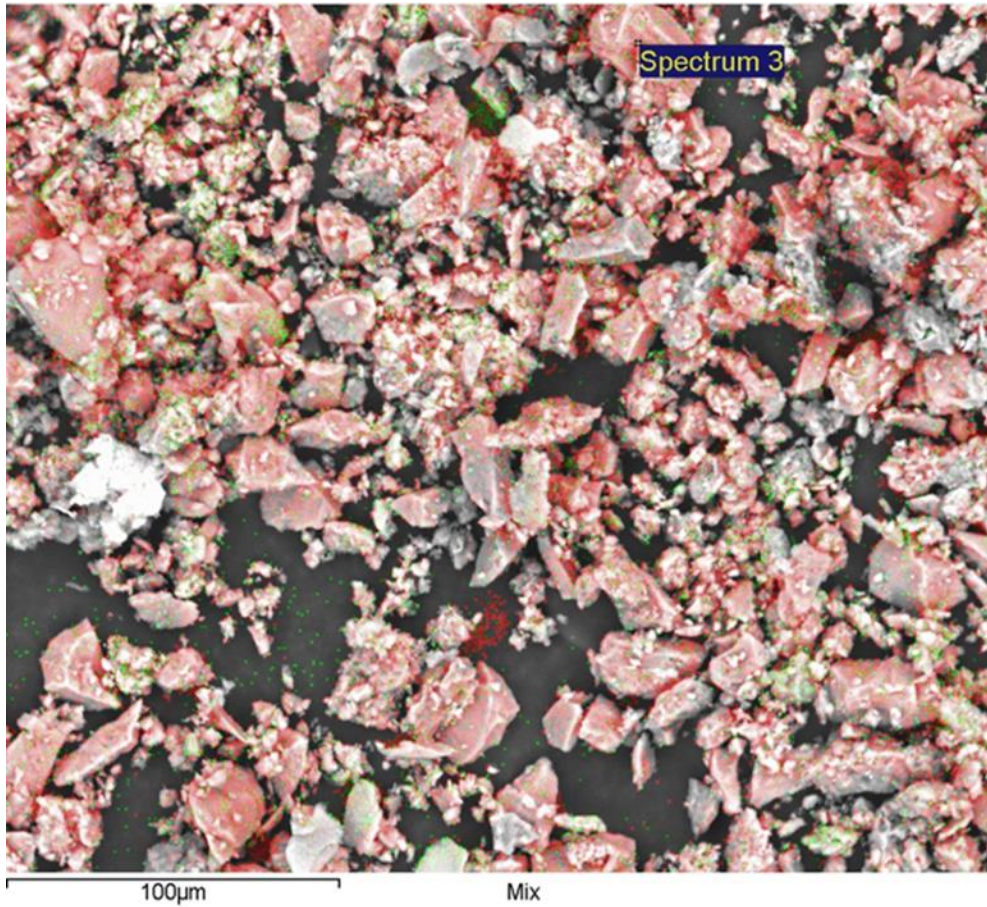


Figure 19. Photomicrograph of WF#9 Ne Alden and associated spectra point. The color red highlights the presence of silica; the color green highlights the presence of aluminum.

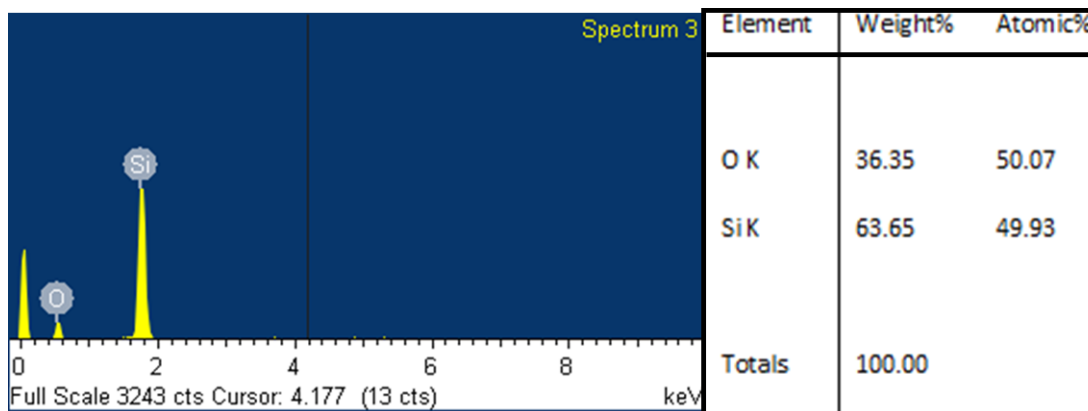


Figure 20. EDS spectra for WF#9 Ne Alden.

3.4 Size Distribution

Grain size estimations of the ten Woodford samples were measured from the SEM photomicrographs at 4000x magnification. The grain sizes were measured in microns (μm), converted to Krumbein's phi scale, and cumulative percent of the total point count were calculated. The results of the grain size data and cumulative percent are presented below (Table 6). The data obtained through the point counting was used to graphically present the data in cumulative curve plots. A cumulative curve plot for WF#1 McCalla Ranch is presented below (Figure 21). The remaining plots can be found in Appendix A.

WF#1 McCalla Ranch			WF#2 Sara Kirk			WF#3 Lela Rahm			WF#4 Guthrie			WF#5 Dwyer Mt			WF#6 Cement Ord			WF#7 Chenoweth			WF#8 Curtis			WF#9 Ne Alden			WF#10 Hannah		
Phi	Cum %		Phi	Cum %		Phi	Cum %		Phi	Cum %		Phi	Cum %		Phi	Cum %		Phi	Cum %		Phi	Cum %		Phi	Cum %		Phi	Cum %	
11.0	100.00		10.0	100.00		10.0	100.00		10.0	100.00		10.0	100.00		10.0	100.00		10.0	100.00		10.0	100.00		10.0	100.00		10.0	100.00	
10.0	74.18	9.0	56.36	9.0	74.32	9.0	53.13	9.0	40.28	9.0	68.22	9.0	40.38	9.0	55.86	9.0	55.17	9.0	55.17	9.0	55.17	9.0	55.17	9.0	55.17	9.0	55.17	9.0	55.43
9.0	48.77	8.4	35.45	8.4	37.16	8.4	20.09	8.4	20.14	8.4	35.66	8.4	16.48	8.4	23.45	8.4	27.59	8.4	27.59	8.4	27.59	8.4	27.59	8.4	27.59	8.4	27.59	8.4	28.57
8.4	24.18	8.0	20.00	8.0	22.97	8.0	6.70	8.0	9.03	8.0	24.03	8.0	7.97	8.0	15.86	8.0	18.10	8.0	18.10	8.0	18.10	8.0	18.10	8.0	18.10	8.0	18.10	8.0	16.00
8.0	14.75	7.6	13.64	7.6	14.86	7.6	4.46	7.6	6.94	7.6	16.28	7.6	5.22	7.6	11.03	7.6	10.34	7.6	10.34	7.6	10.34	7.6	10.34	7.6	10.34	7.6	10.34	7.6	10.86
7.6	9.84	7.4	8.18	7.4	11.49	7.4	2.23	7.4	4.86	7.4	14.73	7.4	3.57	7.4	8.97	7.4	6.90	7.4	6.90	7.4	6.90	7.4	6.90	7.4	6.90	7.4	6.90	7.4	8.57
7.4	6.56	7.0	7.27	7.2	8.78	7.2	1.79	7.2	4.17	7.2	13.18	7.2	3.02	7.2	6.90	7.2	6.03	7.2	6.03	7.2	6.03	7.2	6.03	7.2	6.03	7.2	6.03	7.2	6.29
7.2	4.10	6.5	5.45	7.0	6.76	6.6	1.34	6.6	3.47	7.0	11.63	6.8	1.92	7.0	5.52	7.0	5.17	7.0	5.17	7.0	5.17	7.0	5.17	7.0	5.17	7.0	5.17	7.0	5.71
6.8	2.05	6.3	4.55	6.6	4.05	6.0	0.45	6.0	2.78	6.6	9.30	6.6	1.37	6.8	4.83	6.6	4.31	6.6	4.31	6.6	4.31	6.6	4.31	6.6	4.31	6.6	4.31	6.6	5.14
6.6	1.64	5.9	3.64	6.5	3.38	6.5	3.38	6.5	2.08	6.4	7.75	6.5	0.82	6.5	3.45	6.4	3.45	6.4	3.45	6.4	3.45	6.4	3.45	6.4	3.45	6.4	3.45	6.4	4.00
6.3	1.23	5.7	2.73	6.2	2.70	6.2	2.70	6.2	1.39	6.3	6.20	6.3	0.55	6.4	2.76	6.1	2.59	6.1	2.59	6.1	2.59	6.1	2.59	6.1	2.59	6.1	2.59	6.1	3.43
6.1	0.82	5.6	1.82	5.9	2.03	5.9	2.03	5.9	0.69	6.2	5.43	6.2	0.27	6.1	2.07	5.4	1.72	5.4	1.72	5.4	1.72	5.4	1.72	5.4	1.72	5.4	1.72	5.4	2.86
5.4	0.41			5.6	1.35	5.6	1.35	5.6		6.1	2.33	6.1		5.7	1.38	5.1	0.86	5.1	0.86	5.1	0.86	5.1	0.86	5.1	0.86	5.1	0.86	5.1	2.29
				5.4	0.68	5.4		5.4		5.6	1.55	5.6		5.4	0.69														

Table 6. Table depicting grains sizes (phi) and cumulative percents for the ten Woodford samples.

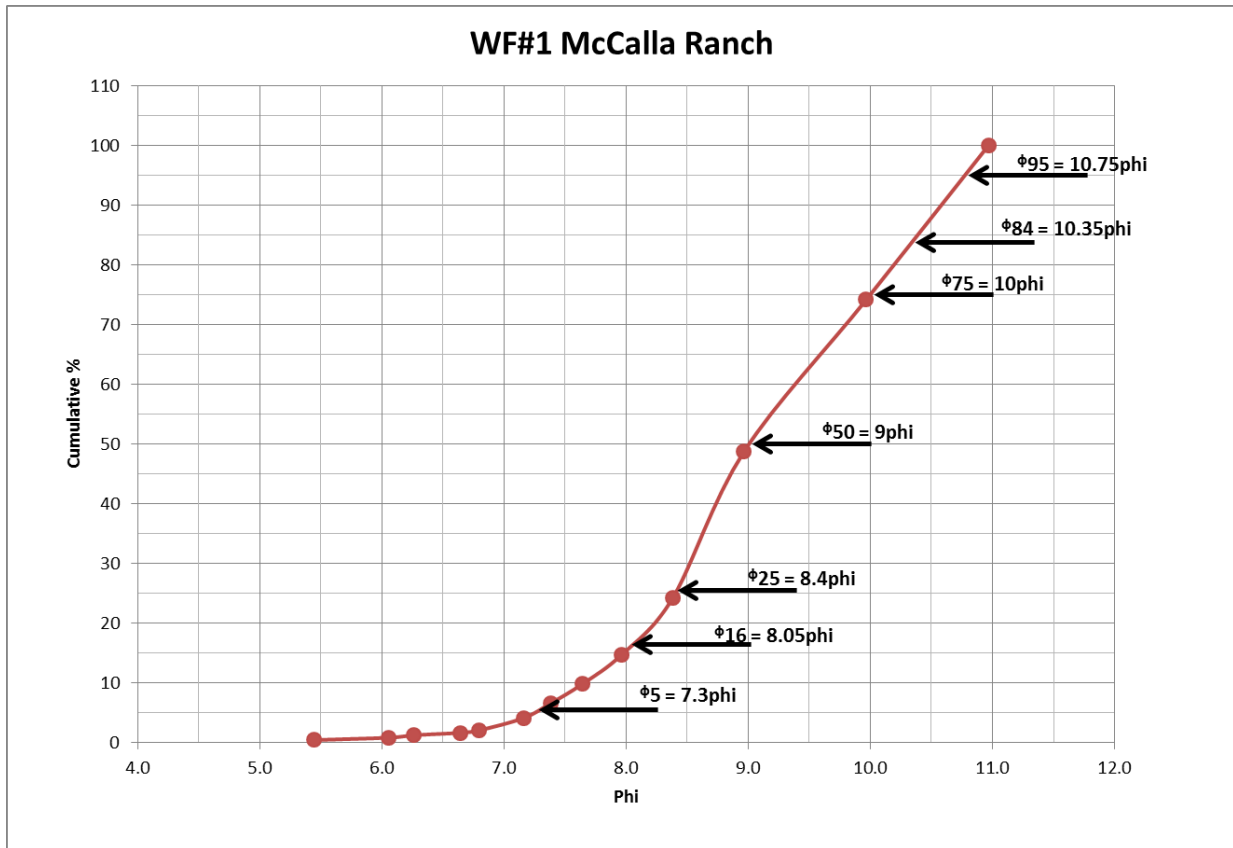


Figure 21. Cumulative curve plot for WF#1 McCalla Ranch and associated ϕ locations and values.

The cumulative curve plots were used to calculate ϕ_5 , ϕ_{16} , ϕ_{25} , ϕ_{50} , ϕ_{75} , ϕ_{84} , and ϕ_{95} for each well. These phi values were used to calculate the mode, median, graphic mean, inclusive graphic standard deviation, inclusive graphic skewness, and kurtosis for each well after Folk, 1981. These data are presented in Table 7.

	WF1	WF2	WF3	WF4	WF5	WF6	WF7	WF8	WF9	WF10
φ5	7.3	6.4	6.8	7.85	7.4	6.15	7.6	6.85	6.87	6.75
φ16	8.05	7.8	7.7	8.3	8.25	7.63	8.35	7.79	7.87	7.97
φ25	8.4	8.1	8.05	8.5	8.55	8	8.63	8.43	8.3	8.27
φ50	9	8.8	8.57	8.9	9.15	8.63	9.15	8.85	8.85	8.85
φ75	10	9.4	9	9.45	9.55	9.15	9.55	9.4	9.4	9.4
φ84	10.35	9.6	9.27	9.62	9.7	9.42	9.7	9.6	9.6	9.6
φ95	10.75	9.85	9.7	9.87	9.87	9.8	9.87	9.85	9.86	9.86
Mode	10	10	9	10	10	9	10	10	10	10
Median	10	9.4	9	9.4	10	9	10	9.4	9.4	9.4
Graphic Mean	9.18	8.73	8.51	8.94	9.03	8.56	9.07	8.81	8.77	8.81
Skewness	0.094202899	-0.25121	-0.16448	0.025653	-0.32919	-0.23811	-0.27541	-0.2523	-0.22868	-0.21512
Kurtosis	0.883709016	1.087642	1.251079	0.871441	1.012295	1.300784	1.011226	1.267534	1.114009	1.127956

Table 7. Table depicting the data calculated from the cumulative curves for each sample.

Chapter 4 - Discussion

4.1 – XRF Precision

The handheld XRF is a relatively new, emerging instrument for quick analysis in the field. In this study the XRF data were used to analyze ratios between element weight percent, and determine if it could be an effective tool to use for on-site analysis on drilling rigs. Handheld XRF has difficulty detecting lighter elements, such as aluminum and silicon, and there was initial concern that without the use of helium in a controlled atmosphere our readings could be inaccurate. These concerns are due to the fact that secondary radiation from lighter elements contains low energy and have lower penetrating powers, and these are further diminished if the x-ray beam is to pass through air. Due to the portable nature of the handheld XRF, the use of helium in a controlled atmosphere during analysis will not commonly be available for readings taken in the field. Another area of concern was using the generic mudrock calibration provided by Bruker for analysis. Mudrocks make up over 50% of the earth’s sedimentary deposits and can have variations in composition. For example, the composition of the Woodford shale differs from that of a typical mudrock as it is organic rich and contains high amounts of silica.

A precision test was conducted on the Woodford #2 Sara Kirk sample. The results obtained yielded reasonably precise readings for all elements, with the highest variation being less than 3 percent (Table 8). The precision of the handheld XRF in this study eliminates any previous concerns about the use of a helium purge and the Bruker mudrock calibration. The handheld XRF can provide precise readings in the field without the requirement of a helium purge. The Bruker mudrock calibration will provide precise readings for the organic rich Woodford shale.

Woodford #2 Sara Kirk Precision																				
Major	NaKa1	MgKa1	AlKa1	SiKa1	P Ka1	S Ka1	K Ka1	CaKa1	BaLa1	TiKa1	V Ka1	CrKa1	MnKa1	FeKa1	CoKa1	NiKa1	CuKa1	ZnKa1		
MAJ precision 1.1	0.63592	0.45571	3.93451	14.2873	0.03699	3.96889	1.72404	2.02167	-0.0415	0.26772	0.02978	0.0197	0.02159	3.84935	0.00152	0.0059	0.00761	0.0138		
MAJ precision 1.2	0.63408	0.44584	3.91187	14.2786	0.03995	3.97729	1.71356	2.00289	-0.0409	0.26681	0.02876	0.01956	0.02181	3.77526	0.00151	0.00577	0.0074	0.01332		
MAJ precision 1.3	0.63392	0.44855	3.98887	14.3207	0.03882	3.99065	1.72112	2.01726	-0.0477	0.2671	0.03056	0.01965	0.02146	3.86745	0.00153	0.00597	0.00706	0.01304		
MAJ precision 1.4	0.6344	0.45952	3.88535	14.3041	0.03472	3.99719	1.72803	2.01835	-0.0464	0.27149	0.03032	0.01932	0.02154	3.8313	0.00152	0.00592	0.00706	0.01414		
MAJ precision 1.5	0.63371	0.44373	3.86342	14.1674	0.03109	3.99587	1.71912	2.00231	-0.0539	0.26858	0.03084	0.01992	0.02126	3.83969	0.00152	0.00592	0.00681	0.01261		
stdev	0.00088	0.0067	0.0484	0.06045	0.00353	0.01238	0.00542	0.00918	0.00529	0.00189	0.00082	0.00022	0.0002	0.03477	5.1E-06	7.5E-05	0.00032	0.0006		
precision	0.00039	0.003	0.02164	0.02703	0.00158	0.00554	0.00242	0.00411	0.00237	0.00084	0.00037	9.7E-05	8.8E-05	0.01555	2.3E-06	3.4E-05	0.00014	0.00027		
percent	0.03942	0.29972	2.16442	2.70348	0.15775	0.5536	0.24231	0.41054	0.23671	0.0843	0.03659	0.00972	0.00884	1.55475	0.00023	0.00337	0.01414	0.02699		
Trace	BaLa1	CrKa1	MnKa1	CoKa1	NiKa1	CuKa1	ZnKa1	AsKa1	PbLa1	ThLa1	RbKa1	ULa1	SrKa1	Y Ka1	ZrKa1	NbKa1	MoKa1	SnKa1	SbKa1	
TR precision 1.1 4	-0.0108	0.02373	0.01971	0.00116	0.0092	0.00039	0.01023	0.00151	0.00173	0.00068	0.01153	-3E-06	0.0049	0.00229	0.0049	0.00034	0.00452	0.00041	0.0025	
TR precision 1.2 4	-0.0679	0.02332	0.01943	0.00112	0.00846	0.00049	0.01048	0.00126	0.0016	0.00065	0.01189	0.00039	0.00465	0.00232	0.00441	0.00031	0.00467	0.00042	0.0026	
TR precision 1.3 4	-0.0529	0.02402	0.01965	0.0013	0.00867	0.00048	0.01018	0.00144	0.0018	0.00069	0.01199	-0.0005	0.00489	0.00254	0.00485	0.00027	0.00444	0.00041	0.00237	
TR precision 1.4 4	-0.161	0.02211	0.01848	0.0013	0.00882	0.00015	0.01068	0.00155	0.00177	0.00066	0.01153	0.00016	0.00484	0.00226	0.00493	0.00031	0.00452	0.0004	0.00251	
TR precision 1.5 4	-0.084	0.02179	0.01882	0.00124	0.00908	0.00037	0.01022	0.00125	0.00169	0.00068	0.01164	-0.0003	0.00494	0.00234	0.00477	0.00028	0.0045	0.0004	0.00261	
stdev	0.05508	0.00099	0.00054	8E-05	0.0003	0.00014	0.00021	0.00014	7.9E-05	1.7E-05	0.00021	0.00034	0.00011	0.00011	0.00021	2.6E-05	8.3E-05	6.2E-06	9.7E-05	
precision	0.02463	0.00044	0.00024	3.6E-05	0.00013	6.2E-05	9.6E-05	6.2E-05	3.5E-05	7.4E-06	9.6E-05	0.00015	5.1E-05	5.1E-05	9.5E-05	1.2E-05	3.7E-05	2.8E-06	4.3E-05	
percent	2.46314	0.04442	0.02424	0.00357	0.01346	0.00616	0.00961	0.00621	0.00353	0.00074	0.00956	0.01504	0.00513	0.00505	0.00948	0.00117	0.00373	0.00028	0.00432	

Table 8. Table displaying the elemental precision of the handheld XRF.

4.2 – XRF: Estimate of Shale Mineralogy

Due to the abundance of elements and other data to be observed within the study, it was determined that the fastest and best method to depict and analyze correlations would be through the generation of a correlation matrix. For the estimates of shale mineralogy through use of handheld XRF, the major and trace element data along with TOC, organic matter, vitrinite reflectance, rare earth elements, chert percent, mean size, Si/K, and Si/Al ratios were examined within the matrix.

This matrix allows recognition of related variables, whether the correlations are negative or positive, and how strong or weak those correlations are. In addition, those variables that are

statistically valid were used to obtain coefficient of determination values (r^2) to assess how much the variation in one variable is directly attributable to the variation in the other. To determine that the correlation is not a chance occurrence, but instead generalized of the total population, the degree of freedom was calculated, and corresponding minimum r values were identified. The degree of freedom for this study was 8 (n=10), and the minimum value obtained for a 0.05 probability was 0.632. Values within the correlation matrix that had an absolute value of 0.632 or higher are highlighted.

In light of expected mineralogy, the correlations observed are reasonable. Totten et al., (2013), conducted a study on the illitization of the Woodford shale in hopes of finding the source of potassium needed for this transformation. They note that the Woodford shale is known to have organic matter values ranging 3-24%. Previous work by Chaudhuri et al., (2007, 2012) has suggested that potassium and aluminum concentrations are sourced from the organic matter and being added to the system during the illitization process. The Woodford shale is also known for its characteristically high amounts of silica that allows for easy generation of fractures, which makes it a strong unconventional target. Previous research conducted by Ramirez (2013) and Coddington (2013) on the samples pertaining to this study have also shed light on heavy minerals and their compositions, as well as in depth analysis of the organic fraction. The associations of variables that show a correlation are highlighted within the matrix and discussed below (Table 9).

	Na	Mg	Al	Si	P	S	K	Ca	Ba	Ti	Mn	Fe	Zn	Rb	Sr	Zr	TOC	Ro	REE	OM%	Chert %	GRAPHIC MEAN	Si/Al	Si/K
Na	1																							
Mg	0.13742	1																						
Al	0.23364	0.71684	1																					
Si	-0.83672	-0.24001	-0.06531	1																				
P	0.4173	-0.48039	-0.45848	-0.48929	1																			
S	-0.69305	-0.2192	-0.20133	0.52205	0.01807	1																		
K	0.40716	0.71223	0.946	-0.17304	-0.31224	-0.36696	1																	
Ca	0.74226	0.48177	0.10928	-0.86816	0.23609	-0.56295	0.27164	1																
Ba	-0.54609	-0.1594	-0.20978	0.38943	-0.12705	0.83069	-0.36382	-0.30608	1															
Ti	0.61628	0.56945	0.82029	-0.43769	-0.14787	-0.57936	0.88705	0.37597	-0.60303	1														
Mn	0.34337	0.70153	0.11613	-0.5276	-0.15086	-0.40467	0.20733	0.82359	-0.16938	0.1625	1													
Fe	0.47172	0.53449	0.68823	-0.39978	0.15502	-0.29746	0.81497	0.3847	-0.36128	0.80921	0.12929	1												
Zn	-0.63967	-0.29179	-0.31248	0.47561	-0.07734	0.89394	-0.48576	-0.45014	0.97816	-0.69897	-0.29678	-0.46922	1											
Rb	0.63027	0.51727	0.86312	-0.37269	-0.12334	-0.46752	0.90789	0.29907	-0.51331	0.955	0.09342	0.74561	-0.60111	1										
Sr	0.20488	0.57483	0.41556	-0.3427	-0.21076	-0.05741	0.31345	0.34515	-0.19226	0.31041	0.47475	0.06132	-0.21387	0.39401	1									
Zr	0.40952	0.61737	0.9064	-0.18548	-0.46722	-0.38342	0.88828	0.19441	-0.38744	0.89401	0.12912	0.57875	-0.48035	0.92172	0.48794	1								
TOC	-0.48874	-0.24113	-0.10095	0.31481	0.18949	0.62431	-0.27473	-0.54453	0.19375	-0.33146	-0.46116	-0.22021	0.33988	-0.22204	0.31485	-0.22419	1							
Ro	0.2044	-0.03163	0.1946	-0.08674	-0.10265	0.0344	0.22734	0.20024	0.37511	0.1547	-0.08639	0.23387	0.24415	0.1589	-0.22141	0.22153	-0.37531	1						
REE	-0.50422	-0.17992	-0.04281	0.45378	-0.11901	0.89122	-0.19246	-0.48574	0.84911	-0.35838	-0.42479	-0.19617	0.86137	-0.24828	-0.11831	-0.12379	0.3225	0.31921	1					
OM%	0.56918	0.6864	0.61745	-0.6714	0.13785	-0.1629	0.65537	0.69639	-0.04992	0.60826	0.52189	0.73227	-0.20085	0.62362	0.46675	0.50442	-0.19099	0.27504	-0.07972	1				
Chert %	-0.53624	-0.77374	-0.63869	0.59731	0.08455	0.25457	-0.71226	-0.71126	0.1472	-0.71237	-0.57266	-0.73651	0.31186	-0.66934	-0.46215	-0.65371	0.37637	-0.36091	0.05607	-0.88134	1			
GRAPHIC MEAN	0.49378	-0.38515	-0.00388	-0.05028	0.15352	-0.47987	0.08106	-0.0769	-0.4935	0.19746	-0.23447	-0.14775	-0.44469	0.33428	-0.05494	0.20316	-0.18477	-0.14934	-0.36025	-0.26022	0.29342	1		
Si/Al	-0.65264	-0.6332	-0.78514	0.5198	-0.00923	0.2708	-0.82046	-0.51711	0.19624	-0.75959	-0.36155	-0.70696	0.32883	-0.85253	-0.47154	-0.73077	0.24114	-0.19509	0.10262	-0.88267	0.78386	-0.13802	1	
Si/K	-0.69705	-0.57637	-0.73193	0.52372	-0.10734	0.29886	-0.80835	-0.52051	0.25869	-0.75064	-0.34053	-0.72831	0.38242	-0.84995	-0.41583	-0.68604	0.25179	-0.15148	0.14317	-0.85089	0.75258	-0.21301	0.98741	1

Table 9. Correlation matrix of major and trace element data analyzed.

4.2.1 – Clay Mineralogy and Chert

The Woodford shale is known to have a clay mineralogy composition predominantly of illite (Lewan, 1987). Substitution is common in both the tetrahedral and octahedral sheets; predominantly aluminum replacing silica in the tetrahedral and magnesium or iron replacing aluminum within the octahedral sheet. The strong interlayer bond between illite is composed of potassium ions. A strong K/Al correlation depicted within the matrix proves this assumption as aluminum is representative of the clay mineral fraction (aluminosilicates), and potassium representative of the specific clay mineral illite (K-rich aluminosilicate). Positive correlations noted between Al/Mg and K/Mg provides further evidence to support this claim. An inverse correlation is also observed between aluminum and chert weight percent, while no correlation is observed between aluminum and organic matter weight percent. This is also consistent with the assumption of aluminum being located within the clay mineral fraction of the samples, as organic- rich shales are comprised of clay minerals, chert, and organic matter.

The silica/potassium and silica/ aluminum ratio in each sample were used as a preliminary estimation of chert present in samples. Silica was chosen to be representative of chert in these ratios because chert is composed of silicon dioxide (SiO_2). Also, as previously stated, the Woodford Shale clay mineral fraction is illite in composition which is the reasoning for the selection of potassium and aluminum to represent the clay fraction. Hence these ratios should mimic the ratios of the corresponding minerals. The ratios show a strong correlation to one another within the matrix, and are graphically presented below (Figure 22).

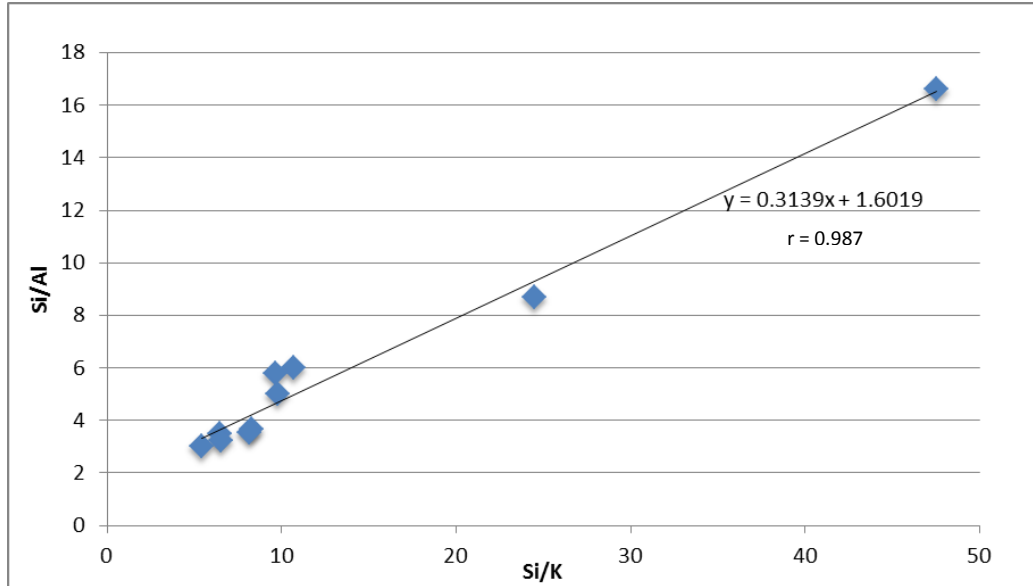


Figure 22. Graph depicting the strong correlation observed between Si/Al and Si/K ratios.

A correlation was also observed between the Si/Al and Si/K ratios and the weight percent chert as calculated through the sodium bisulfate fusion. This comparison was expected, as chert is a main contributor of silica in the Woodford shale, so our whole rock silica amounts and fused chert amounts should be similar in weight percent (Figure 23). The total chert weight percentages could show slight inaccuracy, as the multi-step approach administered left probability for loss of sample. Also, although chert is composed of silicon dioxide, shale is known to contain silica within the clay and organic fractions. Therefore the silica readings obtained through XRF are expected to be higher than the estimated chert percentages, which could lead to weakening of the correlation to chert.

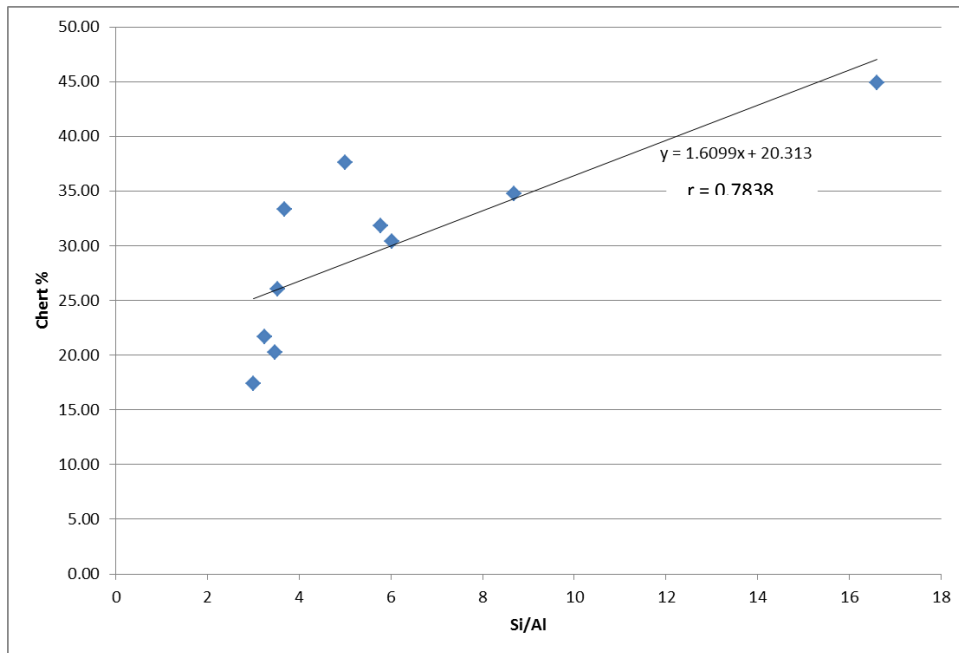


Figure 23. Graph depicting the correlation between the chert percent and the observed XRF Si/Al ratio.

4.2.2 – Heavy Minerals

Previous work pertaining to the heavy minerals present within the Woodford shale samples used for this study was conducted by Coddington (2013). The correlation matrix displays a positive correlation between titanium, iron, rubidium, and zirconium all of which could be related to the heavy minerals observed within these Woodford samples. The strongest correlation is observed with the iron which is logical; as Coddington’s research depicted that the heavy mineral fraction of the Woodford is predominantly pyrite and iron micas.

An inverse correlation was noted between these elements pertaining to heavy minerals, and the chert amount within in samples (Figures 24-27). These correlations are not unexpected given that cherts, as well as heavy minerals, contribute to the non-clay fraction of the Woodford.

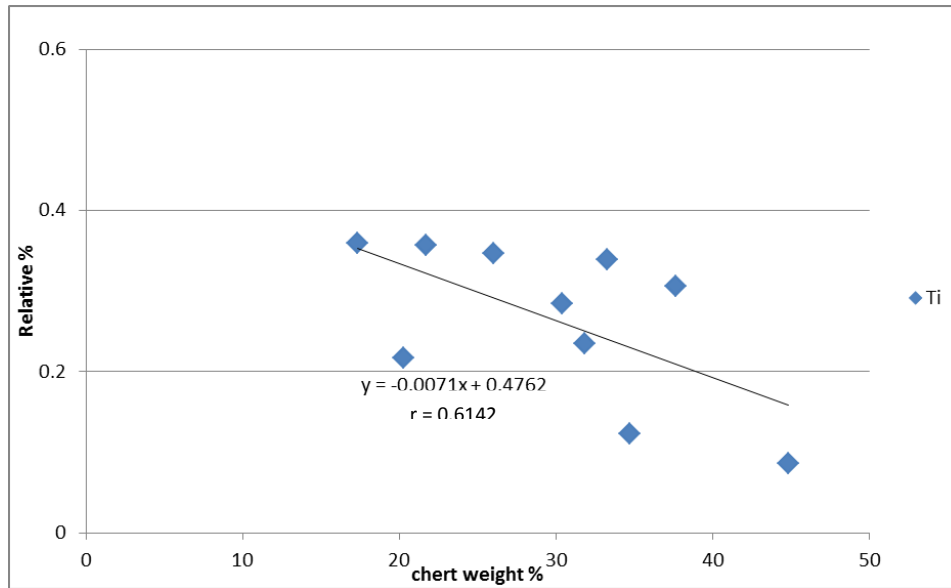


Figure 24. Graph depicting the inverse correlation between titanium and chert weight percent.

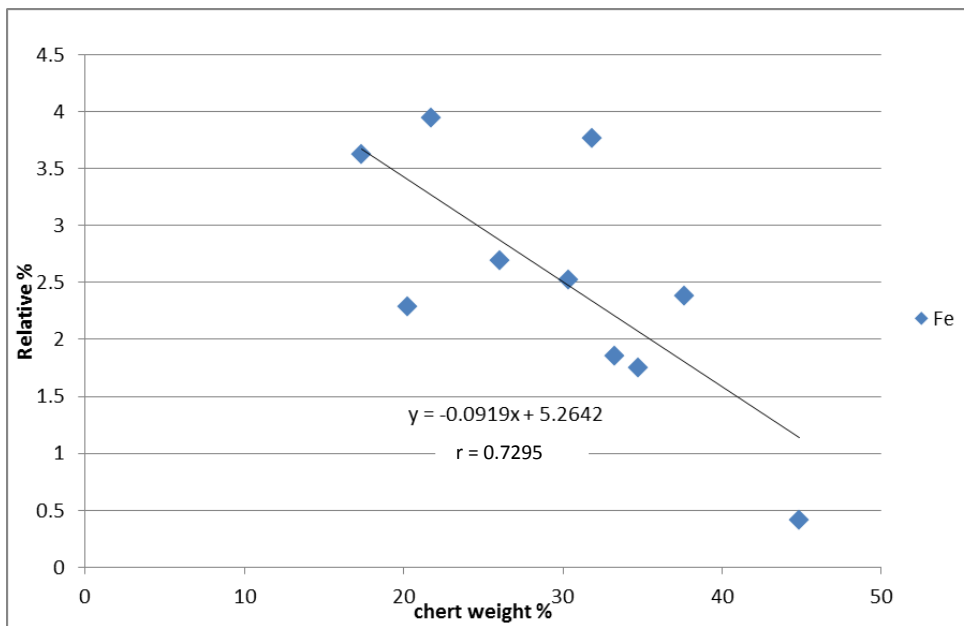


Figure 25. Graph depicting the inverse correlation between iron and chert weight percent.

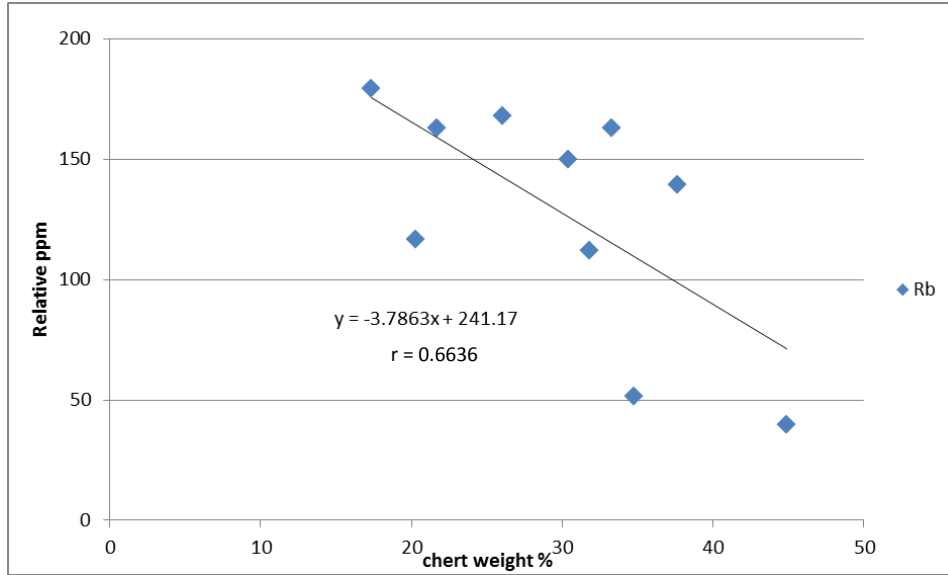


Figure 26. Graph depicting the inverse correlation between rubidium and chert weight percent.

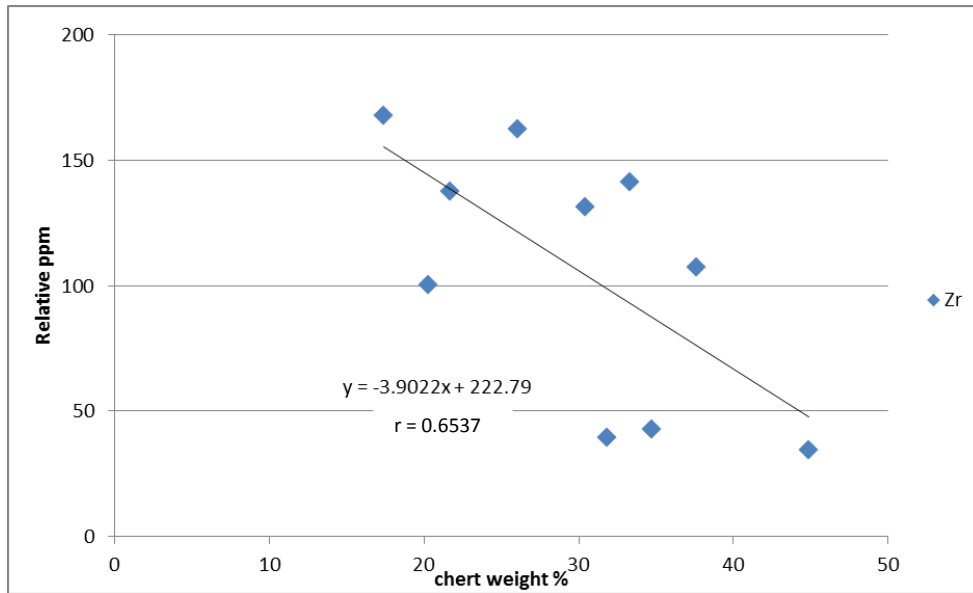


Figure 27. Graph depicting the inverse correlation between zirconium and chert weight percent.

4.2.3 – Rare Earth Elements

The elements barium, sulfur, and zinc all display positive correlations relative to one another. It is hypothesized that the relation of barium to sulfur could be indicative of barite, which has a chemical formula of BaSO_4 . This is supported by research conducted on other North American Devonian black shales that have revealed the presence of barite (Lash and Blood, 2012). The source of barite within most shales and sandstones is located within detrital feldspar and mica (Ham & Merritt, 1944).

The relation of zinc to sulfur is hypothesized to be indicative of sphalerite, which has a chemical formula of $(\text{Zn,Fe})\text{S}$. Sphalerite deposits have been found within Lower Devonian deposits. These deposits are also noted to commonly be found in conjunction with barite (Meurant, 2012).

Positive correlations were observed between sulfur, zinc, and barium in relation to rare earth element composition (Figures 28-30). This correlation is logical as rare earth elements are known to be present in both barites and sphalerites (Attendorn and Bowen, 1997).

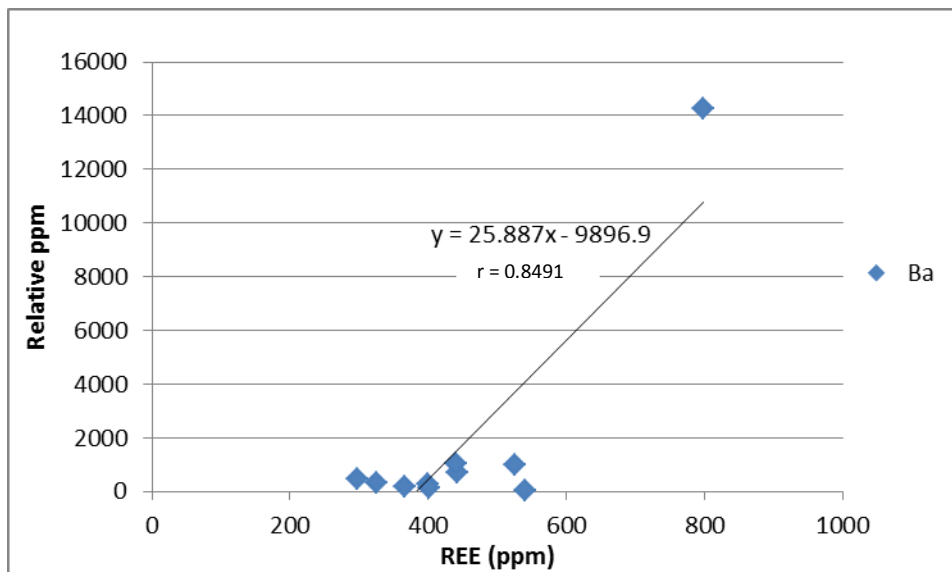


Figure 28. Graph depicting strong relationship of barium to rare earth element concentrations in the organic matter fraction of the samples.

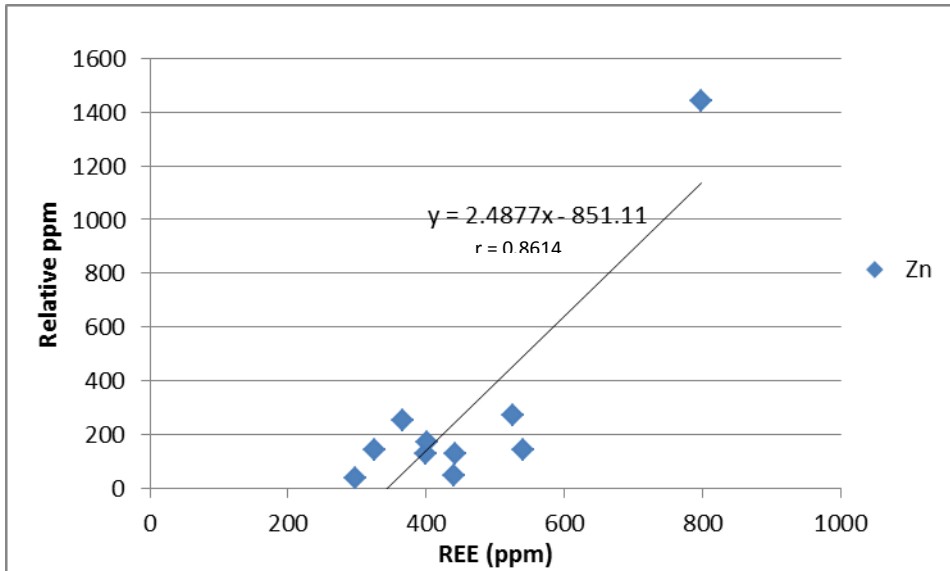


Figure 29. Graph depicting strong relationship of zinc to rare earth element concentrations in the organic matter fraction of the samples.

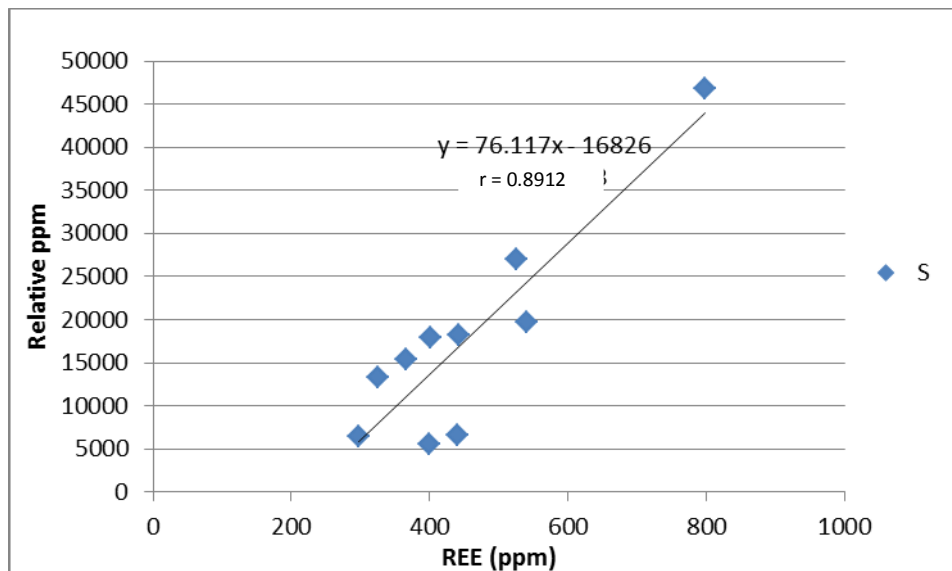


Figure 30. Graph depicting strong relationship of sulfur to rare earth element concentrations in the organic matter fraction of the samples.

4.3 – XRF: A Proxy for Organic Matter

Organic matter values are important in the petroleum industry as they are used to assess the quality of source rocks and productivity of unconventional reservoirs. Samples with higher amounts of organic matter present the highest potential for petroleum accumulations. A strong

inverse correlation is observed between organic matter weight present and the Si/Al and Si/K ratios. This is reasonable, because the higher the organic content of shale, the less chert and clay minerals it can contain, as they are the other major constituents of organic-rich shales.

Strong correlations between magnesium, potassium, calcium, and iron to the organic matter weight percent were also noted. These correlations are logical, as these elements were all observed within the organic matter fraction of the samples. The major element analysis of the organic portion of the samples was conducted through Ion Coupled Plasma Atomic Emission Spectrometer (ICP-AES) by Ramirez (2013), and is presented in Table 10.

It should be noted that when graphically presented, the samples from this study have a gap between 5 and 15% organic matter, and that these data should be determined by additional study (Figure 31). The reliability of the equation above 15% is useful for many unconventional reservoirs. The ability to use handheld XRF for quick on site analysis to estimate organic matter will save contractors time and money, and has the potential to greatly impact in the petroleum industry. The strong inverse correlation observed shows that the handheld XRF has the potential to provide quick data on Si/Al ratios that can be used as a proxy for organic matter estimates.

Woodford Shale (WF) Samples Organic Matter Analysis (weight %)										
Sample	Si %	Al %	Mg %	Ca %	Fe %	Mn %	Ti %	Na %	K %	P %
WF#1	<0,03	20.17	6.73	8.83	3.77	0.03	0.40	0.86	5.69	0.059
WF#2	<0,04	13.65	9.16	12.94	3.18	0.11	0.52	0.53	5.96	0.47
WF#3	0.047	18.97	6.72	5.27	11.01	0.047	0.61	0.88	7.56	0.093
WF#4	0.33	21.54	5.34	4.91	8.95	0.04	0.47	1.54	6.09	0.060
WF#5	0.16	11.09	2.89	1.70	5.34	0.023	0.56	0.65	5.37	0.069
WF#6	0.75	12.56	3.23	0.44	7.83	0.017	0.76	0.92	5.74	0.11
WF#7	0.096	23.85	6.74	0.37	4.86	0.055	0.48	0.84	10.14	<0,06
WF#8	0.87	17.54	4.74	2.52	5.71	0.035	0.92	1.35	5.76	0.17
WF#9	0.061	6.32	0.31	5.77	3.15	0.017	0.45	0.15	1.40	2.59
WF#10	0.044	16.82	8.23	9.89	3.80	0.037	0.18	0.42	7.48	0.052

Table 10. Major element analytical results of the organic portion of the Woodford samples from Ramirez (2013).

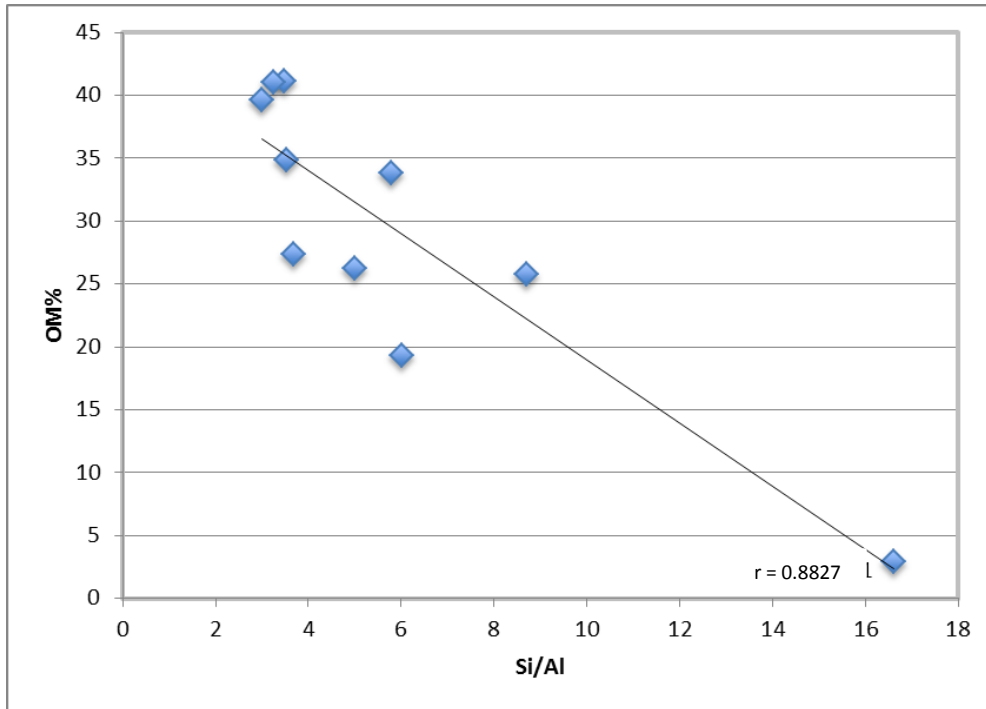


Figure 31. Graph depicting the inverse correlation between organic matter weight percent and handheld XRF Si/Al ratio.

4.4 – Grain Size Correlations

Due to the large amount of grain size data collected within this study a correlation matrix was once again generated for analysis of relations between variables (Table 11). The degree of freedom for these analysis remained the same as before, and was 8 (n=10). Therefore the minimum value obtained for a 0.05 probability was again 0.632. Values within the correlation matrix that had an absolute value of 0.632 or higher are highlighted. The associations of variables that show a correlation are discussed below.

	TOC	Ro	REE	OM%	% Chert	Si/Al	Si	K/Rb	MODE	MEDIAN	GRAPHIC MEAN	GRAPHIC SD	Inclusive SD	Skewness	Kurtosis	φ 5	φ 16	φ 25	φ 50	φ 75	φ 84	φ 95	
TOC	1																						
Ro	-0.375	1																					
REE	0.323	0.319	1																				
OM%	-0.191	0.275	-0.08	1																			
% Chert	0.376	-0.361	0.056	-0.881	1																		
Si/Al	0.241	-0.195	0.103	-0.883	0.784	1																	
Si	0.315	-0.087	0.454	-0.671	0.597	0.52	1																
K/Rb	-0.11	0.293	0.39	0.256	-0.239	-0.174	0.43	1															
MODE	-0.197	-0.177	-0.475	-0.433	0.481	0.31	0.028	-0.242	1														
MEDIAN	-0.232	-0.206	-0.386	-0.303	0.288	-0.13	0.14	-0.317	0.563	1													
GRAPHIC MEAN	-0.185	-0.149	-0.36	-0.26	0.293	-0.138	-0.05	-0.538	0.522	0.94625	1												
GRAPHIC SD	-0.303	0.097	-5E-04	-0.041	0.059	-0.006	-0.155	-0.124	0.431	0.06113	0.0917	1											
Inclusive SD	-0.248	0.268	0.219	0.089	-0.122	0.002	-0.056	0.239	0.26	-0.271	-0.303	0.8818	1										
Skewness	-0.185	-0.026	-0.136	0.128	0.038	-0.156	-0.575	-0.643	4E-06	0.08231	0.3404	0.4267	0.0837	1									
Kurtosis	0.372	0.182	0.544	0.144	-0.244	0.077	0.349	0.601	-0.469	-0.7127	-0.835	-0.024	0.382	-0.5789	1								
φ 5	0.05	-0.315	-0.365	-0.184	0.272	-0.088	-0.091	-0.59	0.055	0.65985	0.7633	-0.399	-0.779	0.3911	-0.792	1							
φ 16	-0.154	-0.131	-0.348	-0.207	0.236	-0.092	-0.016	-0.404	0.228	0.77925	0.8282	-0.432	-0.739	0.1819	-0.824	0.914	1						
φ 25	0.168	-0.253	-0.279	-0.31	0.314	-0.042	0.106	-0.524	0.25	0.81259	0.8527	-0.372	-0.681	0.0752	-0.645	0.873	0.89	1					
φ 50	-0.109	-0.177	-0.355	-0.349	0.328	-0.045	0.179	-0.327	0.522	0.95706	0.9175	-0.179	-0.465	-0.039	-0.695	0.722	0.87	0.907	1				
φ 75	-0.275	-0.094	-0.36	-0.241	0.271	-0.111	-0.158	-0.57	0.664	0.85699	0.9287	0.4398	0.0496	0.459	-0.771	0.528	0.585	0.632	0.758	1			
φ 84	-0.303	-0.061	-0.285	-0.199	0.246	-0.131	-0.18	-0.54	0.614	0.7615	0.8448	0.6042	0.2148	0.5623	-0.701	0.419	0.436	0.48	0.612	0.975	1		
φ 95	-0.318	-0.019	-0.174	-0.116	0.192	-0.153	-0.217	-0.478	0.474	0.56369	0.6662	0.7626	0.3938	0.6919	-0.573	0.268	0.217	0.243	0.36	0.859	0.951	1	

Table 11. Correlation matrix of the size data analyzed.

4.5 – Grain Size Parameters

The correlation matrix depicts many correlations pertaining to the grain size parameters of the samples. As depicted in Figure 22 of the results section, grain size parameters obtained in this study were $\phi 5$, $\phi 16$, $\phi 25$, $\phi 50$, $\phi 75$, $\phi 84$, and $\phi 95$ after Folk (1981), and correspond to the cumulative curve. For example, $\phi 95$ is located at 95% on the curve and is representative of the finest 5% of chert grains observed.

The first correlation is seen relating median to size. In fact, all phi values except $\phi 95$ show a correlation, with the strongest correlation (Figure 32) being observed in the $\phi 50$. This result is logical, and was expected because the $\phi 50$ indicates the mean grain size on the cumulative curve. It is also observed that the farther the phi values deviate from $\phi 50$, the weaker that correlation becomes. This trend in decreasing correlation is also logical, due to the fact that the median and mean are two measures of average grain size.

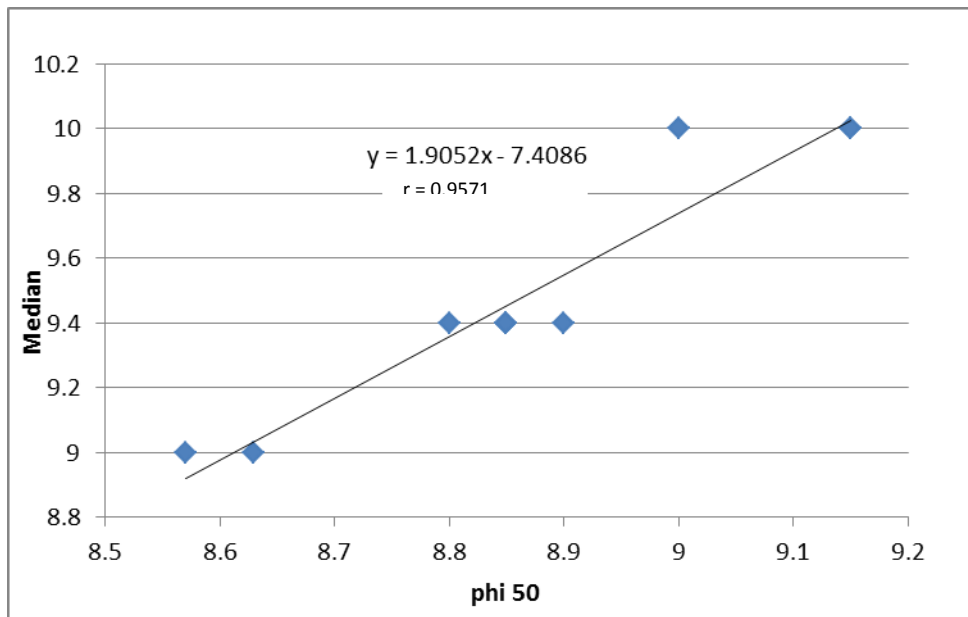


Figure 32. Graph depicting strong correlation between median and phi 50 (mean).

A strong positive correlation is also observed between size fraction and the mean. The correlation matrix depicts the strongest correlation for the ϕ_{75} grain size parameter. This result was expected and proves to be valid, as upon looking at the cumulative plots from which the grain size parameters were calculated, one can see that the ϕ_{75} on the curve is located at about a size of $\phi_{9.4}$ (Figure 33). Results from grain size analysis of the SEM photomicrographs depicted that the majority of the samples had a mean ranging between ϕ_9 and ϕ_{10} , with the exact mean being $\phi_{9.4}$. It is also noted that the larger size fractions have the weakest correlation, which is probably due to the fact that they had lower cumulative percent values.

The only correlation of grain size parameter to mode is shown in the ϕ_{75} parameter. This was expected due to the majority of observed grains in the samples being of the small size fraction. ϕ_{75} correlates to a grain size of about $\phi_{9.4}$ on the cumulative plots and the most abundant grain sizes identified in each of the samples varied between ϕ_9 and ϕ_{10} .

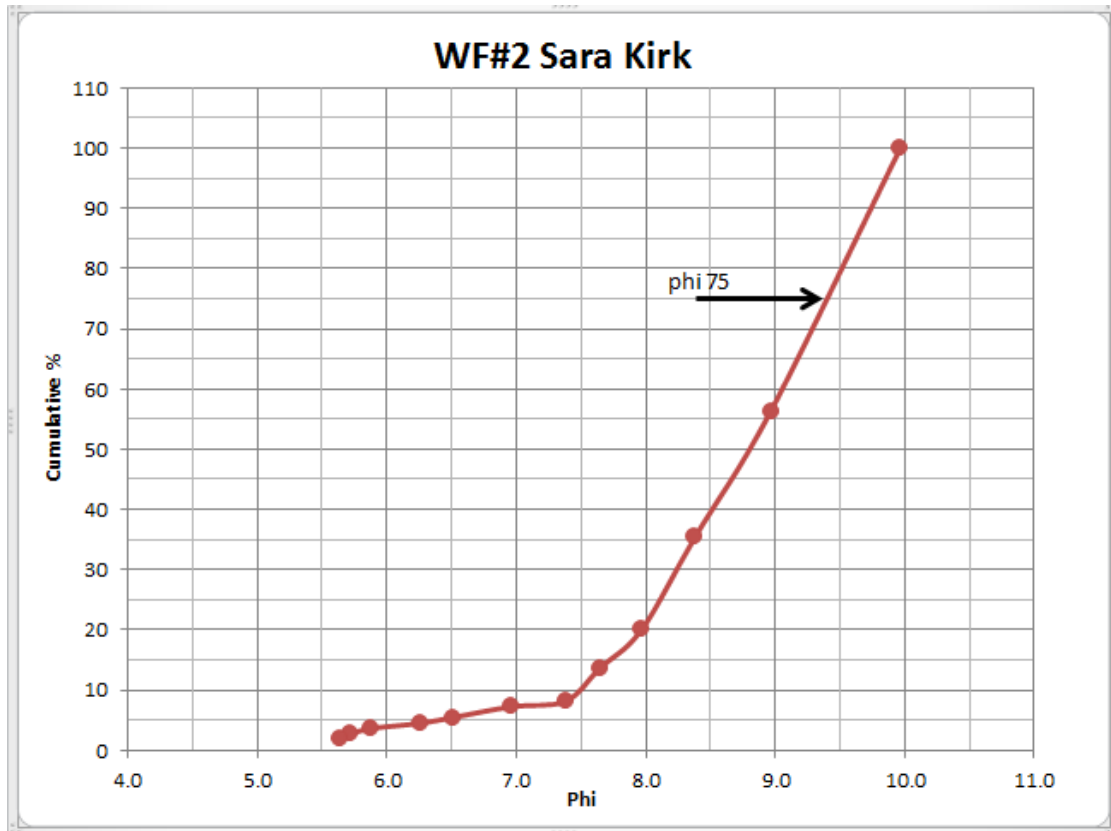


Figure 33. Graph showing the location of ϕ_{75} and its correlating phi value of approximately 9.4

4.6 – Chert as Indicator of Thermal Maturation

Totten and Blatt (1996) studied polycrystalline quartz and its correlation to thermal maturity within the Stanley Formation (Mississippian) of the Ouachita Mountains in southeastern Oklahoma and southwestern Arkansas. They reported that the percentage of fine grained quartz, as well as the mean grain size fraction of quartz, increased in samples of higher maturity. It was determined that as samples became more thermally mature and underwent illitization, the silica released from smectite was being precipitated as authigenic chert. This study was designed to test this hypothesis using cherts from the Woodford shale of the Anadarko basin. The results

obtained differed from those of Totten and Blatt (1996), as there was no evident correlation in the percentage or mean size of cherts in relation to thermal maturity.

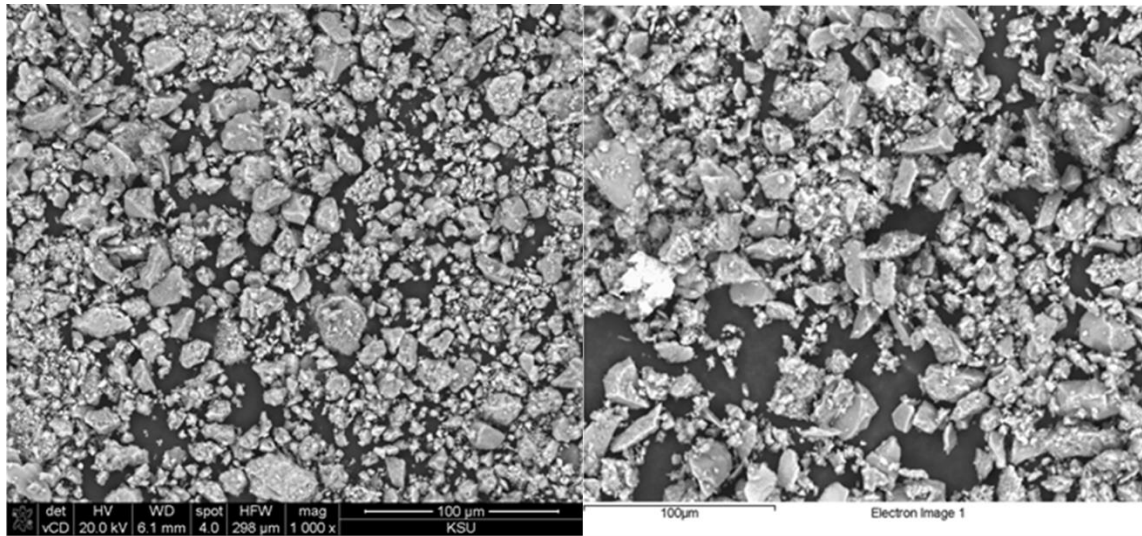
The K/Rb ratio that was obtained through handheld XRF did not show any correlations to the chert size fractions or thermal maturity, which was unexpected. Chaudhuri et al., (2013) discuss how K/Rb ratios, when studied in conjunction with one another, can be indicators for the source of K in a system. The process of transforming smectite to illite requires potassium, and it has been proposed that a possible source of potassium needed for this transformation is from the organic material associated with shale (Totten et al., 2013). The smectite to illite transformation is also noted to release silica, and Totten et al, (1996) have observed this silica to precipitate into many mudrocks as fine grain quartz.

The Woodford Shale is comprised almost entirely of illite clay minerals (Lewan, 1987). The previous work relating changes in clay mineralogy (illitization), and the subsequent growth of authigenic chert, was in rocks with a wide spectrum of thermal maturity, and subsequent mineral transformations. The Woodford has already had these transformations happen, hence the entire sample set was already composed of illite, and there wasn't any silica released to precipitate chert. Totten and Blatt's previous research depicting size correlations to thermal maturity, as well as Chaudhuri's research on the release of silica during the illitization process, had lead us to believe that variation in clay mineralogy, chert percentage and thermal maturity would be related. The Woodford shale is known for its high chert and illite content. Whether these shales are unique and inherited this mineralogy during deposition, or whether the large amount of organic matter drives these reactions at much lower thermal maturities than observed in the samples within this study is not known.

The grain size parameters, graphic mean, median, mode, inclusive graphic standard deviation, inclusive skewness, kurtosis, and fusion weight percentages were plotted against the TOC, vitrinite reflectance, REE, and organic matter weight percent for the ten Woodford samples and can be found in Appendix A. No correlations were observed relating size to thermal maturity. This supports the conclusion that they are depositional in origin.

4.7 – Petrography

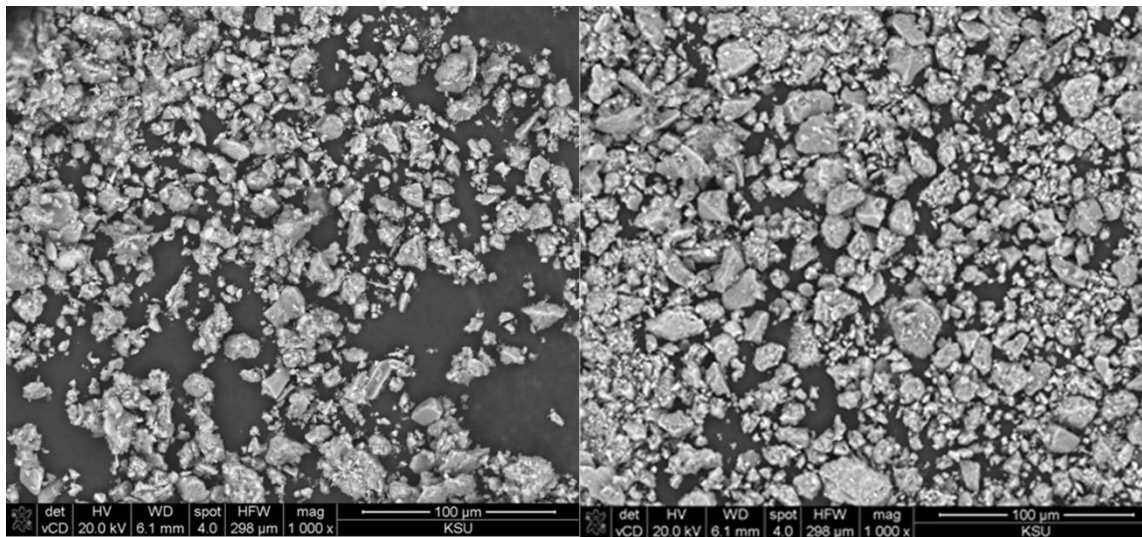
The SEM photomicrograph images were analyzed to look for any differences or variations within the chert fabric. Comparison of the highest vitrinite reflectance (WF#10 Hannah) to the sample of lowest vitrinite reflectance (WF#9 Ne Alden) showed no distinct fabric variations (Figure 34). Comparison of the sample containing the highest TOC (WF#8 Curtis) to the lowest TOC sample (WF#10 Hannah) also showed no distinct variations in the fabric of the cherts (Figure 35). These results were expected after no correlations were observed in the correlation matrix relating TOC and vitrinite to chert sizes. If chert were to be indicative of thermal maturity, based off of previous research one would expect to see an increase in polycrystallinity, and growth and increase in amount within the smaller size fractions.



WF#10 Hannah
 R_0 : 2

WF#9 Ne Alden
 R_0 : 0.47

Figure 34. SEM image comparison of samples containing the highest and lowest vitrinite values.



WF#8 Curtis
 TOC: 11.5

WF#10 Hannah
 TOC: 0.36

Figure 35. SEM image comparison of samples containing the highest and lowest TOC values.

Chapter 5 - Conclusions

Cherts are not an indicator of thermal maturity within the Woodford Shale of the Anadarko Basin, Oklahoma. No correlations were observed between the grain-size and amount of chert present in relation to thermal maturity. Previous studies have indicated that a correlation should be observed. A plausible reason as to why there was no direct correlation observed may be due to the fact that the samples used in this study were already converted to illite, and that the clay transformations seen in previous studies have already occurred. Another complicating factor is that these samples did not contain a wide variation in vitrinite reflectance values, and were from a broad study region. Because the expected clay mineral transformations have already occurred in the Woodford, even in samples with a relatively low thermal maturity of 0.47 vitrinite reflectance, perhaps a new model of shale diagenesis is needed for organic-rich shales. Perhaps the organic matter provides a more abundant source of potassium than normal shales (Totten et al. 2013), and this drives the smectite-illite reaction at lower temperatures. Alternatively, the organic molecules might catalyze the reaction.

The sodium bisulfate fusion procedure used for chert separation within this study had never been attempted on organic-rich mudrocks. Upon completion of the fusion procedure it became apparent that not all of the organics were fused from the sample. Future modifications, such as separating the organics before start of fusion, should be looked into for future studies containing organic-rich mudrocks.

The precision of the handheld XRF, along with strong correlations to the shale mineralogy of the samples that were observed with the handheld XRF indicate that this instrument could prove to be a valuable tool for quick analysis on the rig site. The ability to obtain relatively robust data on Si/Al ratios, along with other elemental data, on cores taken at

the rig site— and to do this quickly (i.e. minutes) and without the need for elaborate sample preparation— could allow for more accurate determinations as to where to hydraulically fracture a formation. Formations with high silica content often prove to obtain the best results when fracking and use of a handheld XRF could allow for fracking targets to be determined on site and in a more efficient manner. The ability to use the XRF to conduct quick analysis on organic matter is also beneficial, as organic matter is often used as a determination as to the quality of a source rock. The ability to use handheld XRF to obtain these data, plus more, with quick results on the drill site could save contractors time and money.

Chapter 6 - Further Research

Upon completion of this study, further research is suggested to help validate the results found.

1. Modify the sodium bisulfate fusion procedure so that organics can be accounted for and removed, leading to more accurate silica weight percent.
2. Reconstruct this study but with samples containing a broader diversity of clay mineralogy.
3. Reconstruct this study on both a more local and regional scale within the Anadarko basin.
4. Conduct further analysis on the silica and cherts in this study to determine its origin.
5. Create a specific Woodford shale calibration on the handheld XRF for better accuracy in analysis.

References

- Attendorf, H. G., & Bowen, R. (1997). *Radioactive and Stable Isotope Geology Issue 3*. Springer Science & Business Media.
- Cardott, B. J., & Lambert, M. W. (1985). Thermal Maturation by Vitrinite Reflectance of Woodford Shale, Anadarko Basin, Oklahoma. *AAPG Bulletin*, v.71, 898-899.
- Chaudhuri, S., Totten, M., Clauer, N., Miesse, J., Riepl, G., Massie, S., et al. (2013). Rare Earth Elements as a Useful Geochemical Tracer in Hydraulic Fracturing Schemes: Shale Shaker. *The Journal of the Oklahoma City Geological Society*, 62, 214-223.
- Coddington, K. (2013). The Role of Heavy Minerals in the Thermal Maturation of the Woodford Shale, Anadarko Basin, Oklahoma. *Thesis Dissertation: Kansas State University Graduate School*.
- Comer, J. B. (2008). Reservoir Characteristics and Production Potential of the Woodford Shale. *World Oil*, 229.
- Dean, M. C., Totten, M. W., & Falster, A. U. (1995). Separation of Heavy Minerals from Mudrocks. *Journal of Sedimentary Research*, 65, 563-566.
- Energy Information Administration (EIA) (2011) Shale Gas is a Global Phenomenon. Today in Energy, <http://www.eia.gov/todayinenergy/detail.cfm?id=811>, accessed Jan 24, 2013.
- Fishman, N. S., Ellis, G. S., Paxton, S. T., Abbott, M. M., & Boehlke, A. (2010). Gas Storage in the Upper Devonian-Lower Mississippian Woodford Shale, Arbuckle Mountains, Oklahoma: How Much of a Role Do the Cherts Play? *AAPG Search and Discovery*, #90122.
- Folk, R. L. (1981). *Petrology of Sedimentary Rocks* (2 ed.). Austin, Texas: Hemphill Publishing Company.
- Fritz, R. D., Horn, M. K., & Joshi, S. D. (1991). Geological Aspects of Horizontal Drilling, Tulsa: AAPG, 563p.
- Halliburton. (2014). *Woodford Shale-A Complex Oil and Gas Play*. Retrieved September 2014, from <http://www.halliburton.com>
- Ham, W. E., & Merritt, C. A. (1944). Barite in Oklahoma. *Oklahoma Geological Survey Circular 23*, 5-42.
- Henry, M. E., and Hester, T.C., 1995, Anadarko Basin Province (058), in Gautier, D. L., Dolton, G.L., Takahashi, K.I., and Varnes, K.L., ed., 1995 National assessment of United States oil and gas resources--Results, methodology, and supporting data: U.S. Geological Survey Digital Data Series DDS-30, Release 2, one CD-ROM.
- Jackson, J. A. (2003). *Glossary of Geology* (4 ed.). Springer.

- King, H. (2005). *What is chert, how does it form, and what is it used for?* Retrieved September 2014, from <http://geology.com>
- Kirkland, D.W., Denison, R.E., Summers, D.M., and Gormly, J.R., (1992). Geology and Organic Geochemistry of the Woodford Shale in the Criner Hills and Western Arbuckle Mountains, Oklahoma. *Oklahoma Geological Survey Circular v. 93*, 38-69.
- Kuuskraa, V. (2011). Economic and Market Impacts of Abundant Shale Gas Resources. Advance Resources International, 2011.
- Lambert, M.W., (1990). Internal Stratigraphy of the Chattanooga Shale in Kansas and Oklahoma, in Johnson, K.S. and B.J. Cardott (eds.) Source Rocks in the Southern Midcontinent, 1990 symposium: Oklahoma Geological Society Circular 93, 94-103.
- Lash, G., & Blood, R. (2012, November). Barite Mobilization in the Upper Devonian Succession of Western New York- Evidence for Anaerobic Methane Oxidation and Methanogenesis during Quasi-Steady State Burial. *AAPG Search and Discovery*, #50744.
- Lewan M.D., Maynard, J.B., 1982. Factors controlling enrichment of vanadium and nickel in the bitumen of organic sedimentary rocks: *Geochimica et Cosmochimica Acta*, v. 46, p. 2547-2560.
- Meurant, G. (2012). *Handbook of Strat-Bound and Strataform Ore Deposits* (Vol. 9). Elsevier.
- Northcutt, R., & Campbell, J. (1996). Geologic Provinces of Oklahoma. *The Shale Shaker*, 46(5), 99-103. Retrieved from AAPG.
- Potter, P.E., Maynard, J.B., and Pryor, W.A. (1980). *Sedimentology of Shale*. Springer Verlag, New York.
- Ramirez-Caro, D. (2013). Rare Earth Elements (REE) as Geochemical Clues to Reconstruct Hydrocarbon Generation History. *Thesis Dissertation: Kansas State University Graduate School*.
- Sorenson R.P., (2005). A Dynamic Model for the Permian Panhandle and Hugoton Fields, Western Anadarko Basin: *AAPG Bulletin*, v.89, 921-938.
- Totten, M. W., Blatt H., 1996. Sources of silica from the illite to muscovite transformation during late-stage diagenesis of shales, Siliciclastic diagenesis and fluid flow, Concepts and Applications: Society of Economic Paleontologists and Mineralogists, Special Publication No. 55, p. 85-92
- Totten, M.W., and Hanan, M.A., 1998, The Accessory Mineral Fraction of Mudrocks and its Significance for Whole-rock Trace-element Geochemistry: in Schieber, J., Zimmerle, W., and Sethi, P., eds., *Shales and Mudstones: Volume I: Petrography, Petrophysics, Geochemistry and Economic Geology*; Publisher: Schweizerbart, Stuttgart/Germany, p. 35-53.

Appendix A -

A.1 – SEM and EDS Spectra

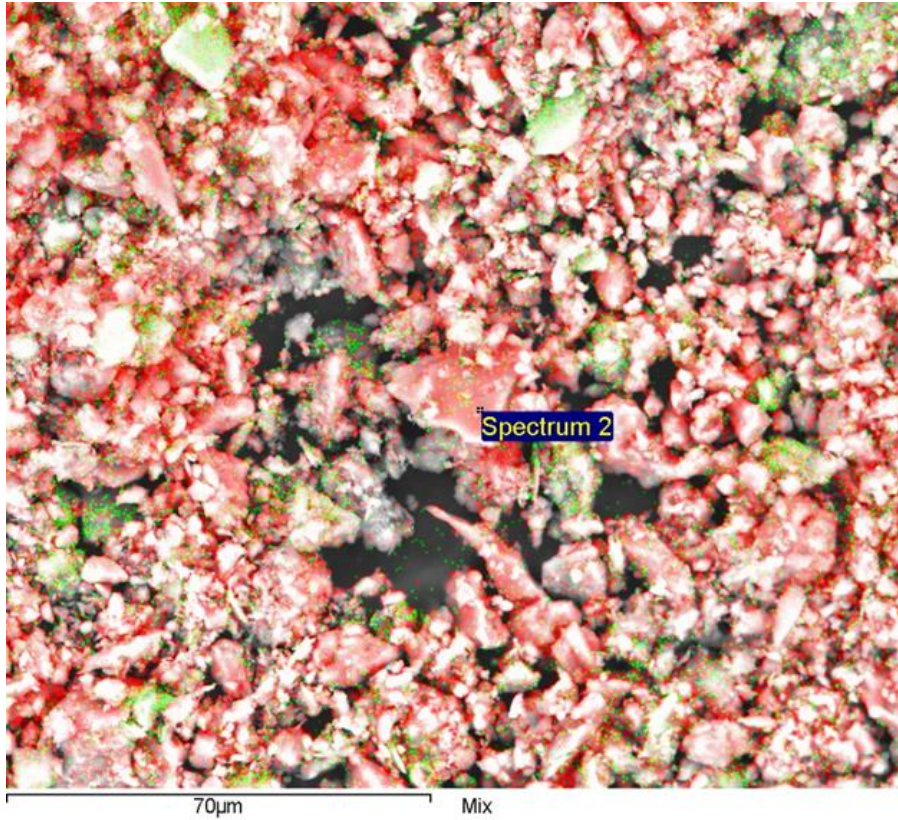


Figure A.1.1. SEM image of chert in WF#1 McCalla Ranch and associated Spectra. Red indicates silica and green aluminum.

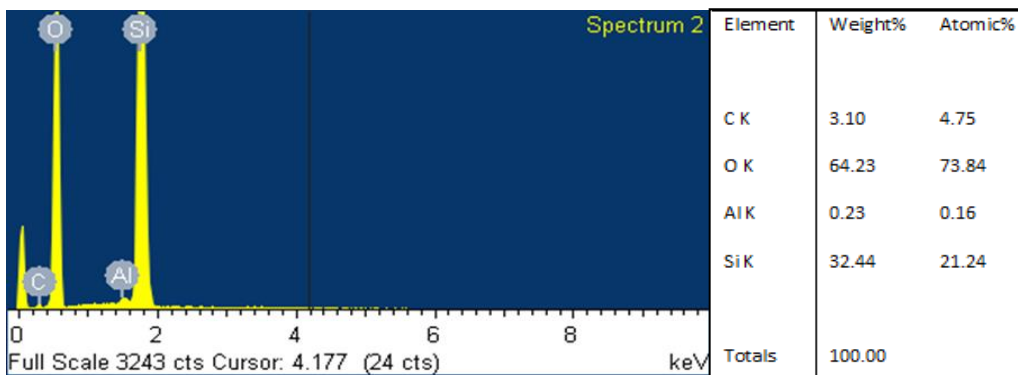


Figure A.1.2. EDS Spectra for WF#1 McCalla Ranch.

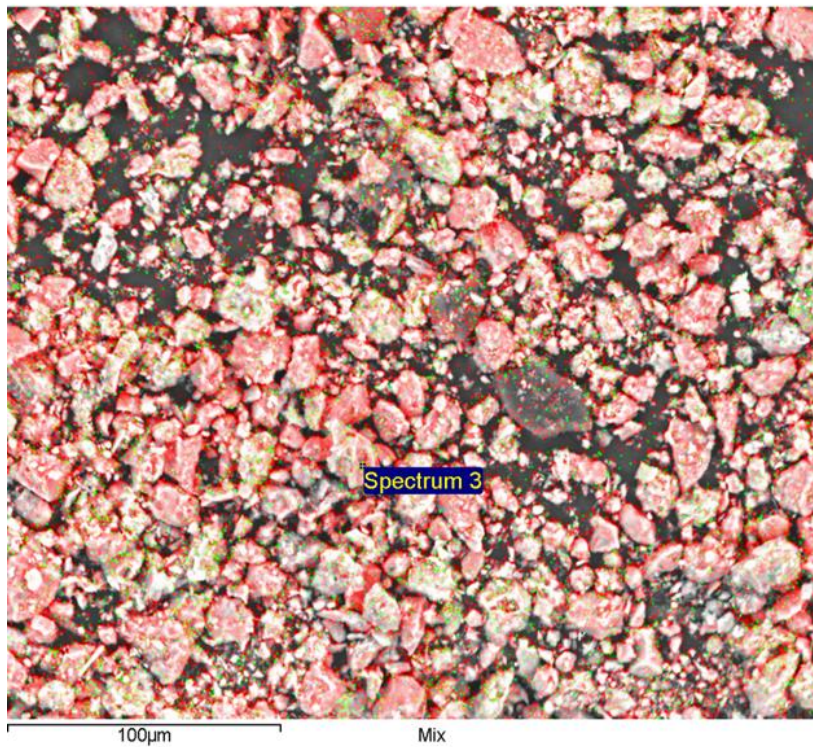


Figure A.1.3. SEM image of chert in WF#2 Sara Kirk and associated Spectra. Red indicates silica and green aluminum.

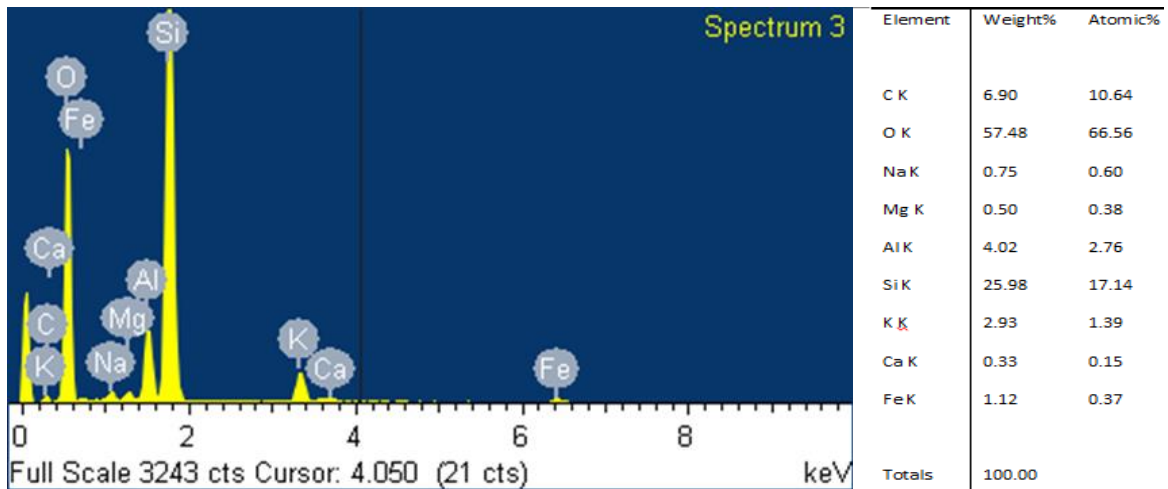


Figure A.1.4. EDS Spectra for WF#2 Sara Kirk.

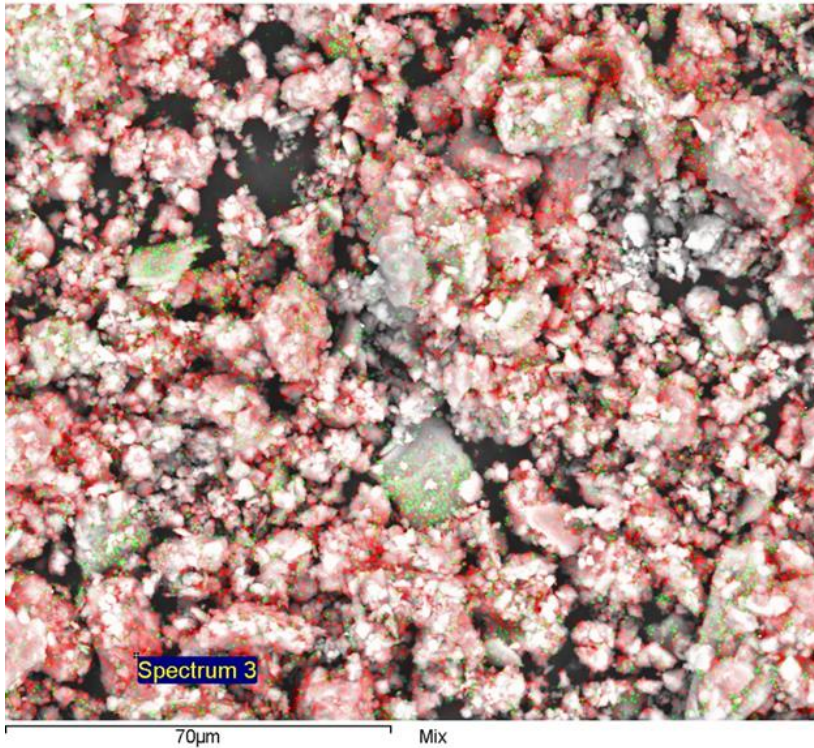


Figure A.1.5. SEM image of chert in WF#4 Guthrie and associated Spectra. Red indicates silica and green aluminum.

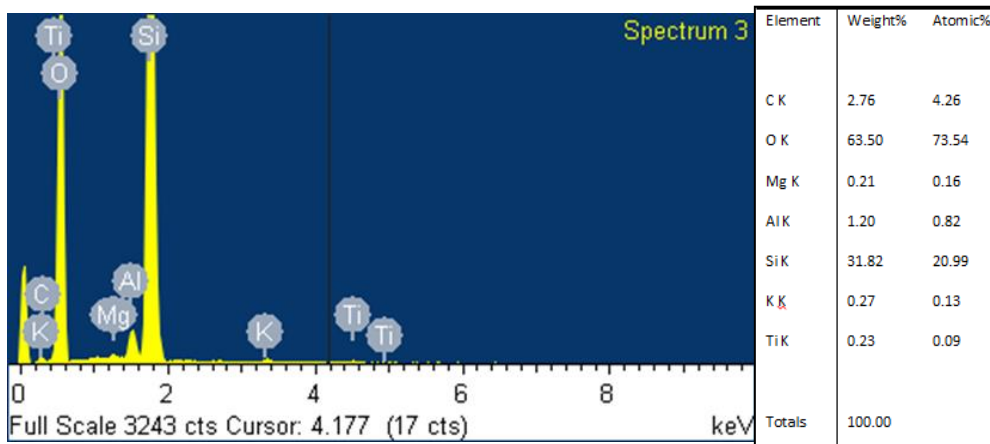


Figure A.1.6. EDS Spectra for WF#4 Guthrie.

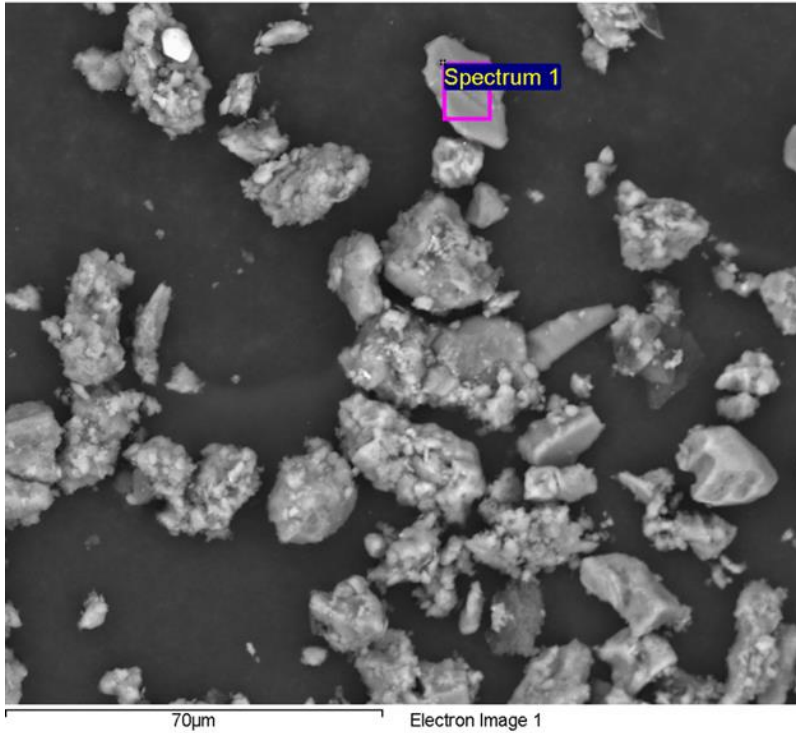


Figure A.1.7. SEM image of chert in WF#5 Dwyer Mt and associated Spectra.

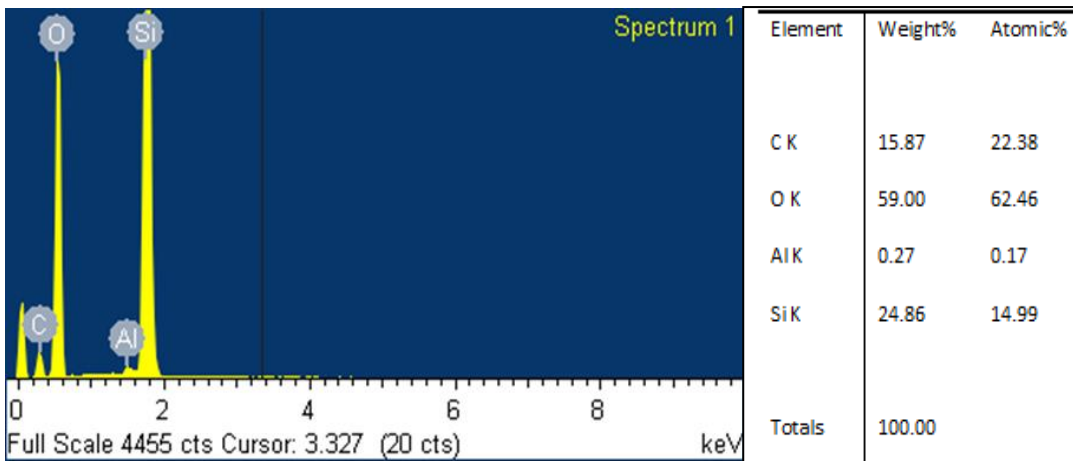


Figure A.1.8. EDS Spectra for WF#5 Dwyer Mt.

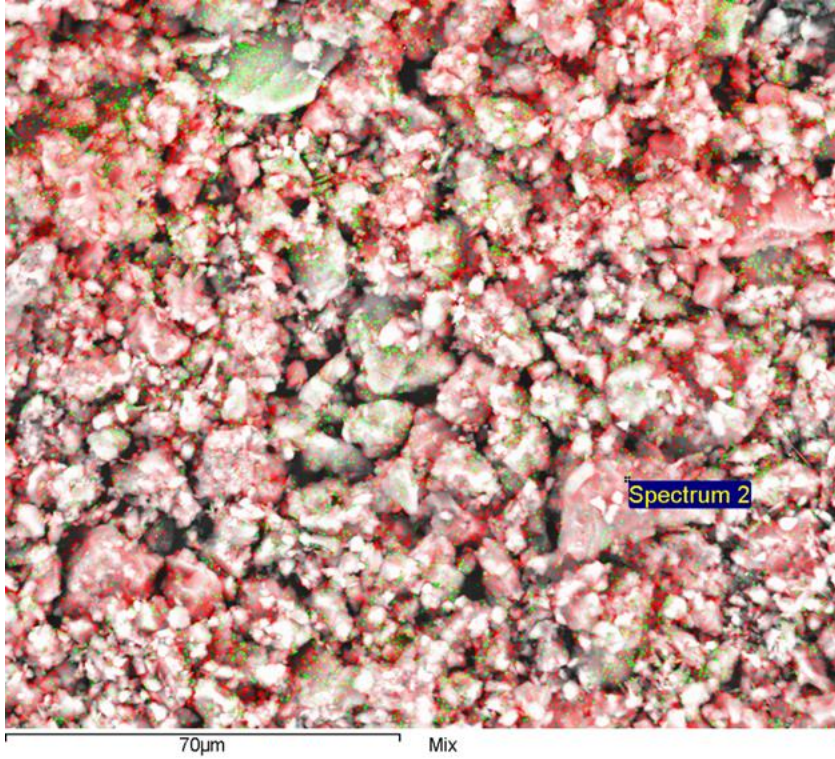


Figure A.1.9. SEM image of chert in WF#6 Cement Ord and associated Spectra. Red indicates silica and green aluminum.

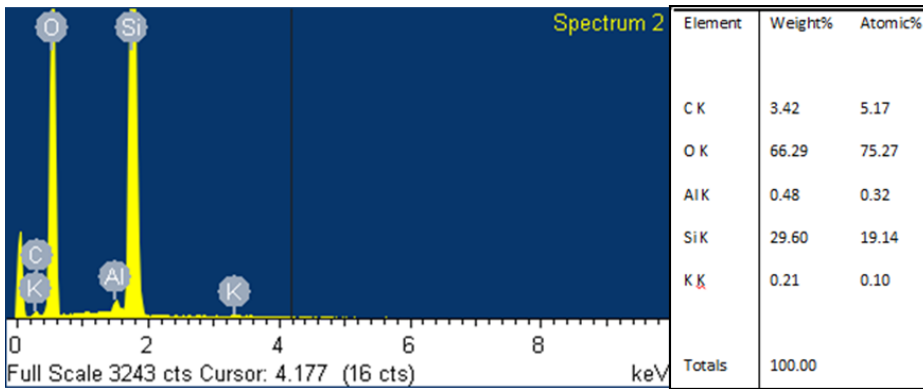


Figure A.1.10. EDS Spectra for WF#6 Cement Ord.

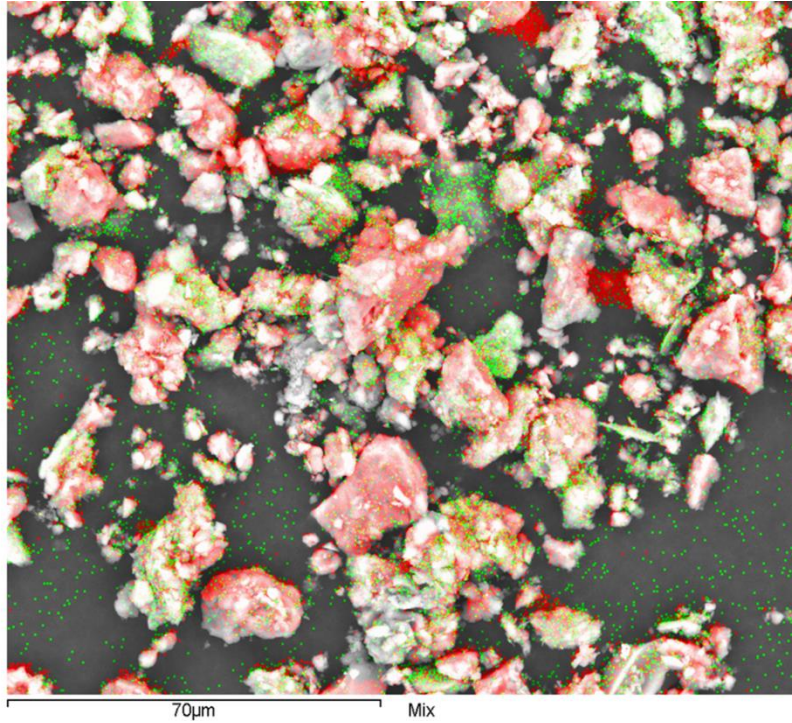


Figure A.1.11. SEM image of chert in WF#8 Curtis and associated Spectra. Red indicates silica and green aluminum.

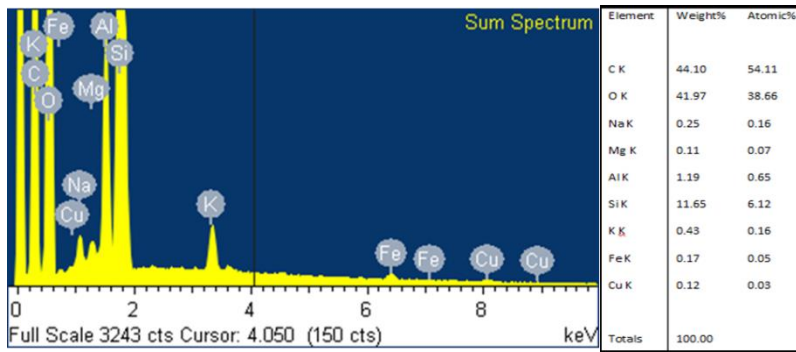


Figure A.1.12. EDS Spectra for WF#8 Curtis.

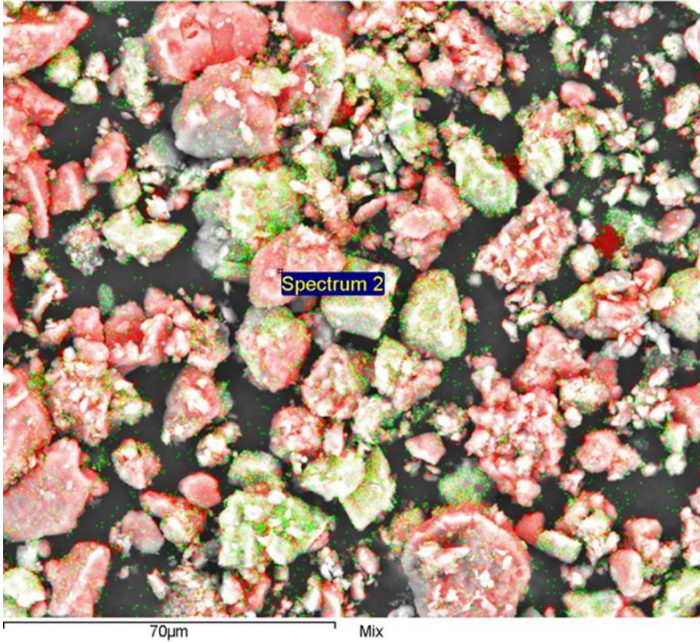


Figure A.1.13. SEM image of chert in WF#10 Hannah and associated Spectra. Red indicates silica and green aluminum.

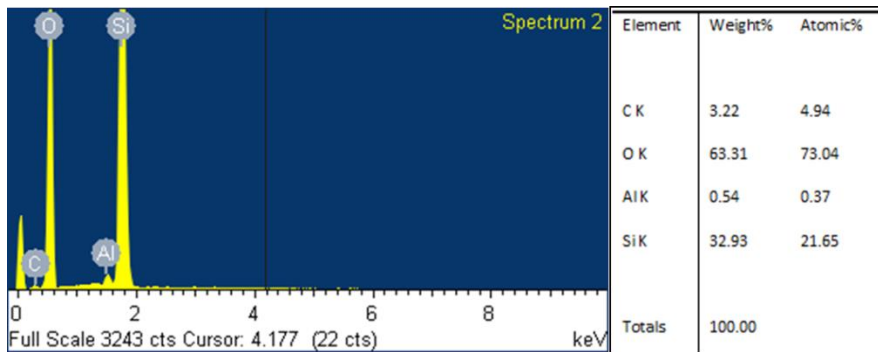


Figure A.1.14. EDS Spectra for WF#10 Hannah.

A.2 – Grain Size Images

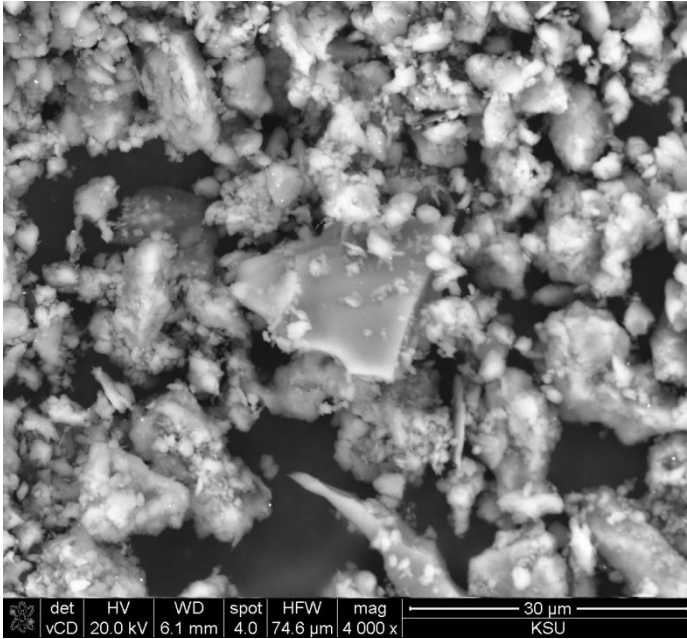


Figure A.2.1. SEM image used for grain size analysis of WF#1 McCalla Ranch.

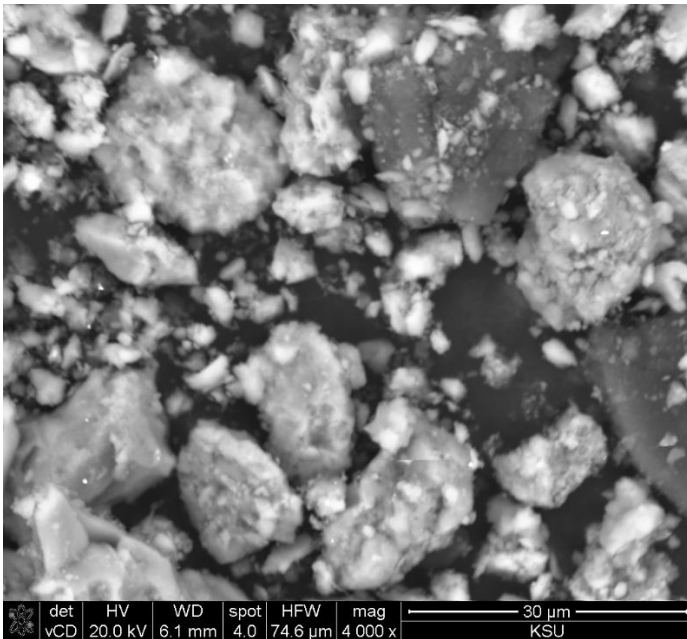


Figure A.2.2. SEM image used for grain size analysis of WF#2 Sara Kirk.

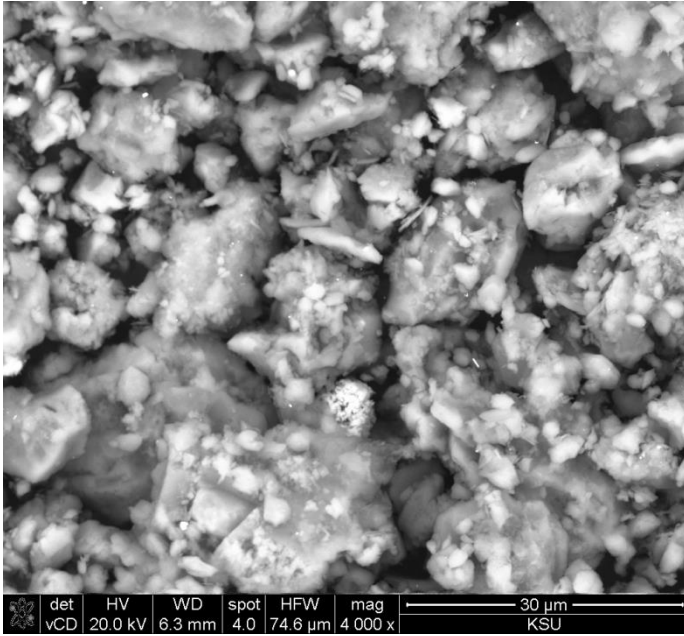


Figure A.2.3. SEM image used for grain size analysis of WF#3 Lela Rahm.

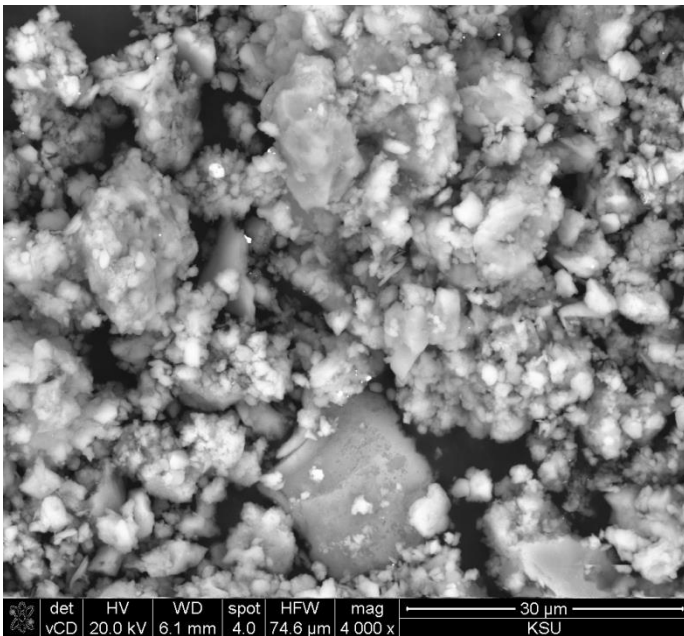


Figure A.2.4. SEM image used for grain size analysis of WF#4 Guthrie.

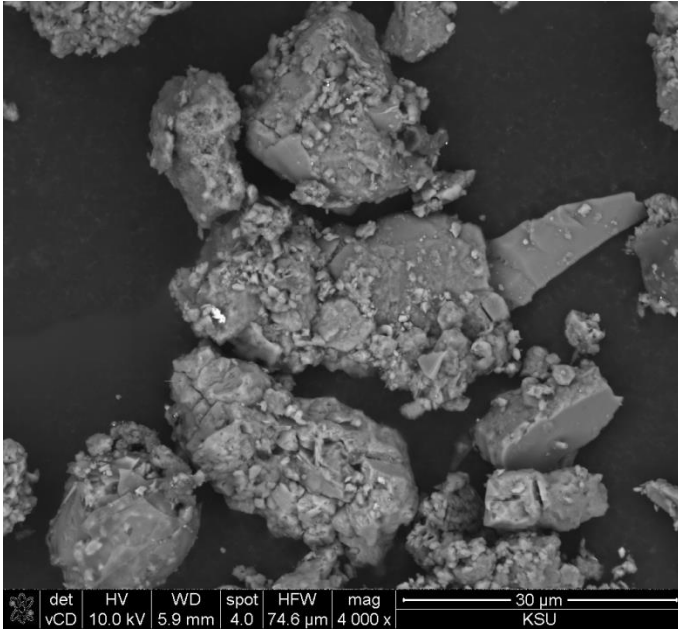


Figure A.2.5. SEM image used for grain size analysis of WF#5 Dwyer Mt.

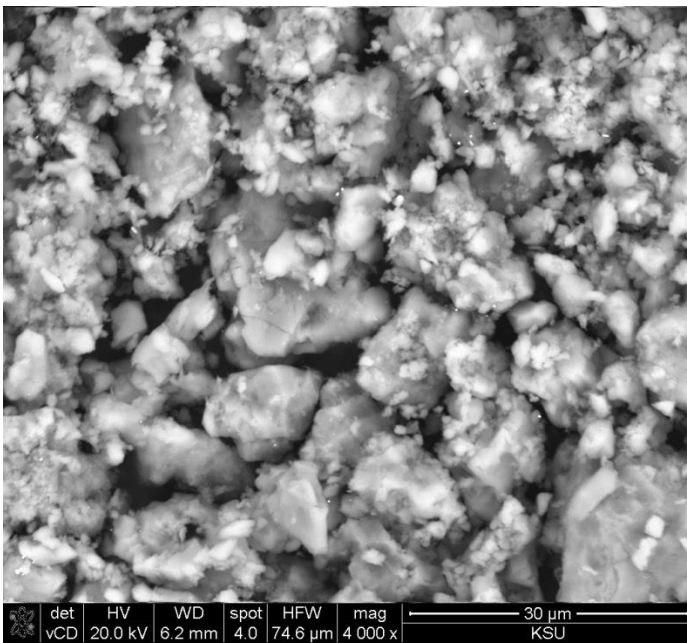


Figure A.2.6. SEM image used for grain size analysis of WF#6 Cement Ord.

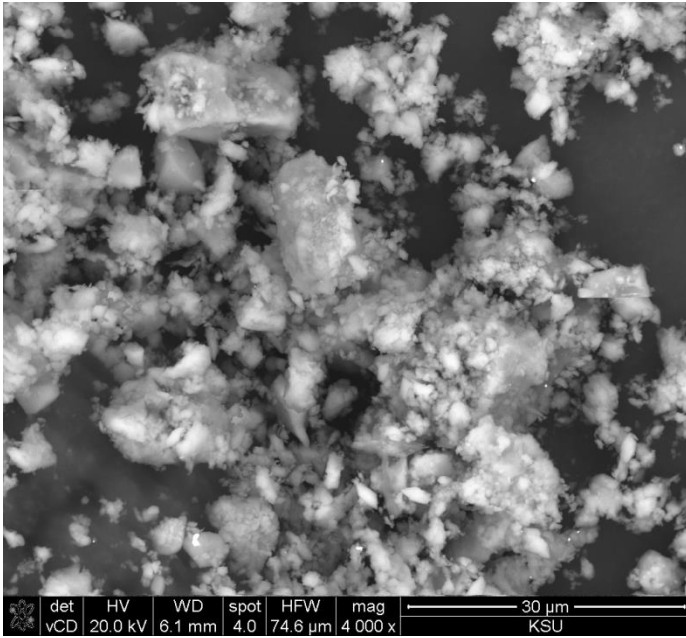


Figure A.2.7. SEM image used for grain size analysis of WF#7 Chenoweth.

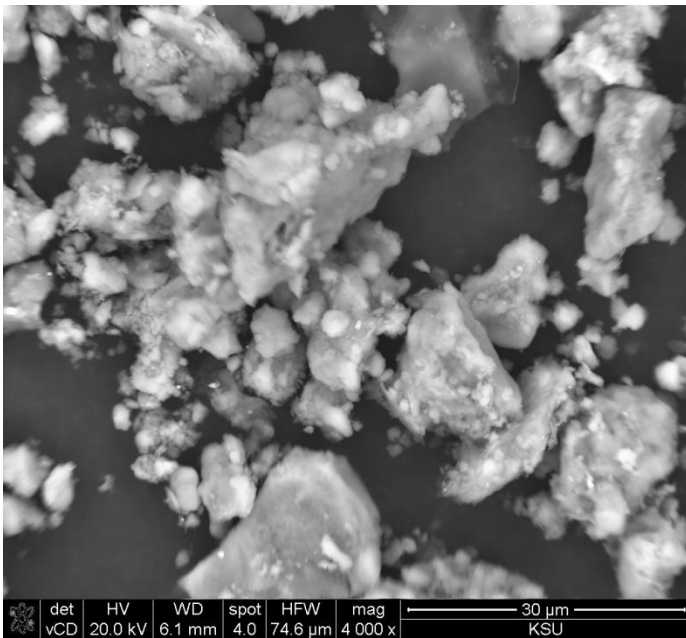


Figure A.2.8. SEM image used for grain size analysis of WF#8 Curtis.

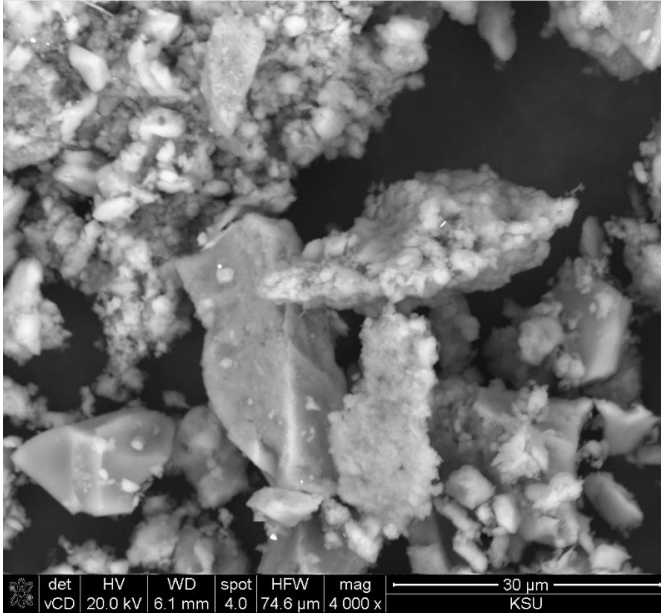


Figure A.2.9. SEM image used for grain size analysis of WF#9 Ne Alden.

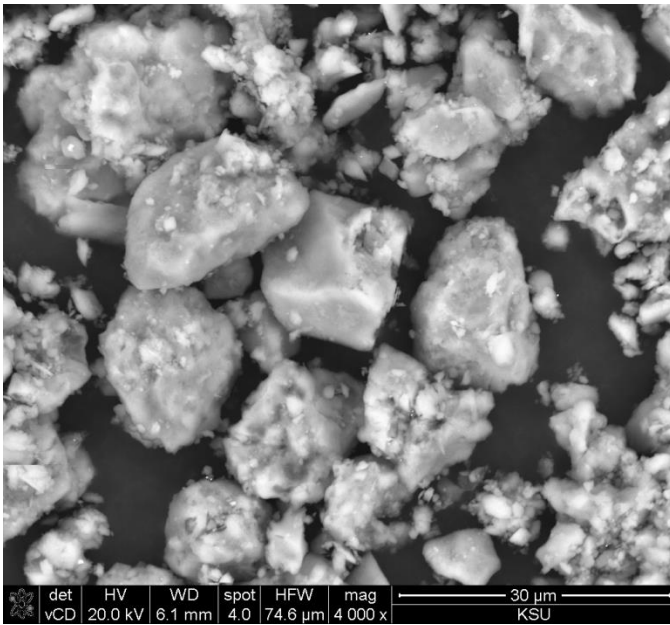


Figure A.2.10. SEM image used for grain size analysis of WF#10 Hannah.

A.3 – Cumulative Curve Plots

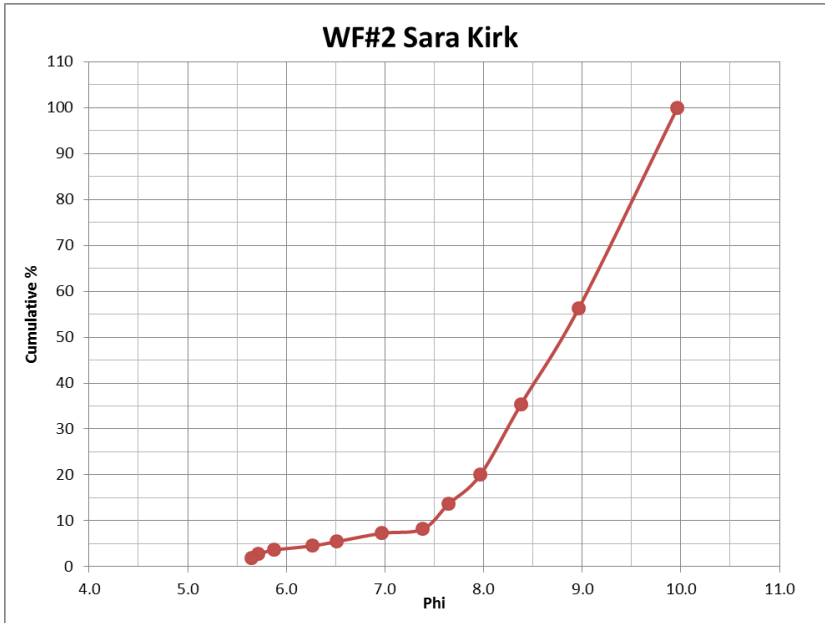


Figure A.3.1. Cumulative curve plot for WF#2 Sara Kirk.

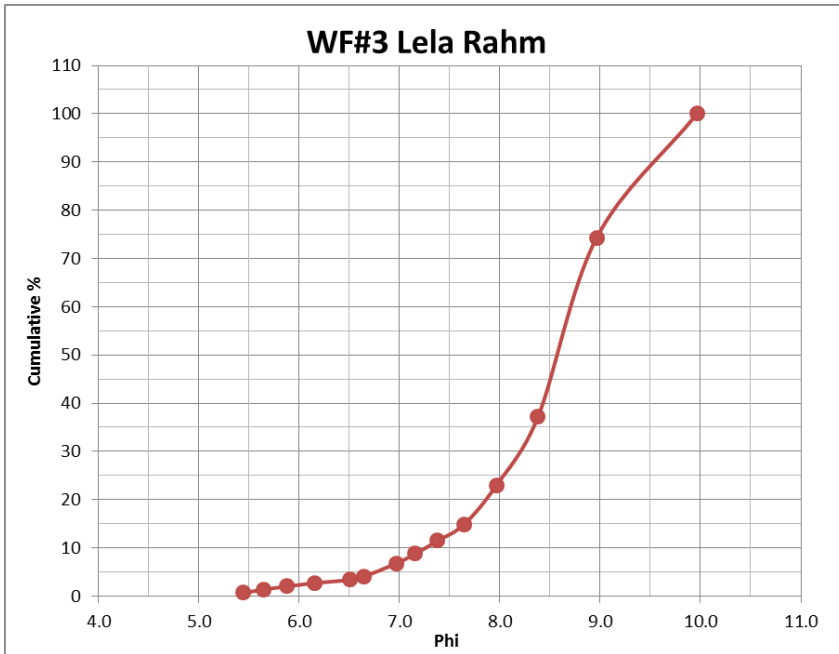


Figure A.3.2. Cumulative curve plot for WF#3 Lela Rahm.

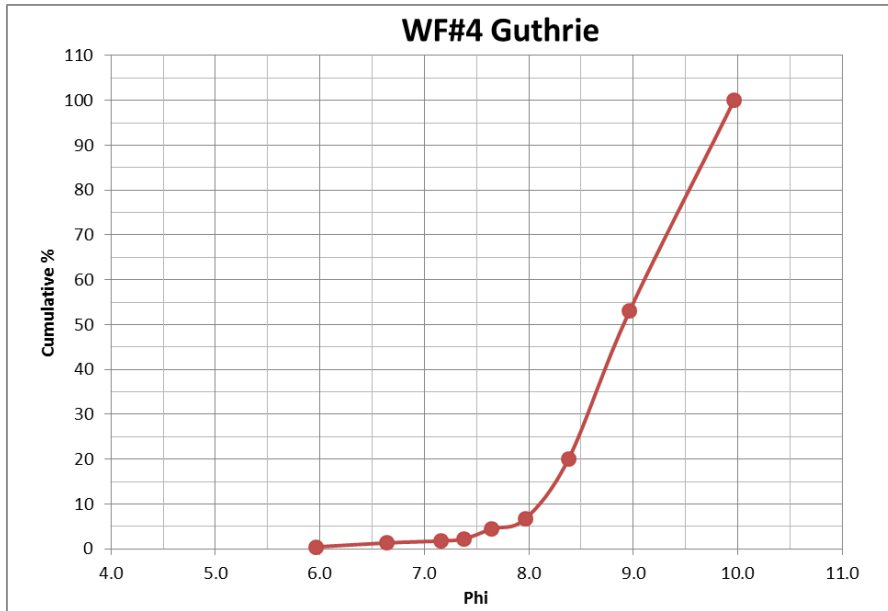


Figure A.3.3. Cumulative curve plot for WF#4 Guthrie.

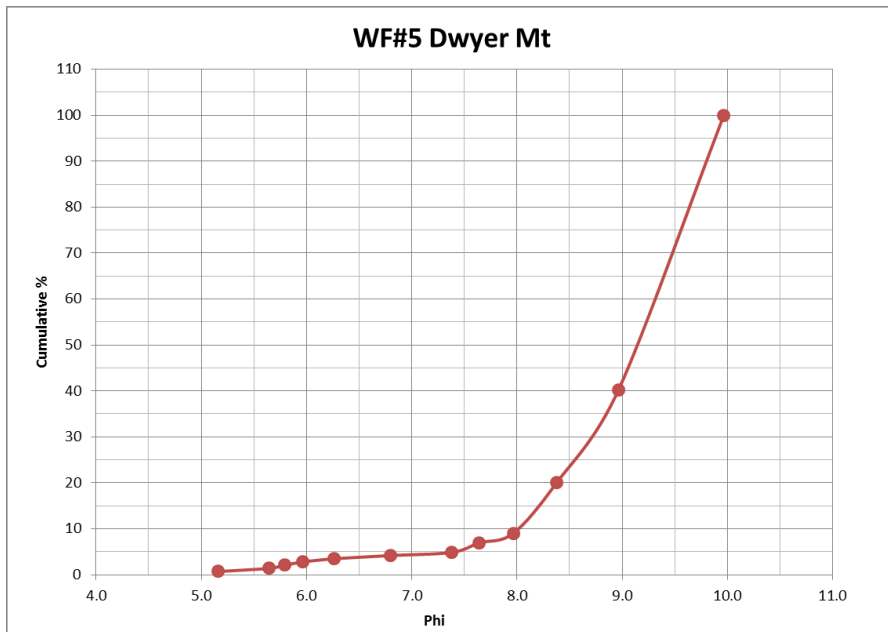


Figure A.3.4. Cumulative curve plot for WF#5 Dwyer Mt.

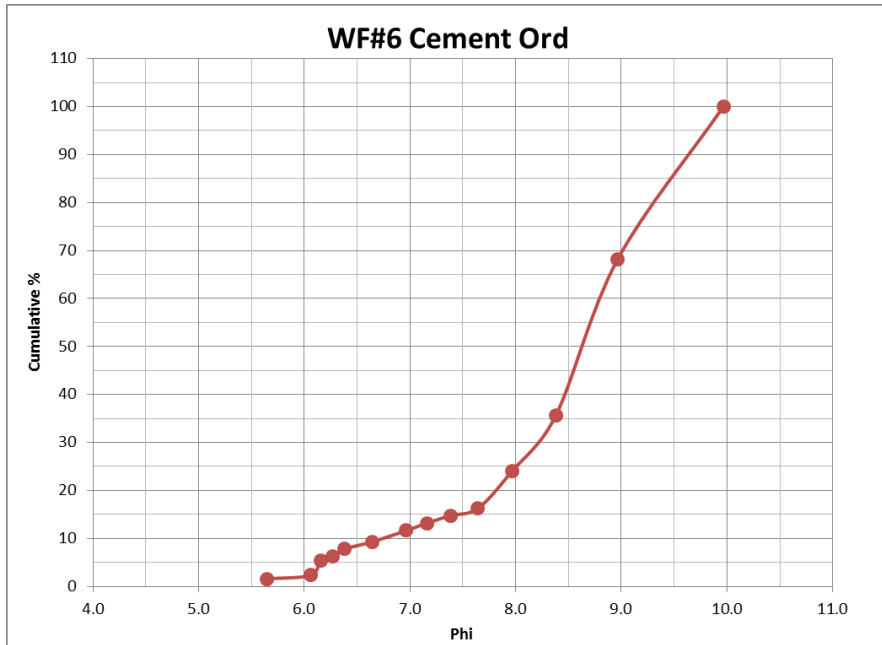


Figure A.3.5. Cumulative curve plot for WF#6 Cement Ord.

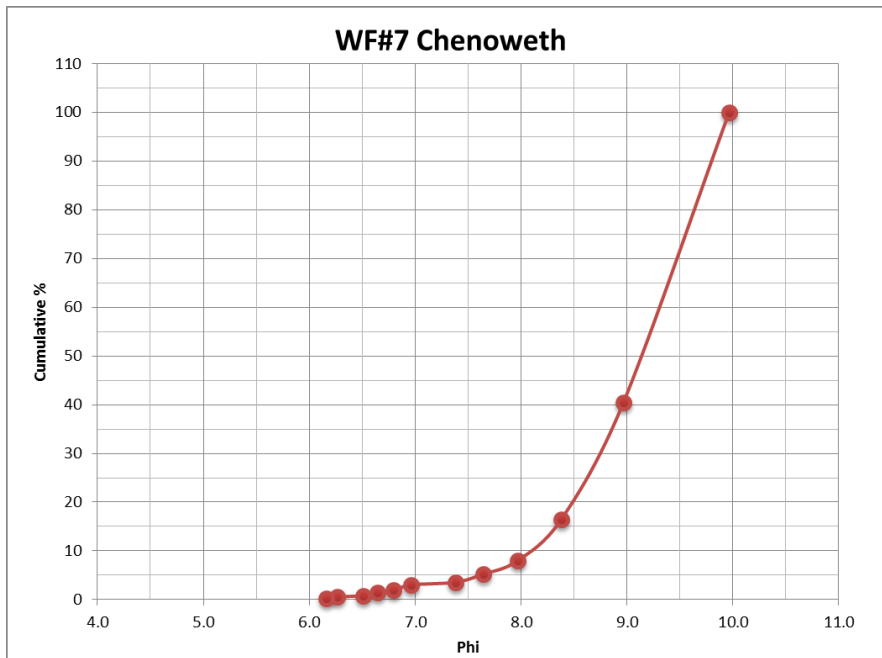


Figure A.3.6. Cumulative curve plot for WF#7 Chenoweth.

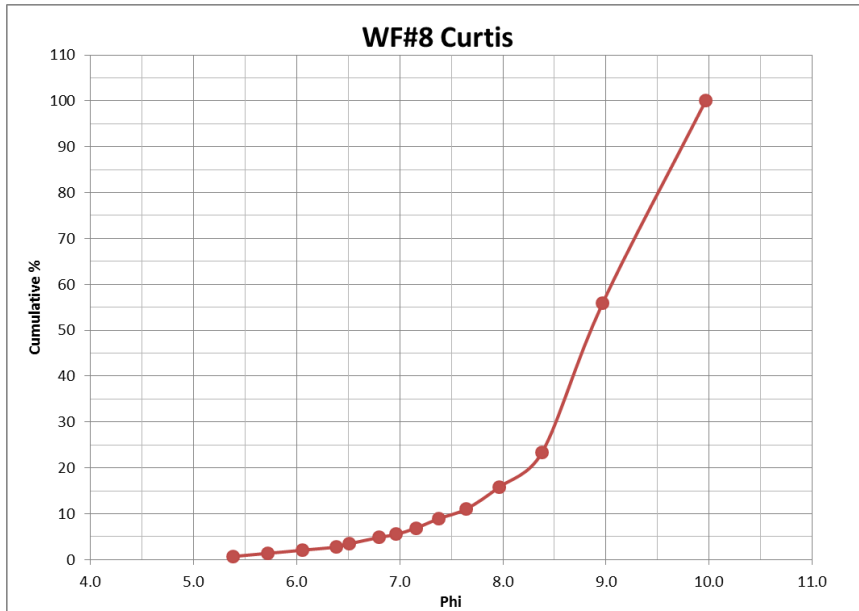


Figure A.3.7. Cumulative curve plot for WF#8 Curtis.

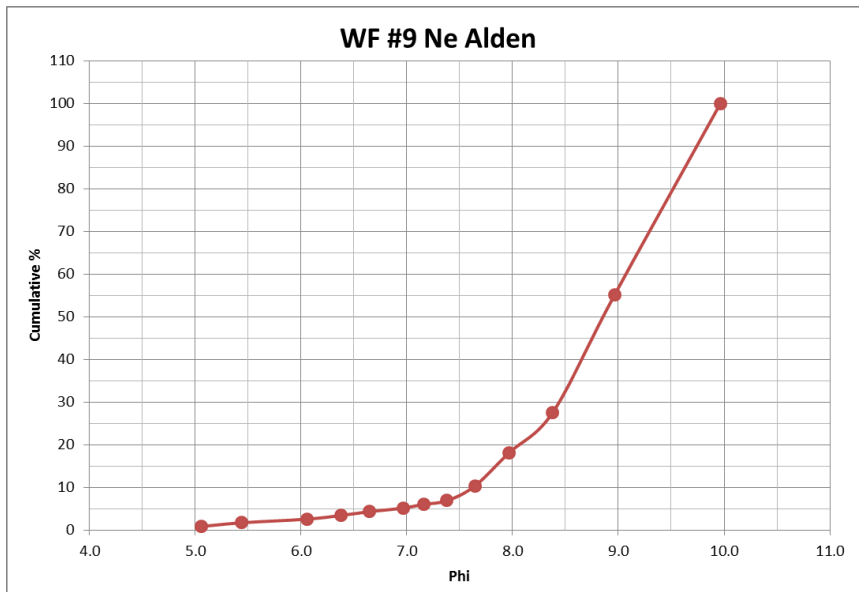


Figure A.3.8. Cumulative curve plot for WF#9 Ne Alden.

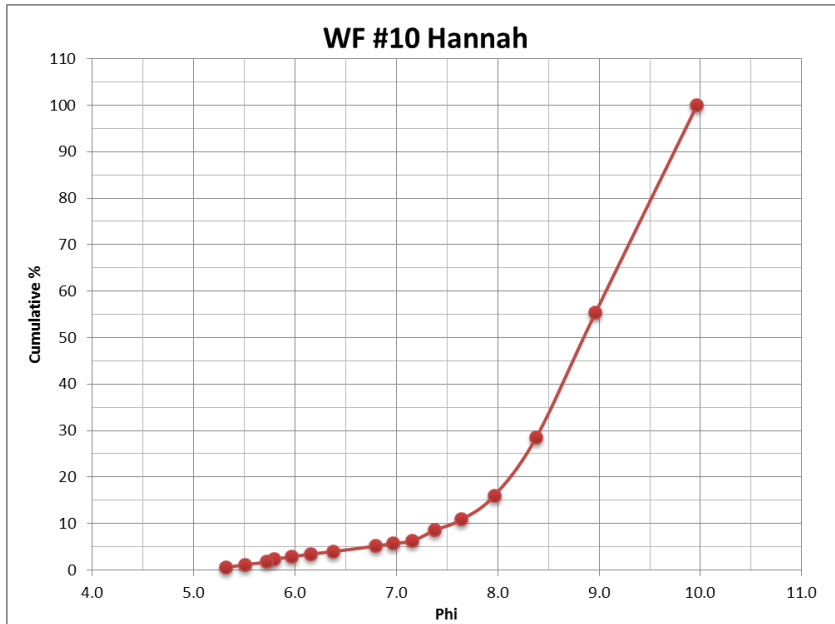


Figure A.3.9. Cumulative curve plot for WF#10 Hannah.

A.4 – K/Rb

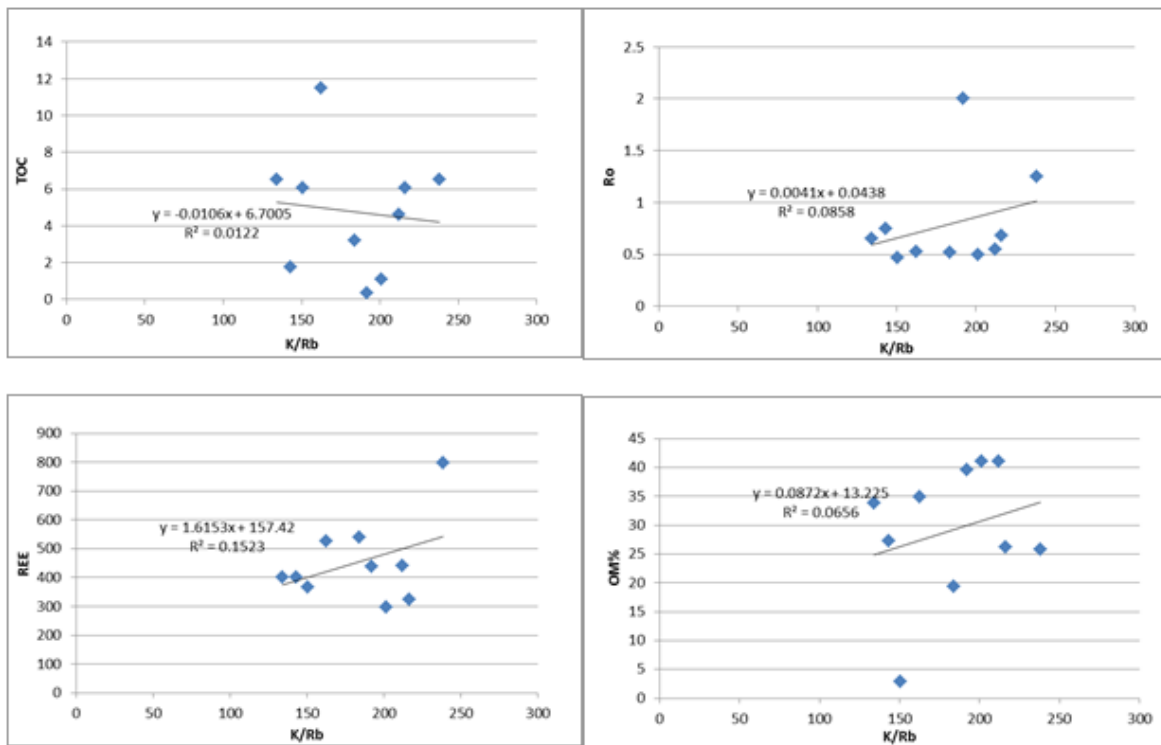


Figure A.4.1. Plots depicting no correlation between K/Rb and TOC, Ro, REE, and organic matter.

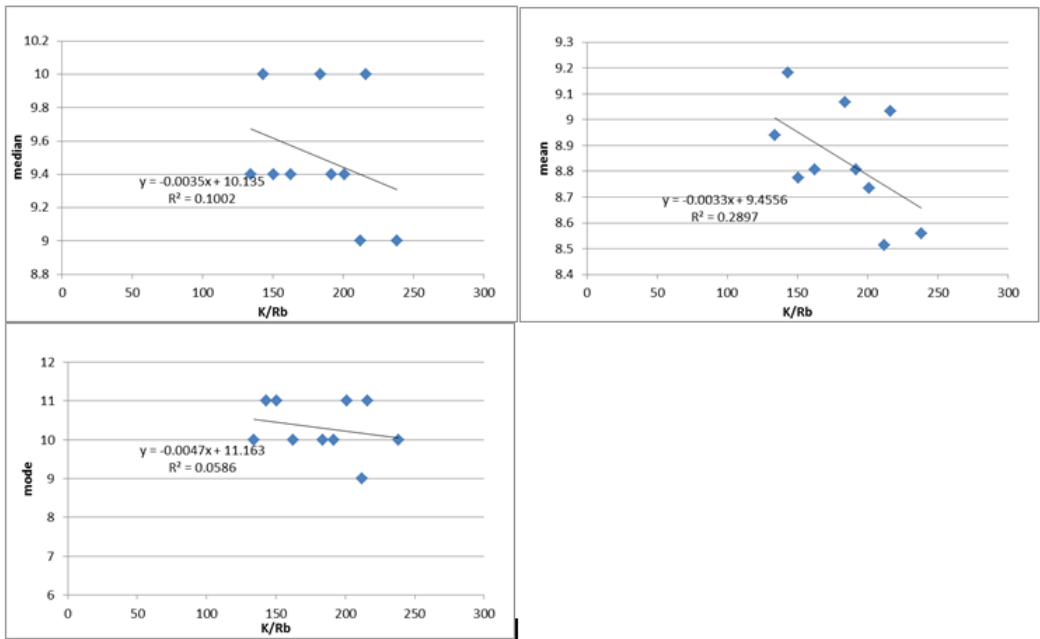


Figure A.4.2. Plots depicting no correlation between K/Rb and grain size mean, median, and mode.

A.5 – Correlation Graphs

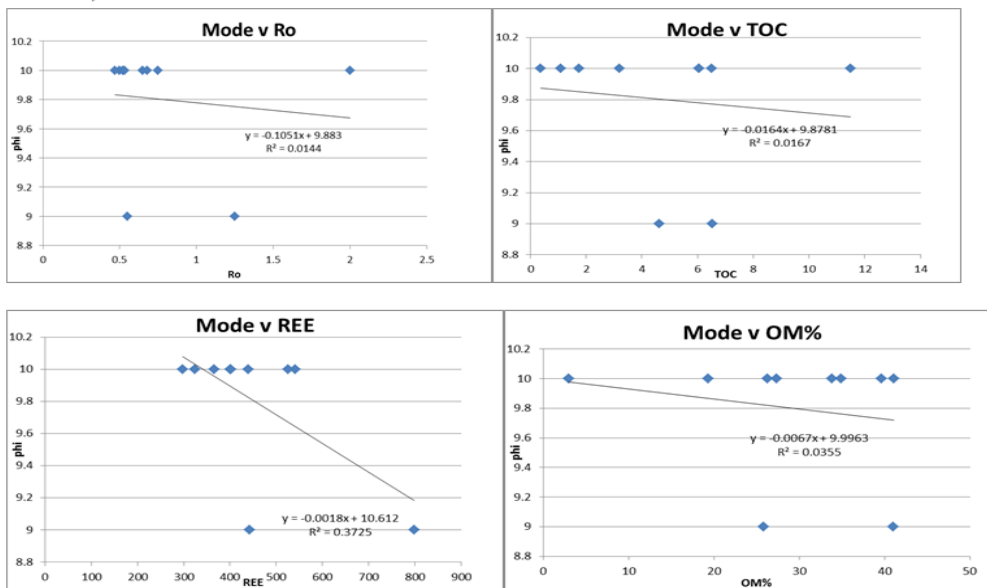


Figure A.5.1. Plots depicting no correlation between mode and TOC, Ro, REE, and organic matter.

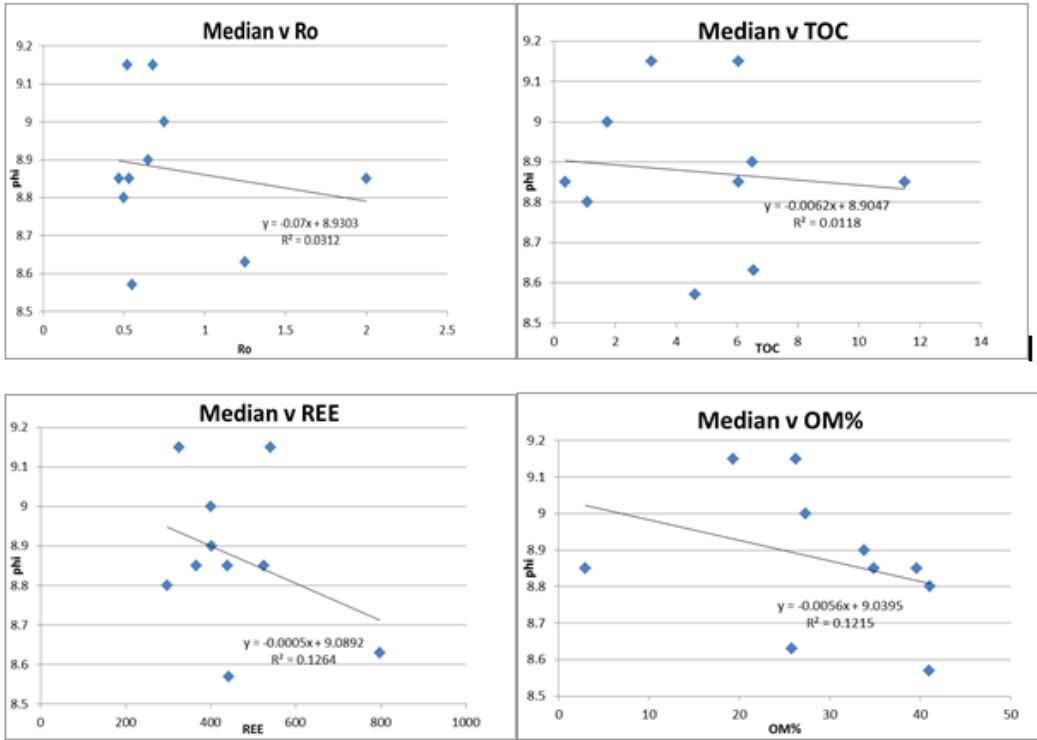


Figure A.5.2. Plots depicting no correlation between median and TOC, Ro, REE, and organic matter.

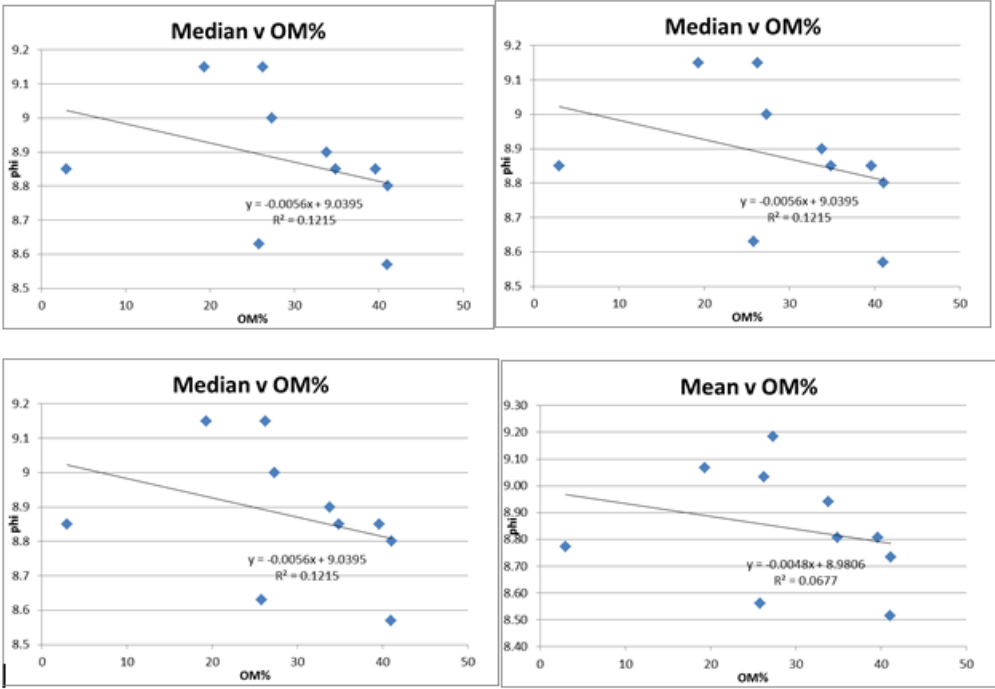


Figure A.5.3. Plots depicting no correlation between mean and TOC, Ro, REE, and organic matter.

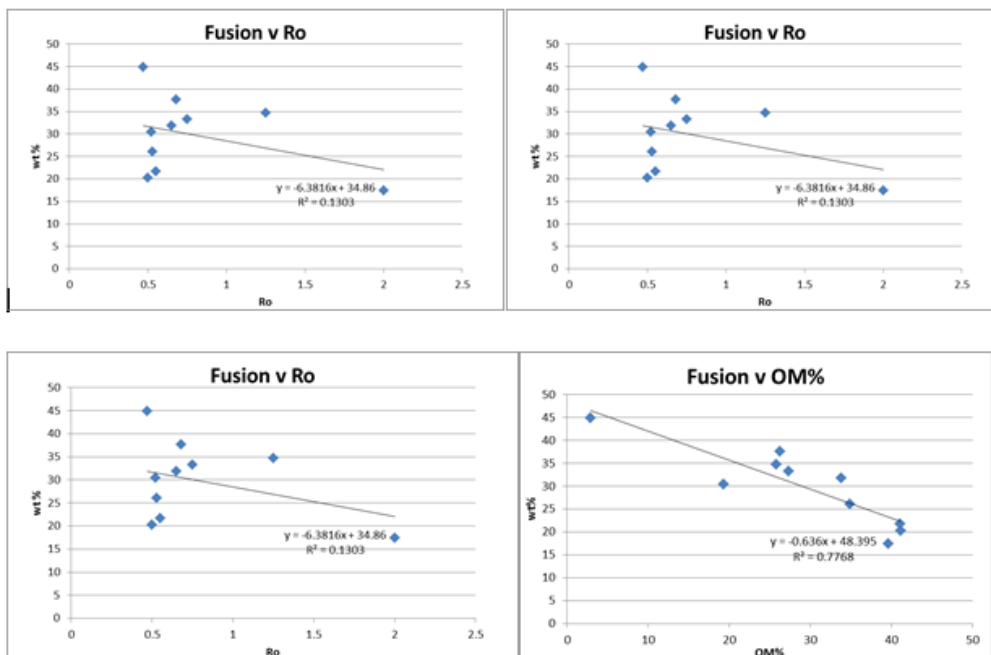


Figure A.5.4. Plots depicting no correlation between fusion weight percent and TOC, Ro, REE, and organic matter.

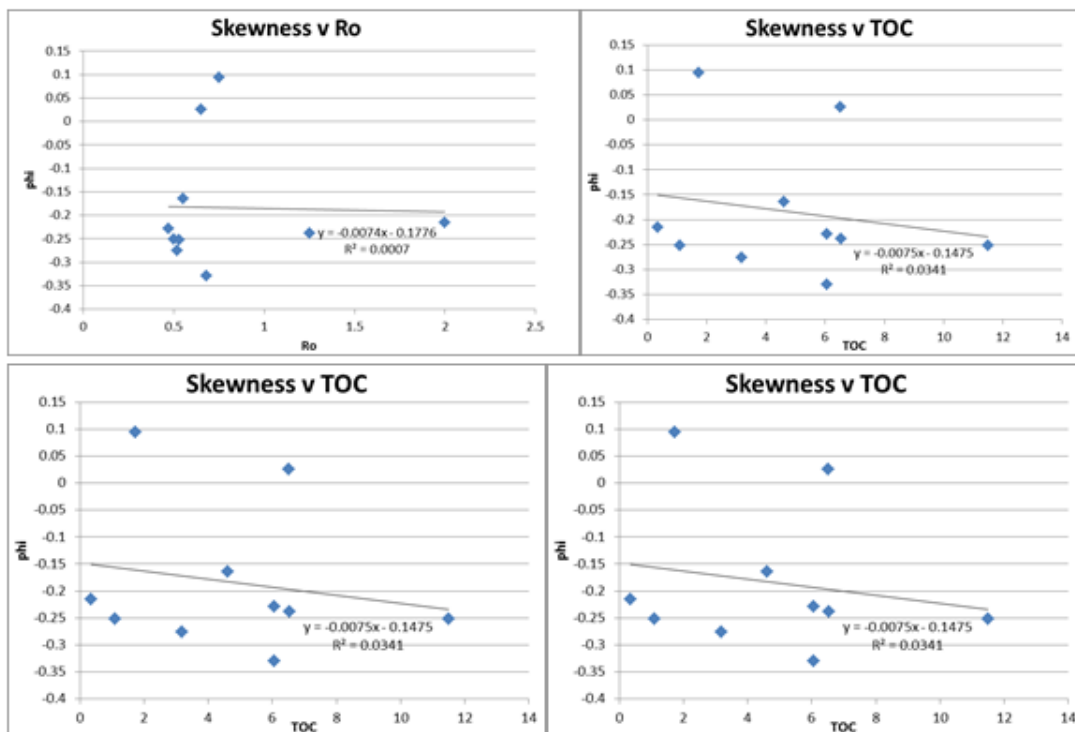


Figure A.5.5. Plots depicting no correlation between skewness and TOC, Ro, REE, and organic matter.

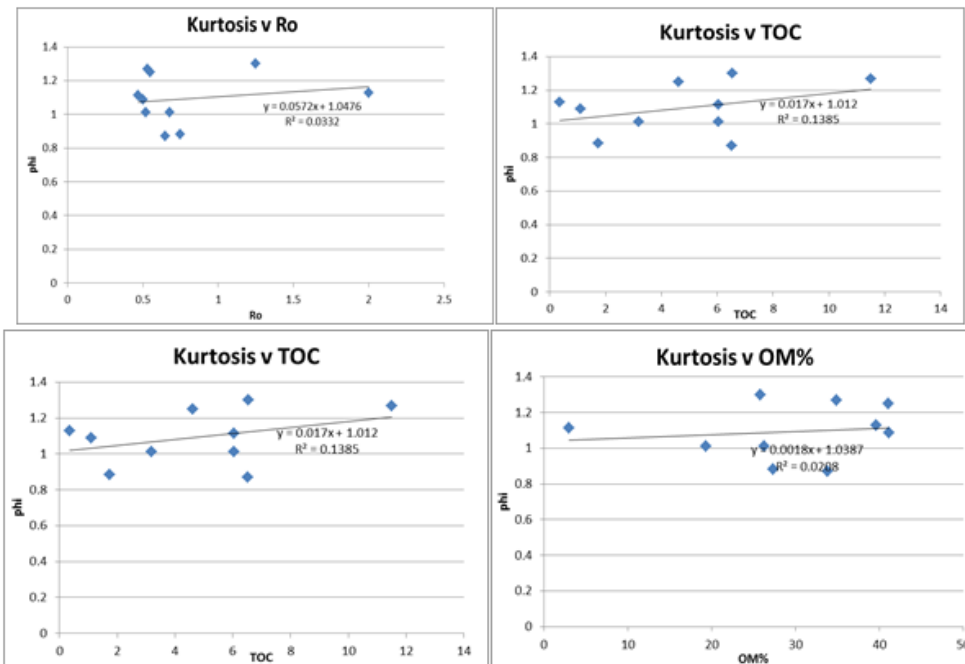


Figure A.5.6. Plots depicting no correlation between kurtosis and TOC, Ro, REE, and organic matter.

A.6 – Grain Size

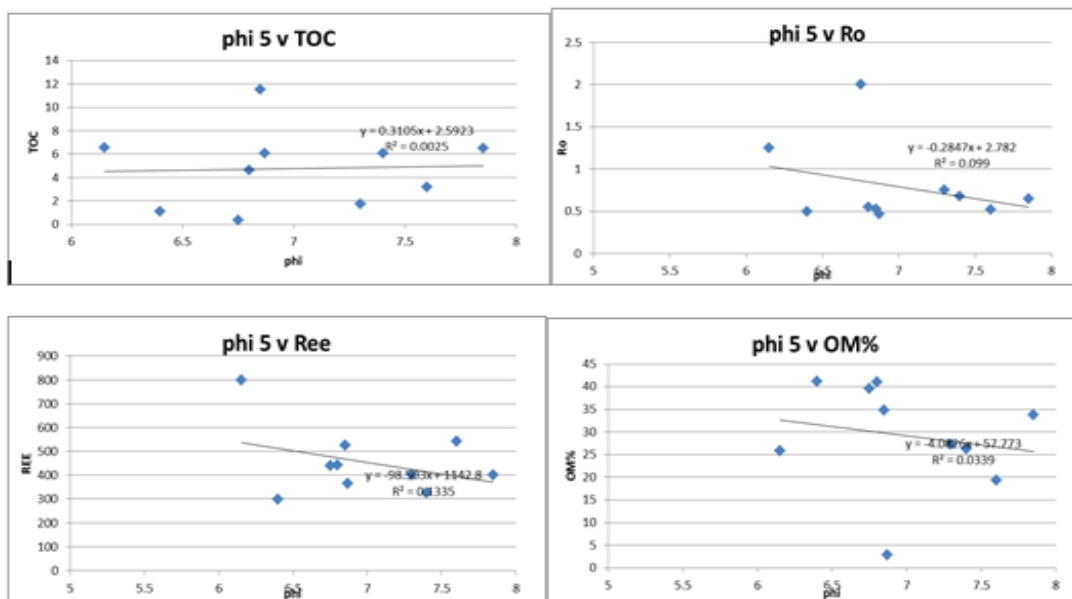


Figure A.6.1. Plots depicting no correlation between phi 5 and TOC, Ro, REE, and organic matter.

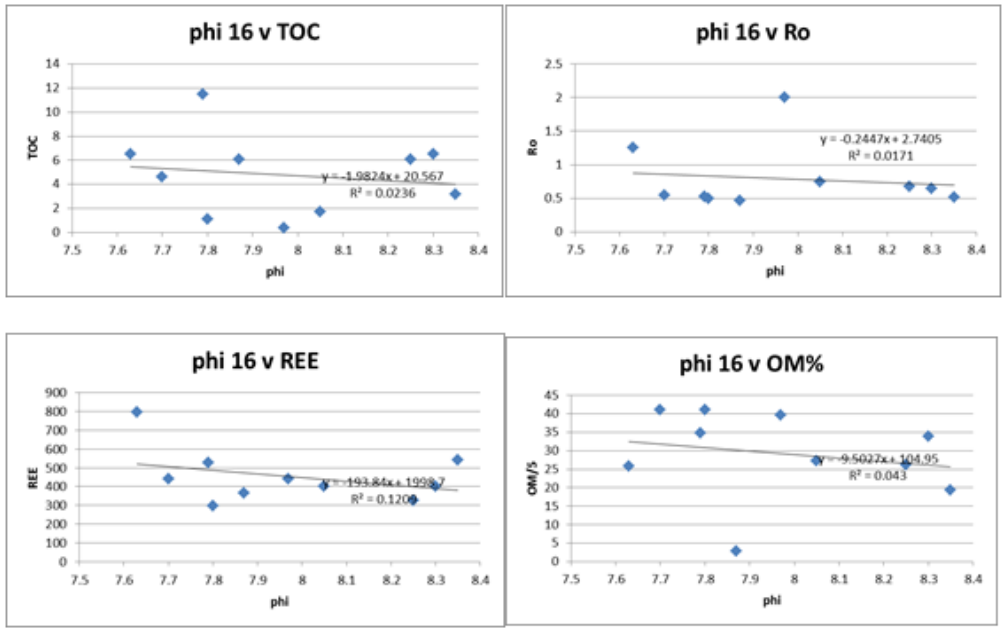


Figure A.6.2. Plots depicting no correlation between phi 16 and TOC, Ro, REE, and organic matter.

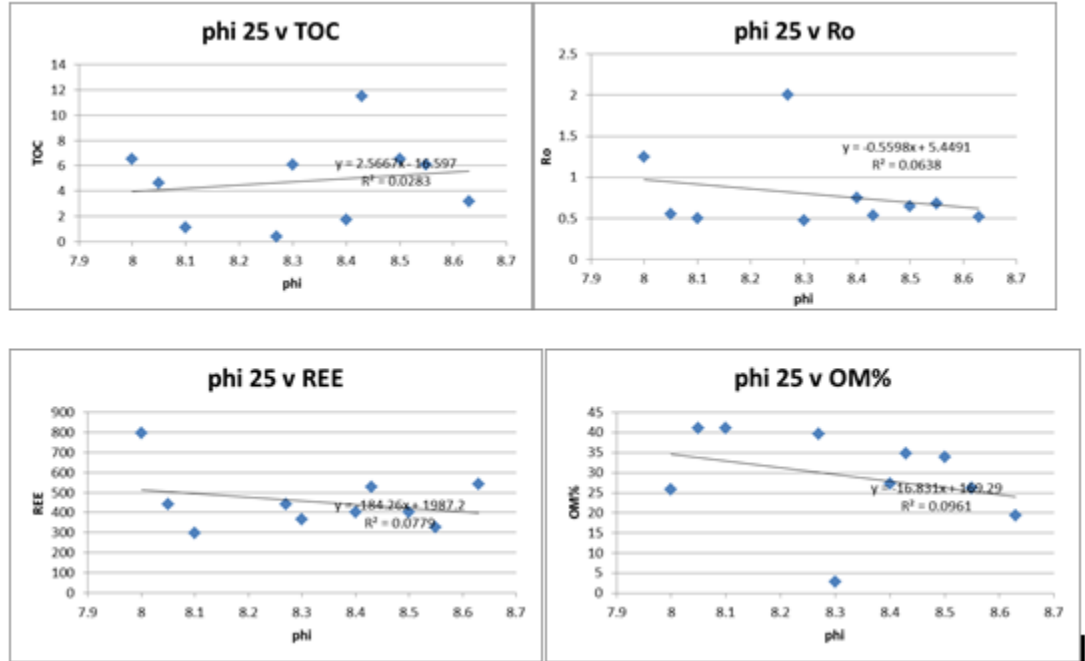


Figure A.6.3. Plots depicting no correlation between phi 25 and TOC, Ro, REE, and organic matter.

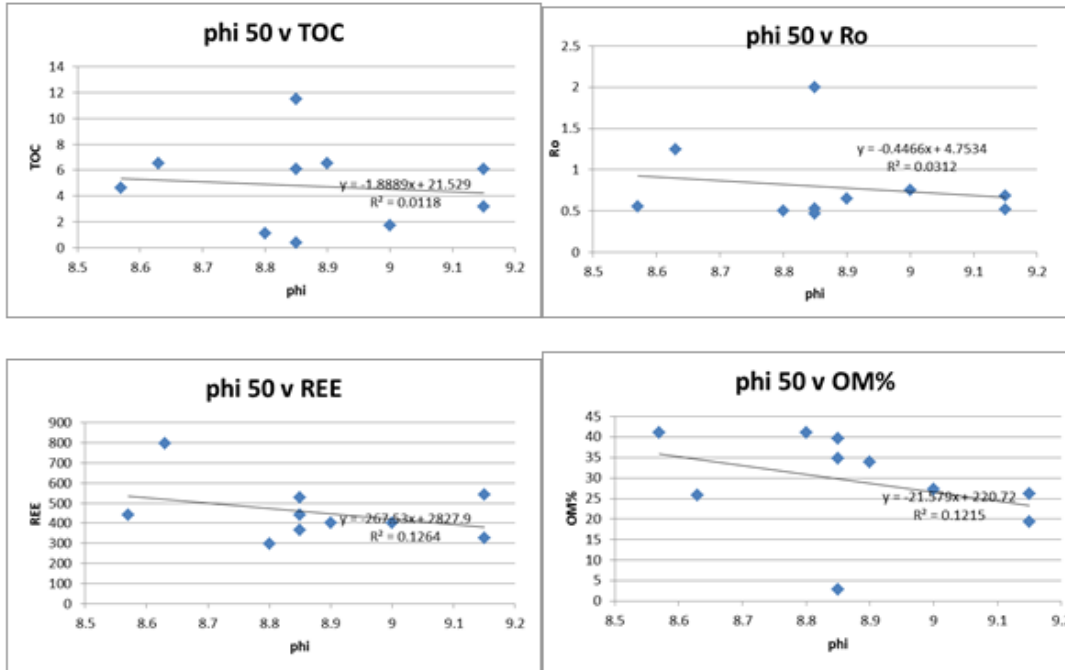


Figure A.6.4. Plots depicting no correlation between phi 50 and TOC, Ro, REE, and organic matter.

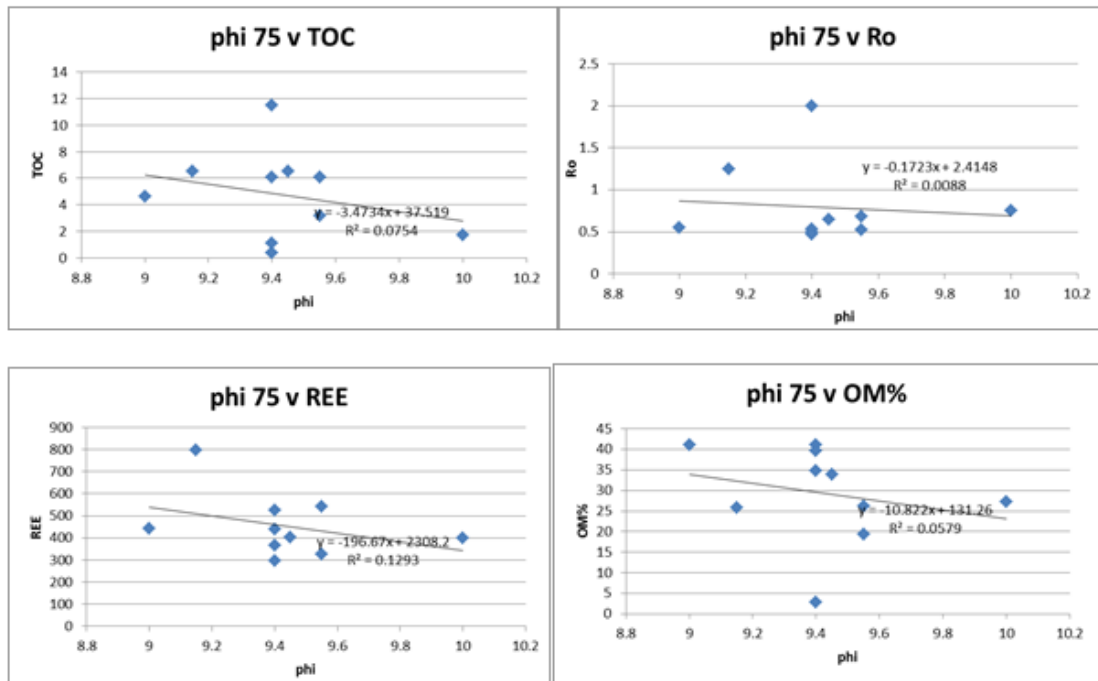


Figure A.6.5. Plots depicting no correlation between phi 75 and TOC, Ro, REE, and organic matter.

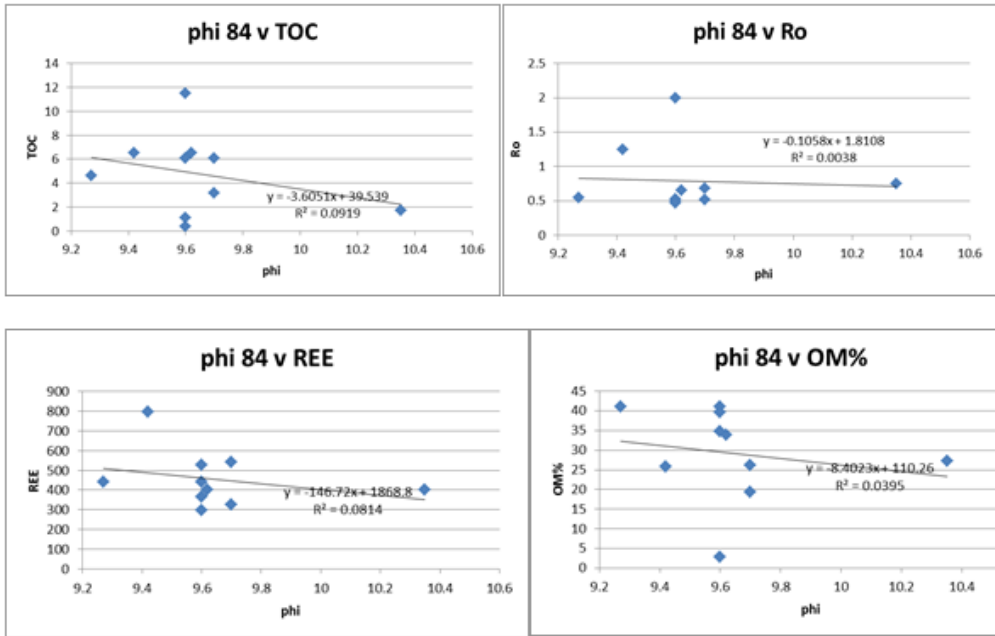


Figure A.6.6. Plots depicting no correlation between phi 84 and TOC, Ro, REE, and organic matter.

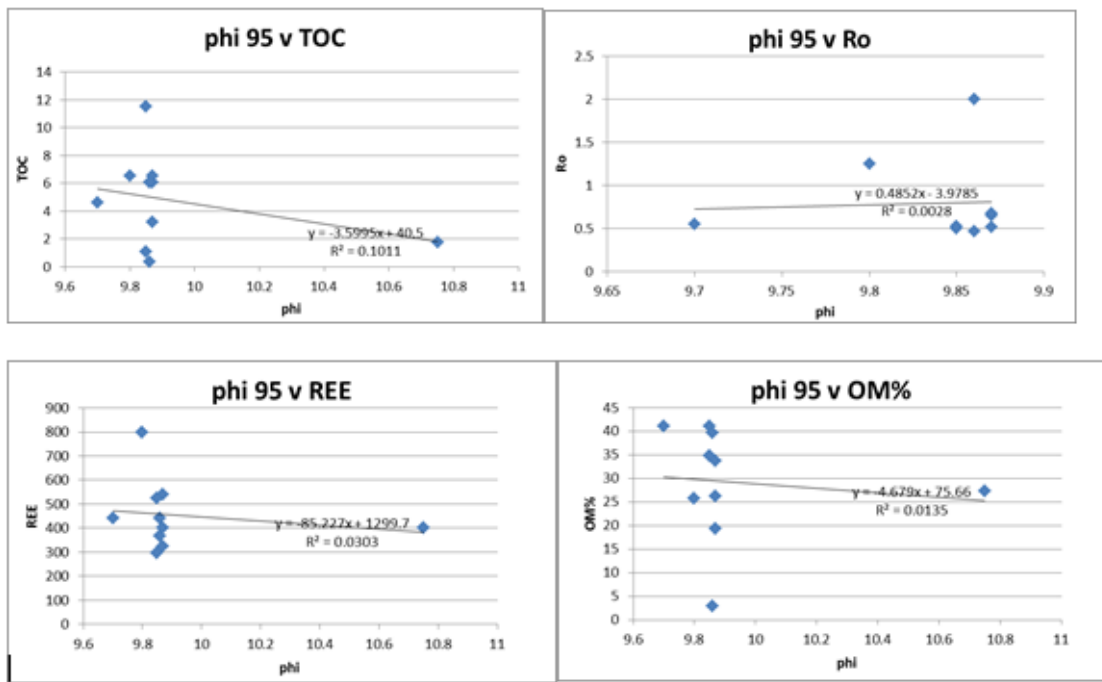


Figure A.6.7. Plots depicting no correlation between phi 84 and TOC, Ro, REE, and organic matter.

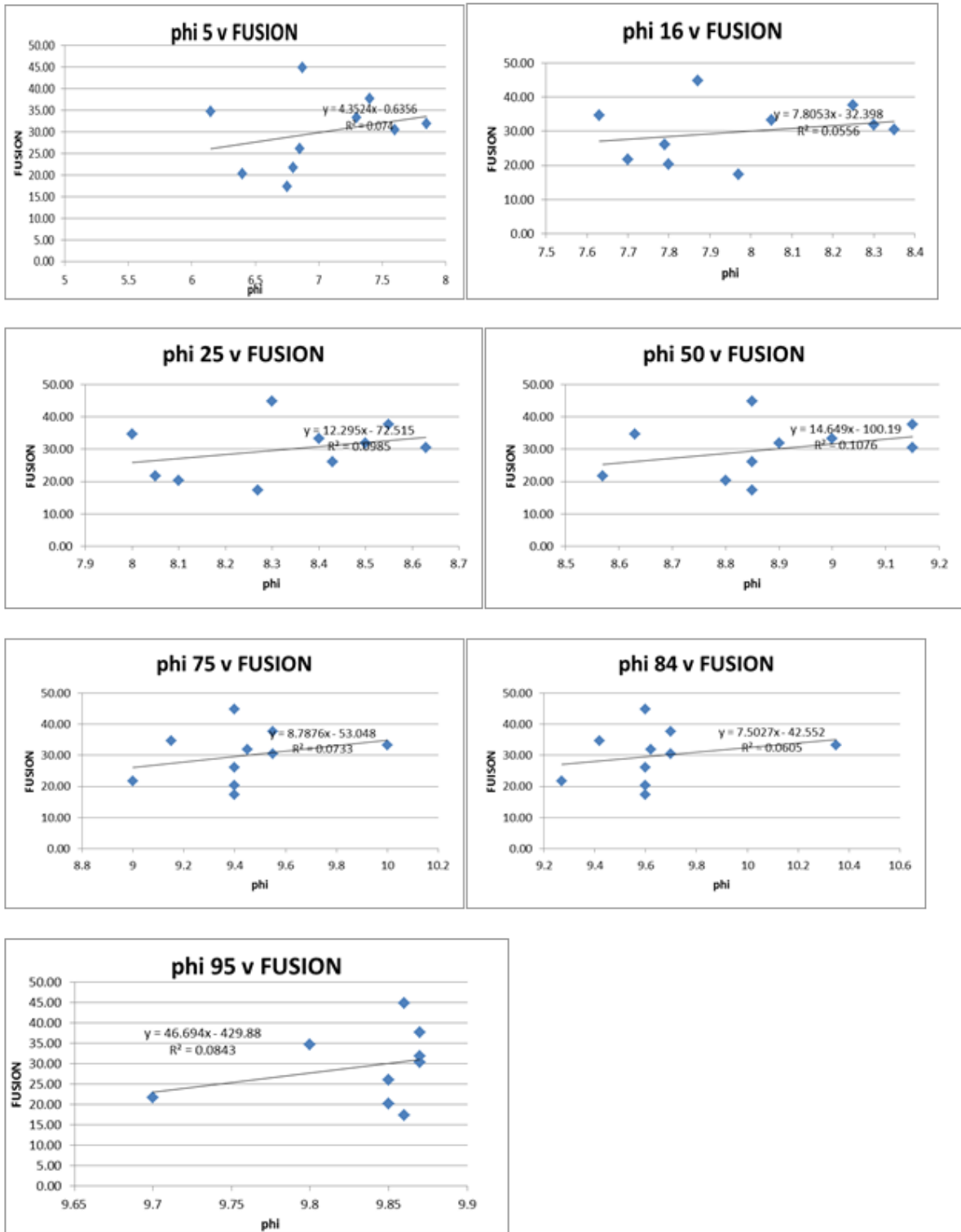


Figure A.6.8. Plots depicting no correlation between phi sizes and fusion weights.